Sintered CdTe nanocrystal films for optoelectronic applications and the sublimation of CdSe nanorods

By

Daniel John Hellebusch

A dissertation submitted in partial satisfaction of the

requirements for the degree of

Doctor of Philosophy

in

Chemical Engineering

in the

Graduate Division

Of the

University of California, Berkeley

Committee in charge:

Professor A. Paul Alivisatos, Co-Chair

Professor David B. Graves, Co-Chair

Professor Roya Maboudian

Professor Junqiao Wu

Fall 2015

Sintered CdTe nanocrystal films for optoelectronic applications
and the sublimation of CdSe nanorods

Daniel John Hellebusch

Abstract

Sintered CdTe nanocrystal films for optoelectronic applications

and the sublimation of CdSe nanorods

By

Daniel John Hellebusch

Doctor of Philosophy in Chemical Engineering

University of California, Berkeley

Professor A. Paul Alivisatos, Co-Chair

Professor David B. Graves, Co-Chair

Advances in colloidal nanocrystal chemistries have enabled more complex fabrication of nanostructured materials. Colloidal nanocrystals can be easily deposited from solution and used in a variety of optoelectronic applications such as photodetectors and photovoltaics. Colloidal nanocrystals deposited as films act as the light absorbing layer. These films can be used as-is or be sintered into polycrystalline films. Introducing dopant species as a surface species on semiconducting nanocrystals allows controlled doping profiles in sintered films where the dopant preferentially segregates at the grain boundaries. Chloride in CdTe films is one well-known example of this phenomena. The focus of this work is designing chloride-capped CdTe nanocrystal building blocks and sintering these into polycrystalline films with controlled grain structure and therefore doping profiles. Applications investigated for these films are solar cells and photodetectors.

Chapter 2 investigates CdTe nanocrystal chemistry to design and synthesize the CdTe-Cl nanocrystal building block for sintering into polycrystalline films. A quasi-spherical CdTe nanocrystal capped with Cd-oleate was synthesized and characterized. This starting quasi-spherical NC material was around 5 nm in size and possessed a wurtzite crystal structure with notes of zinc blende. Surface chemistry protocols were developed to react with the native cd-oleate ligand replacing it with a cadmium chloride species; colloidal stability of the CdTe-Cl NC was maintained by an octylamine shell.

Chapter 3 explores sintering the CdTe-Cl NC building blocks into polycrystalline CdTe films. Layers of CdTe NCs were deposited by spin casting and heating on a hotplate 300-400°C for 10s-

100s of secs to recrystallize the NCs into films with grain sizes 50-200 nm. At high nanocrystal formation, thick films formed numerous pores and voids. To mitigate these film defects, a layer-by-layer approach was explored. In this method, the nanocrystal concentration was found to control the grain structure of the film: high concentration yielded grainy and porous films while low concentration formed continuous, columnar films oriented normal to the substrate. Other film formation details were studied such as the effect of the formation of excess cadmium chloride on the films surface, intra-layer solvent rinses, and sintering in air.

Chapters 4 and 5 investigate applications of sintered CdTe-Cl NC films. In chapter 4, we fabricated solar cells using a simple, ITO-CdTe-ZnO-Al Schottkey-like structures. We demonstrated that solar cells incorporating columnar films exhibited >10x higher efficiency on average compare to a grainy film with comparable thickness. Columnar films grown by sintering in air boosted the efficiency nearly 2x over those fabricated in an inert environment. A simple 150 nm test structure was used to optimize key parameters such as nanocrystal concentration, temperature, and sintering time. An optimized test solar cell sintered in nitrogen yielded an average efficiency of 2.2% and 4.5% when sintered in air. In chapter 5, ultra-high gain photodetectors were fabricated by incorporating grainy films sintered in an inert environment. The sensitivity of semiconductor photodetectors is limited by photocarrier recombination during the carrier transport process. We developed a new photoactive material that reduces recombination by physically separating hole and electron charge carriers. This material has a specific detectivity (the ability to detect small signals) of $\sim 5 \times 10^{17}$ Jones, the highest reported in visible or infrared detectors at room temperature, and 4–5 orders of magnitude higher than that of commercial single-crystal silicon detectors. The material was fabricated by sintering chloride-capped CdTe nanocrystals into polycrystalline films, where Cl selectively segregates into grain boundaries acting as n-type dopants. Photogenerated electrons concentrate in and percolate along the grain boundaries – a network of energy valleys, while holes are confined in the grain interiors. This electrostatic field-assisted carrier separation and percolation mechanism enables an unprecedented photoconductive gain of $\sim 10^{10}$ electrons per photon, and allows active carrier quenching to control the device response speed.

Chapter 6, the sublimation of CdSe nanorods was explored. *In situ* electron microscopy was used to observe the morphological evolution of Cadmium Selenide nanorods as they sublime under vacuum at a series of elevated temperatures. Mass loss occurs anisotropically along the nanorod's long axis. At temperatures close to the sublimation threshold, the phase change occurs from both tips of the nanorods and proceeds unevenly with periods of rapid mass loss punctuated by periods of relative stability. At higher temperatures, the nanorods sublime at a faster, more uniform rate, but mass loss occurs from only a single end of the rod. We propose a mechanism that accounts for the observed sublimation behavior based on the terrace-ledge-kink (TLK) model and how the nanorod surface chemical environment influences the kinetic barrier of sublimation

Dedication

To my family and friends, I could not have done this without the love and laughter.

Table of Contents

List of Figures

List of Tables

Acknowledgements

There are numerous people I'd like to thank. First, and foremost, is my parents for their loving support for all of my endeavors throughout my life. I'd like to especially acknowledge that our 2-week long vacations during the summer throughout the country with a heavy emphasis on the American West. Exposing me to the natural world, these trips helped shape my world view that the planet is a wonderful place to live and something worth protecting. This emotional connection has driven me to seek out clean energy related research first at UT with Brian Korgel, and then at Berkeley with Paul Alivisatos. Of course I must also acknowledge my siblings, Renee, Sean, and Brendan that helped shape me during my childhood. Next on the list to acknowledge is Dr. Grant Willson at UT Austin. He was the one that plucked me out of his organic chemistry class in the Spring of 2007 and introduced me to research. In his lab I proved to Dr. Willson and myself that research was an enjoyable and intellectually rewarding activity. Brian Korgel offered my first research experience in solar cells. I loved every part of it. Then there is Paul---I have much to thank him in regards to the freedom he offered me to explore my own research interests with little funding restrictions. He challenged me to dive deep into the fundamentals of nanocrystal synthesis and properties. In addition, he assembled a lab personnel of graduate students and post-docs that helped me become a better chemist and overall researcher. Outside of lab work, I'd like to also thank all my volunteers that joined me with the SEED high school program. There is also the grad ChemE community that provided numerous social outlets. I'd also like to thank my class (grad Cheme 2010) for being there for classes, prelims, and quals. Finally, I'd like to thank my significant other, Maria Schriver, for joining me for the majority of my grad school career, and for her patient while I finished my PhD.

1 Chapter 1: Introduction

1.1 Nanomaterials for optoelectronic applications

Nanotechnology has now enjoyed several decades of basic science and engineering research. Early nanostructured materials were carbon nanostructures, quantum dots, and metal nanoparticles (specifically gold and silver.) These materials captured the fascination of scientists due to their size dependent physical properties at the nanoscale which were distinctly different from their respective bulk form. These materials exhibit a properties between those of single atoms, or clusters, and the bulk. The size of these material that span the properties from clusters to bulk—nanoscale. For example, nanoscale CdSe fluorescence spanned the entire rainbow while gold nanocrystals exhibited absorption in the pinks and purples. In this work, we focus on semiconductor nanocrystals, or quantum dots.

After the basic physical properties of quantum dots were explored and charted, investigators naturally wandered into applications. Semiconductor quantum dots absorb and fluoresce in the visible and ultraviolet spectrum. One of the most ubiquitous quantum dot systems is the II-VI. The optical properties of CdS, CdSe, and CdTe span the visible spectrum, and beautifully so. There is not a doubt that many scientists pursued the study of CdSe quantum dots just to be able to gaze at the gamut of colors they transmitted or fluoresced. In fact, this has been one of the benefits working in a quantum dot lab—I loved peering into the pure reds, yellows, and oranges of my labmates' work. My CdTe nanocrystal solutions, on the other hand, were large in size relative to its Bohr radius, and thus black. With absorbance in the visible spectrum, obvious applications were opto-electronic devices such as light emitting diodes (LEDs) and photovoltaics, and photodetectors. Colloidal quantum dots for these applications enjoyed the pervasive argument littering many introductions of scientific publications: these materials offer solution-processing and lead us from an expensive, high vacuum, high temperature, Dark Age to a magical low-cost era. This has a dubious claim: a few decades have passed and I still can't paint solar cells on my car or roof.

Colloidal quantum dots active in the UV-Vis-IR range can be incorporated into devices by two main processes. The first is simply deposit and use without modification. Early applications followed this process and found minimal success. One of the pitfalls to this method is not surprising: in order to achieve colloidal stability, these nanosized semiconductor crystals need a surfactant that binds to the surface. Once deposited to a substrate, these chains are no longer useful. As one can imagine, charges do not transport through these long, oily chains that coat the crystal. A lot of effort has been spent to remove these ligands after deposition with great success. For example, various short chained di-thiols such as benzene dithiol or ethanedithiol are used to kick off the lead-olate in PbS and PbSe films and link the crystals together.[1] The resulting meta-material is referred to as a *quantum dot solid*. When a PbS QD solid linked with ethandithiol is deposited on graphene, a tremendous gain is achieve.[2] PbS QD solids have achinved over 10% efficient solar cells.[3] But progress has been slow as interfaces pose a big impedance to charge transport.

The second method to incorporate colloidal quantum dots into device applications is to simply sinter them into polycrystalline films. Here, the quantum dots are simply a precursor to a solution processed semiconductor thin films. The method does not work very well for QD systems that require quantum confinement to access a particular band gap. For example, QD PbS can be tuned to absorb in the infrared, which is ideal for solar applications; but as a bulk semiconductor with a band gap around 037 eV, the applications are limited. Sintering NCs into films are ideal for material systems with a bulk bandgap in the IR-Vis such as CdTe, CIGS, and CZTS. QDd in the III-V system such as GaAs are theoretically ideal for this application. However, these materials have higher melting points and charge transports and film performance is very sensitive to defects.

In this work I focus on sintering CdTe NCs into thin films for opto-electronic applications. Sintering films for solar applications was the original goal of my Ph.D. research. CdTe hits a sweet spot for many of these requirements. The bulk band gap is 1.5 eV. This is near the solar spectrum maximum. In addition, the bonding structure has enough ionic character that enables a relatively low melting point compared to other semiconductors with band gaps near the solar spectrum maximum. This ionic character also reduces the impact of surface states and charge transport. In fact, I will discuss how the surfaces, or grain boundaries, can be converted from a performance liability to an asset by include chloride.

1.2 Role of chloride in CdTe films

Chloride plays a crucial role in the electronic properties of cadmium telluride polycrystalline films. This halide enables a film riddled with grain boundaries to efficiently conduct current enabling highly function solid state opto-electronic device most notably solar cells and photodetectors. For example, nearly all publications pertaining to CdTe photovoltaics report the best performance is obtain after the film has been exposed to chloride source.[4–6]

The origin of this performance is that chloride preferentially segregates at the grain boundaries causing highly localized n-type doping.[7–10] Until recently, chloride was believe to assist in homogeneous p-type doping of the CdTe film by coupling with cadmium vacancies.[4] About a decade ago scanning probes measurements provided photocurrent, surface potential, and capacitance maps that revealed grain boundaries conducted photocurrent and possessed an n-type doing.[11–13] Recently, elemental mapping combined with further correlation of grain boundary—photocurrent relationship improved the model.[9,10] Chloride substitutes for tellurium at the grain boundaries leading to localized n-type doing.[9] Theoretical calculations produced an energetic preference for the Cl at the CdTe grain boundary compared to the bulk CdTe and band dispersion calculations reveled that chloride assists in the removal of interband defect sites while contributing electron density into the conduction band.[9] In simpler terms, the chloride dopes the grain boundary as illustrated in Figure 1.1a.

Grain boundaries with n-type characteristic facilitate electron conduction through the material as well as separation of photogenerated charges. In general, grain boundaries scatter charge carriers in conducting materials such as CdTe. However, by exposing the material to chloride, the grain boundaries are converted to a network electron conduction pathways as illustrated in Figure 1.1b. Furthermore, grain boundaries introduce p-n type junction that assist in

the separation of photogenerated charges, enhancing the materials performance in opto-epectrical applications like photovoltaics.

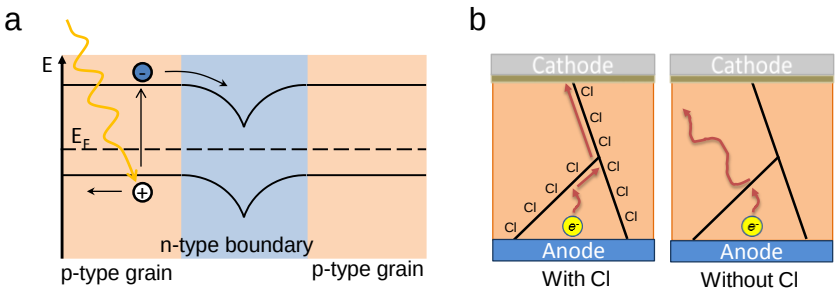

Figure 1.1. Illustration of the effect of chloride on CdTe grain boundaries. (a) Band bending in an n-type doped grain boundary. (b) Chloride-doped GBs act as electron conduction conduits.

1.3 Applications of CdTe films

1.3.1 CdTe Solar Cells

Solar energy is an important part of our low carbon energy generation portfolio. When most people think of solar, we usually think silicon solar cell. CdTe is the second most deployed light-absorbing material after silicon, albeit a long shot with only 5% of the market share. Salient metric for these two semiconductors are summarized in Figure 1.2a. Both Si and CdTe have a band gap near the theoretical solar spectrum maximum as shown in Figure 1.2b. However, CdTe trails Si in both commercial and lab-scale efficiency. CdTe has a unique advantage over Si; it is a direct bandgap semiconductor, meaning it requires much lees material to absorb the same amount of light. Typical CdTe devices have $1/10^{th}$ the material of Si. This is important in the pricing schemes of solar modules, which depend on the cost of the cost of the module, as well as the installed cost. CdTe historically has been cheaper than Si as evidence from learning curves of solar cells made from the two materials in Figure 1.2c. However, Si prices have dramatically dropped due to massive production which drive price down nearly the same cost as CdTe when this was written (Fall 2015). These days, the lack of efficiency in CdTe makes the material less attractive than silicon. Therefore CdTe needs a new learning curve. To do this, it needs a new process to gains in efficiencies. One way to jump onto a new learning curve for a technology is changing the way it is processed.

a

	CdTe	Silicon
Market Share	5%	90%
Band Gap (eV)	1.5	1.1
Efficiency	21	25
Thickness (μm)	5-20	100-500

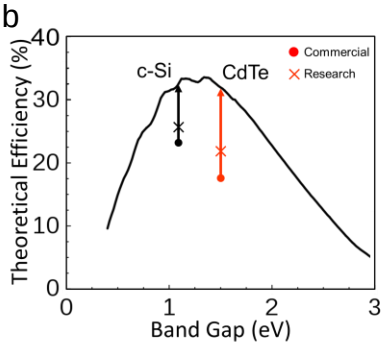

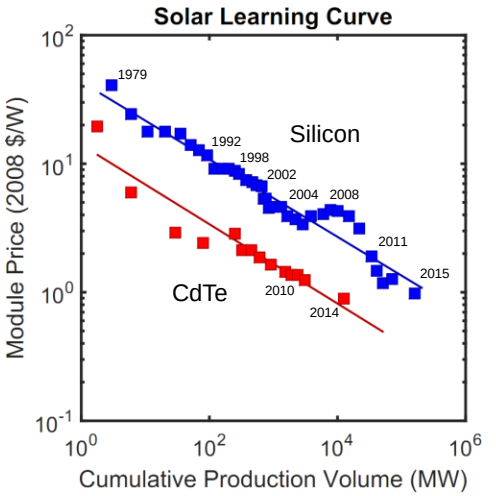

Green, Emery, Hishikawa, Warta, and Dunlop. *Prog Photovol.* 2015, 23, 1.
National Renewable Energy Laboratory. *Best Research-Cell Efficiencies Chart.* 2015.
Fraunhofer Institute. *Photovoltaics Report.* www.ise.fraunhofer.de. 2014.
Maycock, *Bloomberg New Energy Finance*, 2012.

Figure 1.2. Comparison of CdTe to Si for solar applications.

Conventional method to manufacture CdTe solar cells is known to be energy intensive as it requires high temps. Typically several microns of CdTe are deposited on a thin layer of CdS/transparent conducting oxide (TCO, such as ITO or FTO) by some physic vapor deposition, the most common is close-space sublimation. Next, the film is exposed to a chloride source and heated in a process called *chloride activation*, or when cadmium chloride, $CdCl_2$, is used, it is referred to as the *cadmium chloride treatment*. The chloride source is deposited from solution or in vapor form and the films is heated. During this process the film recrystallizes dramatically changing its grain structure from the initial deposition. Beside growing larger grains, cadmium chloride is also known to facilitate better charge transport in the film. Recently, chloride has been associated with n-type doping the grain boundaries facilitating better electron charge transport. The best performing cells experience some form of chlorination. Figure 1.3 illustrates this conventional film fabrication.

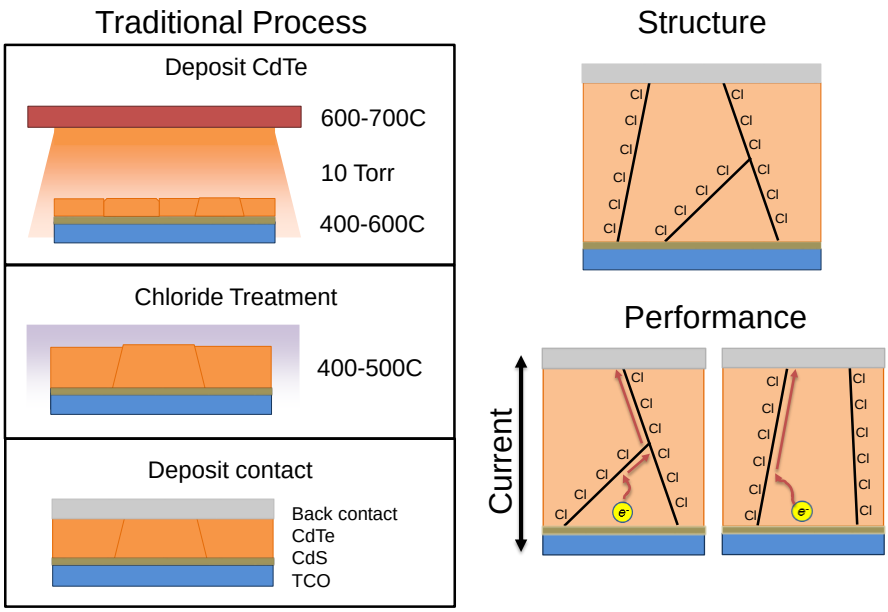

Figure 1.3. Conventional CdTe solar cell process-structure-performance relationship

The chloride activation step in conventional, multistep, process inhibits grain morphology control. During this intermediate step, the CdTe recrystallizes separating control of the film structure from the initial deposition. This disconnect weakens the ability to optimize performance in traditional process-structure-performance relationship concept the underlie materials engineering.

A solution-processed method to efficient CdTe films promises a more robust, and perhaps lower cost route to achieving high-efficient thin film solar cells. Starting with a building block that includes CdTe and Cl and sintering it into a thin films offers a simpler, more direct route to controlling grain morphology, and this performance. Therefore a stronger connect between the processing and structure and thus performance is established. This relationship is illustrated in Figure 1.4. Sintered NC films promise films in a single step, using a single precursor, for easy optimization. This vertically integrated fabrication process from NC to solar cell also enables us to study device and material fundamentals.

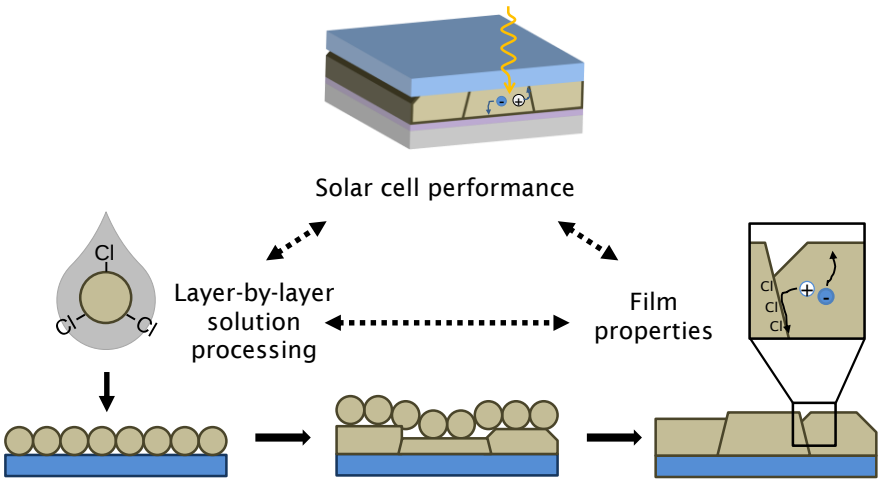

Figure 1.4. The process-structure-performance relationship in sintered CdTe solar cells.

1.4 References

(1) Brown, P. R.; Kim, D.; Lunt, R. R.; Zhao, N.; Bawendi, M. G.; Grossman, J. C.; Bulovi, V. *ACS Nano* **2014**, *8*, 5863.

(2) Konstantatos, G.; Badioli, M.; Gaudreau, L.; Osmond, J.; Bernechea, M.; de Arquer, F. P. G.; Gatti, F.; Koppens, F. H. L. *Nat. Nanotechnol.* **2012**, *7*, 363.

(3) Chuang, C.-H. M.; Brown, P. R.; Bulović, V.; Bawendi, M. G. *Nat. Mater.* **2014**, *13*, 796.

(4) McCandless, B. E.; Sites, J. R. In *Handbook of Photovoltaic Science and Engineering*; Luque, Antonio, Hegedus, S., Ed.; John Wiley and Sons: West Sussex, United Kingdom, 2011; pp. 601–641.

(5) Bonnet, D. *CdTe Thin-Film PV Modules*; Elsevier Ltd, 2012.

(6) Kumar, S. G.; Rao, K. S. R. K. *Energy Environ. Sci.* **2014**, *7*, 45.

(7) Li, C.; Wu, Y.; Pennycook, T. J.; Lupini, A. R.; Leonard, D. N.; Yin, W.; Paudel, N.; Al-Jassim, M.; Yan, Y.; Pennycook, S. J. *Phys. Rev. Lett.* **2013**, *111*, 096403.

(8) Li, C.; Poplawsky, J.; Wu, Y.; Lupini, A. R.; Mouti, A.; Leonard, D. N.; Paudel, N.; Jones, K.; Yin, W.; Al-Jassim, M.; Yan, Y.; Pennycook, S. J. *Ultramicroscopy* **2013**, *134*, 113.

(9) Li, C.; Wu, Y.; Poplawsky, J.; Pennycook, T. J.; Paudel, N.; Yin, W.; Haigh, S. J.; Oxley, M. P.; Lupini, A. R.; Al-Jassim, M.; Pennycook, S. J.; Yan, Y. *Phys. Rev. Lett.* **2014**, *112*, 156103.

(10) Poplawsky, J. D.; Paudel, N. R.; Li, C.; Parish, C. M.; Leonard, D.; Yan, Y.; Pennycook, S. J. *Adv. Energy Mater.* **2014**, *4*, n/a.

(11) Visoly-Fisher, I.; Cohen, S. R.; Gartsman, K.; Ruzin, a.; Cahen, D. *Adv. Funct. Mater.* **2006**, *16*, 649.

(12) Visoly-Fisher, I.; Cohen, S. R.; Ruzin, A.; Cahen, D. *Adv. Mater.* **2004**, *16*, 879.

(13) Visoly-Fisher, I.; Cohen, S. R.; Cahen, D. *Appl. Phys. Lett.* **2003**, *82*, 556.

2 Chapter 2: CdTe nanocrystal chemistry

2.1 Introduction

Target CdTe-Cl building block properties ideal for semiconducting CdTe films include a crystalline CdTe core and some chloride component greater than 1%.[1,2] Recent advances in CdSe nanocrystal (NC) surface chemistry has shown that the surface of CdSe can be modified with chloride and colloidally stable with BuP or a primary amine ligand.[3,4] The chloride content of ~3nm CdSe NCs is ~5-8 atom-% using this method.[3,4] Identified as a surface species, the chloride amount in a NC sample can be controlled by the volume to surface ratio via size control i.e. larger NCs will have lower Cl content and vice versa. However, when considering the downstream sintering process, we must keep in mind that changing NC size will also include the recrystallization dynamics. In this chapter, we demonstrate how surface chemistry established in CdSe NCs can be adapted to CdTe NCs to yield CdTe-Cl stabilized by octylamine.

2.2 Methods

2.2.1 Materials

Chemical	Purity	prep	Supplier
Synthesis			
Cadmium oxide powder (CdO)	99.999%	as received	Strem
Tellurium powder (Te)	~30 mesh, 99.997%	as received	Sigma Aldrich
Oleic acid	Technical grade, 90%	as received	Sigma Aldrich
1-Octadecene (ODE)	Technical grade, 90%	as received	Sigma Aldrich
Tri-n-butylphosphine (Bu_3P)	>97%	as received	Strem
Purification			
Methyl acetate	anhydrous, 99.5%	Dried over activated alumina, stored over 4 Å sieves at least 24hr before use	Sigma Aldrich
Pentane	anhydrous, ≥99%	Dried over activated alumina, stored over 4 Å sieves at least 24hr before use	Sigma Aldrich
Toluene	anhydrous, 99.8%	Dried over activated alumina, stored over	Sigma Aldrich

		4 Å sieves at least 24hr before use	
Ligand exchange			
Trimethylsilychloride (TMSCl)	redistilled, 99%	Reflexed over CaH_2 and distilled	Sigma Aldrich
Tri-n-butylphosphine (TBP)	>99%	As received	Strem
Octylamine	99%	Reflexed over CaH_2 and distilled	Sigma Aldrich

2.2.2 CdTe-Cd(oleate)$_2$ nanocrystal synthesis

CdTe nanocrystals capped with cadmium oleate ($Cd(oleate)_2$) with an ensemble size of approximately 5 nm were synthesized by a standard "hot injection" method modified from a previously reported protocol.[2] Specifically, 4.8 g (37.38 mmol) CdO, 42 g (148.69 mmol) oleic acid, and 40 g ODE were combined in a 500 ml three-neck round bottom flask. This mixture was degassed under vacuum at 100 °C for an hour. Meanwhile, two identical solutions of Te and Bu_3P were prepared: 1.5 g (24 mmol) Te and 12 ml Bu_3P were added to a 24 ml vial and heated to 220 °C until the powder dissolved and the solution became clear and yellow (~90 mins). Once a clear yellow color was reached, these solutions were cooled to room temperature. After degassing the contents of the round bottom flask, the head space was backfilled with argon and heated to 270 °C to form the cadmium oleate complex indicated by a color change from a red suspension to a clear, colorless solution. Once the temperature stabilized at 270C °C, the flask was promptly removed from the heating mantle and the two Te/ Bu_3P solutions were swiftly and simultaneously injected though 16-gauge needles into the hot solution. Upon injection, the clear solution quickly changed to a dark color. The flask was rapidly cooled to room temperature by spraying air and isopropanol from a wash bottle on the flask. After the solution cooled, the flask was connected (while under argon flow) to a distillation apparatus and the volatiles were vacuum distilled at 130 °C and 55 mTorr until ~40 ml of liquid remained. The crude product in the still pot was transfer via cannula to a schlenck flask and stored in an argon-filled glovebox waiting purification.

2.2.3 Nanocrystal purification

Nanocrystals were isolated and purified in an argon atmosphere. Approximately 10 ml of the crude product was added to a 50 ml centrifuge tube and filled with dried methyl acetate to ~40 ml total volume, and then centrifuged at 8,000 rpm for 5 mins. The clear supernatant was disposed and dark colored pellet with small amount of white content (presumably unreacted Cd-oleate) was dispersed in minimal amount (~3-4 ml) of pentane. Methyl acetate was added to a total volume of 50 ml creating a turbid solution which was then centrifuged at 8,000 rpm for 5 mins. The nearly clear super was disposed and the pellet was cleaned with 3 additional pentane/methyl acetate washing steps using minimal amount pentane to reduce the volume of methyl acetate needed to obtain a clear super (and complementary compact peller.) By the last step, the pellet no longer possessed a white streak visible in the initial step. Finally, the pellet was dispersed in 20 ml of toluene and filtered into a clean glass vial with a 0.2 μm PTFE syringe filter. The solution was then dried under vacuum until all volatiles were removed (≥60 mins.) The dried residue was

dispersed in toluene until a concentration of 1.5 mM using the absorbance correlation previously established.[5]

2.2.4 Surface modification of CdTe-Cd(oleate)$_2$ nanocrystals with chloride

CdTe NC surface reaction was performed in an argon environment by adopting protocols established for CdSe-Cd(oleate) NC to CdTe.[4,3] The ligand surface density was not measured but assumed to be 3 ligands/nm^2 as reported for CdSe in Ref. 4. It is crucial to rid all reagents and solvents of water using rigorous drying methods described in the materials section above (Section 2.2.1.) To begin, ~4 µmol CdTe-Cd(oleate)$_2$ NC (~2.7 ml of 1.5 mM NC solution) was added to a glass vial. Bu_3P was added to the NC solution to a concentration of 500 mM. While the solution was stirred, 1.4 ml (12x molecular equivalents/NC nm^2, or 10.6 mmol) of TMSCl was added. *If any water is present, HCl will etch the NCs. Therefore, toluene and TMSCl must be rigorously dried.* After the solution stirred for 1 hr, the volatiles were removed by vacuum distillation at room temperature (a small amount of liquid remained, presumably the Bu_3P). After ~1 hr of vacuum exposure, 3 ml of toluene was added to the remaining product and the vial was shaken to mix and then centrifuged for 4,000 rpm for 5 mins. The clear supernatant was disposed and 5 ml of toluene was added to the pellet and shaken to disperse (not well). 147 µL octylamine (3x molecular equiv/nm^2 NC) was added to the suspension and the NCs immediately dispersed as the primary amine displaced the Bu_3P and coordinated the NC surface. After stirring for 1 hr, methyl acetate was added to flocculate the solution, which was then centrifuged at 4,000 rpm for 5 mins. The supernatant was then disposed. The toluene/octylamine exposure step was repeated two more times to ensure all Bu_3P was removed and maximum surface coordination was achieved. If too much octylamine is added in this step, the NC require excessive amounts of methyl acetate to achieve a clear super and large pellet. The final pellet was dispersed in ~5 ml toluene and filtered with a 0.2 µm PFTE syringe filter into a clean glass vial, then dried under vacuum until dryness (~1 hr.) The dark residue was dispersed in toluene to a NC concentration of ~500 mM.

2.2.5 Absorbance

Absorbance of CdTe nanocrystal solution was measured with an Agilent UV-Vis Spectrophotometer. All CdTe samples were dispersed in toluene. A spectrum was measured by blanking the instrument with the same quality toluene as the sample was stored (i.e. anhydrous toluene, dried toluene, etc.) An ideal spectrum had the first exciton below an absorbance value of O.D = 0.1. To calculate the *average NC ensemble size*, d_{NC}, of the sample (assuming spherical shape), the position of the NC solution first exciton peak was identified and used in an correlation (equation 2 in Ref. 5.) To calculate the *nanocrystal concertation* ([NC]), the absorption coefficient in the continuum states at 410 nm, ε_{410}, is calculated using d_{NC} and another correlation in Ref. 5 (equation 9). The absorbance at 410 nm, A_{410}, is then identified from the sample spectrum and Beer's law is then invoked to calculate the concentration ($A_{410} = c\varepsilon_{410}L, L = 1\ cm$); this is then multiplied by a dilution factor to obtain the nanocrystal solution of the original sample (i.e. how diluted the UV-Vis sample from the original.)

2.2.6 Transmission electron microscopy

Transmission electron micrographs were taken on an FEI Tecnai G2 S-Twin TEM. Images were recorded with a Gatan Orius SC200 CCD. Only contrast adjustments were made.

2.2.7 H-NMR

H-NMR spectra used to identify the organic component of the nanocrystal ligand shell were measured on a Bruker AVB-400 with a 400 MHz field. A high NC concentration (~0.5 mM @ ~5 nm), and hence ligand concentration (~100s mM), is required to measure a spectrum, especially when monitoring the weak vinyl peak of the native oleate ligand.[4,6] Ligand concentration is the most important concertation to control.

2.3 Nanocrystal synthesis and surface chemistry

2.3.1 Synthesis of CdTe-Cd(oleate)

A target CdTe-Cl building block is obtained by adopting surface chemistry pioneered by Jon Owen for cadmium selenide nanocrystals stabilized with cadmium-oleate[4,6,7]. The native ligand in many cadmium chalgogenide nanocrystals, cd-oleate provides a handle to evaluate the extent of reaction in surface modifications e.g. ligand exchanges. Oleate possess two vinyl hydrogens that have an H-NMR resonance far upfield (~5.5-5.6 ppm) from the other protons on the alkyl chain.[6,8] This separation allows quantitative and qualitative analysis of the extant of removal of the oleate species. In order to use this ligand exchange ruler, we targeted a nanocrystal synthesis to produce oleate-capped CdTe nanocrystals as the basis of our CdTe-Cl building block.

CdTe-oleate nanocrystals were synthesized in a gram-scale reaction via a *hot injection* method adopted from previous methods.[2] Briefly, a solution of tri-n-butylphosophine telluride is injected into a hot solution of cadmium oleate in octadecene and oleic acid and immediately cooled to terminate nanocrystal growth. This crude solution is vacuum distilled to remove the majority of volatiles, followed by purification via centrifugation using the pentane/methyl acetate solvent/antisolvent pair. The purified product was dispersed in toluene for further use.

The final CdTe-oleate was characterized to confirm its physical properties prior to surface modification with chloride. Transmission electron micrographs revealed that the nanocrystals have an irregular, quasi-spherical shape. In some cases, adjacent particles appear to have necked (Figure 2.1a.) Powder x-ray diffractogram shows that the particles possess a mixture of *zinc blende* and *wurtzite* crystal structures (Figure 2.1b.) The most likely structure is a wurtzite structure with a high population of stacking faults that manifest as zinc blende pattern.[9,10] The final product has an average nanocrystal size of ~4.9 nm calculated from the first exciton feature in the absorbance spectrum (Figure 2.1d.)[5] Finally, from the H-NMR spectrum we can confirm that the dominant ligand on the surface is oleate (Figure 2.1d.)[4,6] EDS measurements show that the cadmium to tellurium radio is 1.19:1. Assuming the core of the NC is stoichiometric Cd:Te 1:1, the excess of Cd is with an Cd-oleate surface species.[4,6,11–13] Although charge balance suggests that the structure of Cd-oleate to be $Cd(II)(Oleate)_2$, we were unable to confirm that this is the exact ligand species since oleate concentration was not obtained from the HNMR spectrum.

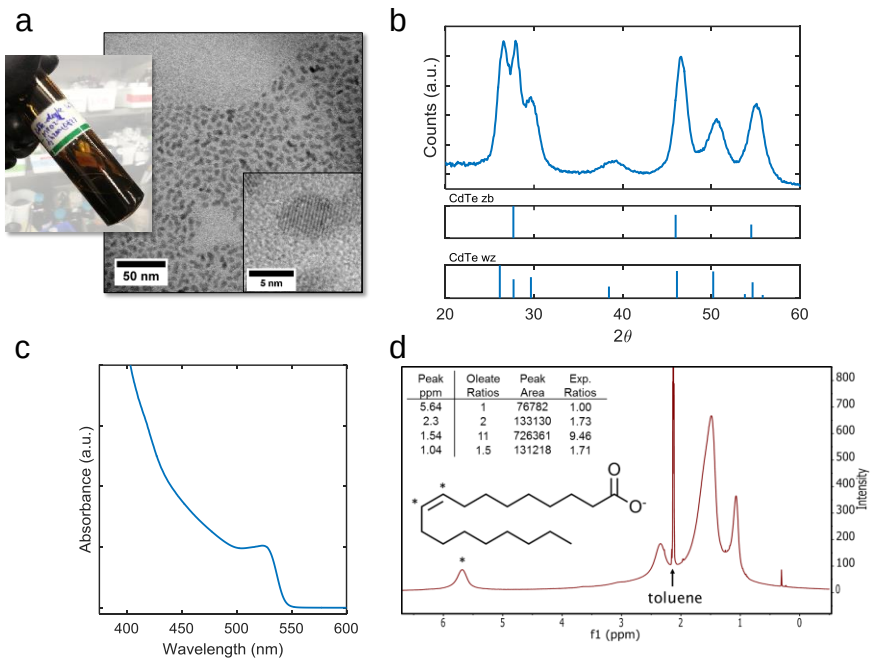

Figure 2.1.CdTe-oleate NC characterization: (a) Photograph of solution in vial (overlay), TEM image of low resolution and high resolution (inset); (b) powder XRD; (c) absorbance; (d) H-NMR, 0.5 mM NC measured in d8-toluene.

2.3.2 Surface modified CdTe with chloride, stabilized with $OctNH_2$

CdTe nanocrystals were surface-modified with chloride by exposing the oleate-capped NCs to trimethylsilychloride (TMSCl) in the presence of tributyl-n-phosphine (Bu_3P.) This reaction scheme was adopted from surface chemistry previously developed with CdSe NCs.[4] It is imperative that Bu_3P is introduced to the system *prior* to TMSCl, and that the solvent, toluene, is rigorously dried (otherwise generated HCl will etch the nanoparticles.) TMS group reacts strongly with the carboxylate portion of the oleate surface species forming a strong silicon-oxygen bond—the driving force for the reaction.[7] The chloride then bonds to the surface cadmium to maintain charge balance in the overall reaction. This reaction can be thought of as a substitution reaction, although the exact type (S_N1 or S_N2) is unknown at this time. If the CdTe-oleate NCs are directly exposed to TMSCl, the surface chloride does not provide an adequate barrier to Van de Waals forces between the NC cores which lead to irreversible aggregation (see reaction (a) in Figure 2.2. CdTe nanocrystal chloride surface reaction)[7] This is consistent to what was observed in the CdSe NC system.[4,7]

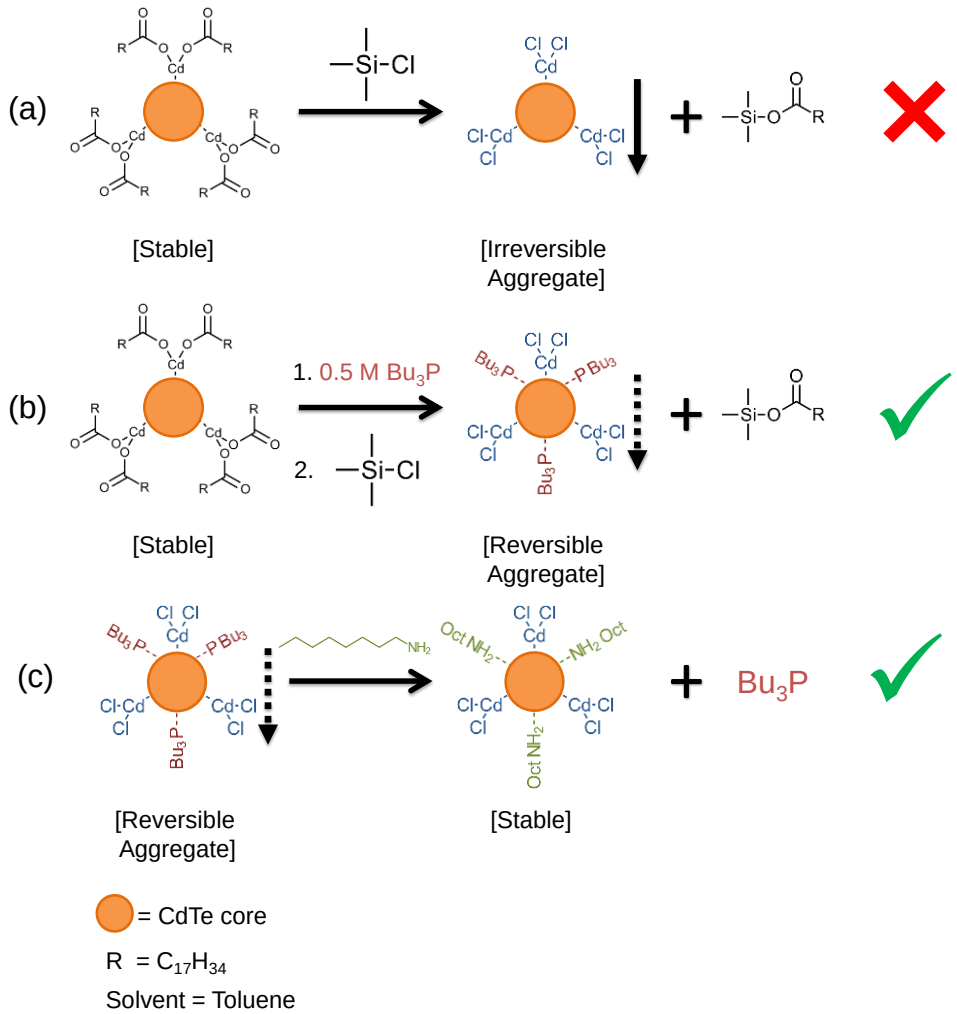

Figure 2.2. CdTe nanocrystal chloride surface reaction

Irreversible aggregation is prevented by introducing a co-ligand, Bu3P, before the TMSCl (see reaction (b) in Figure 2.2. According to previous studies in the related CdSe NC system, Bu_3P displaces ~30% of the surface Cd-oleate. However, once TMSCl is introduced, stripping the surface oleate species, the Bu_3P datively binds with the exposed surface preventing irreversible aggregation. Bu_3P does not permit the CdTe-Cl NCs to be colloidally stable in nonpolar solvents, as opposed to the ~3 nm CdSe NC systems where the analogous species is reported to be stable nonpolar solvents. The lack of colloidal stability in the [CdTe-Cl]Bu_3P system maybe be the result of lower surface coverage (1 Bu_3P/nm^2 calculated in CdSe[4]), lower radius of curvature, slightly weaker binding than in CdSe, or a combination of these effects. Neither of these were experimentally confirmed for [CdTe-Cl]Bu_3P.

Colloidal stability for CdTe-CL NCs is regained by adding octylmine (see reaction (b) in Figure 2.1.) Previous reports found that primary amines were ideal for displacing Bu_3P on the CdSe-Cl nanocrystals.[4] In our system, we wanted a primary system with a length to provide adequate colloidal stability, but can de desorbed from the surface during sintering. Ligand boiling point was used as a proxy for the latter. Butyl amine (b.p. 77-79°C) was found lead to aggregation

over time. This is presumably due to the short chain length that provides only a modest barrier to the Van der Waals interaction between NC cores.[4,3] We decided that octylamine (b.p. 175-179°C is an optimal primary amine for creating an alkyl barrier between CdTe cores, but would desorb well below the proven sintering temperature of 350°C.[2,14] Upon adding octylamine, the CdTe-Cl suspension immediately dispersed in toluene as the Bu_3P are presumably displaced by the primary amine (reaction (c) in Figure 2.2.) The entire reaction scheme converting [CdTe](Cd-oleate) to [CdTe](Cd-Cl2){Bu3P} is summarized in Figure 2.4.

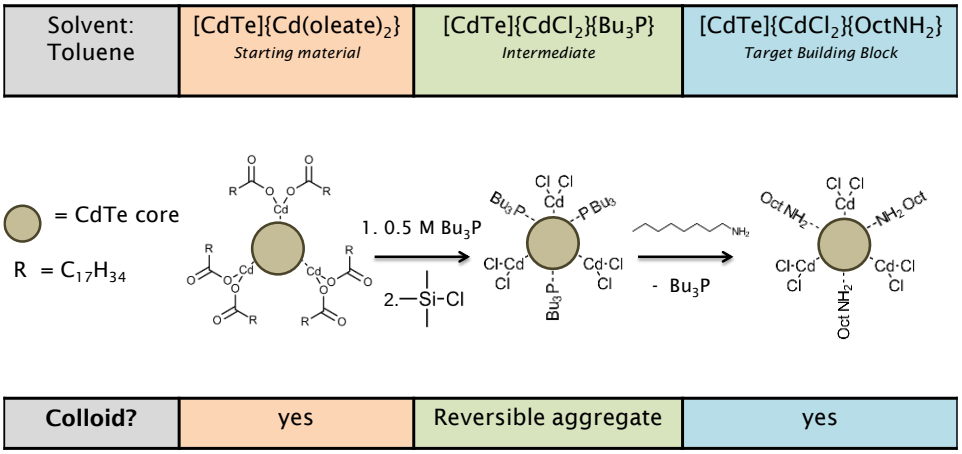

Figure 2.3. CdTe NC surface reaction summary

Absorbance spectrum reveals that the chloride modified NCs have a ~3 nm blue shift in the first exciton but maintain a similar size distribution as indicated by the half-width-half-maximum of the first peak of ~26 nm. EDS shows a decrease in the Cd:Te ratio and increase in chloride content. This amounts to 5-6 at-% chloride in the CdTe-Cl product. This is consistent with the CdSe-Cl system.[4,3] H-NMR confirms the removal of the oleate surface species as indicated by the disappearance of the ~5.6 ppm vinyl proton peak.

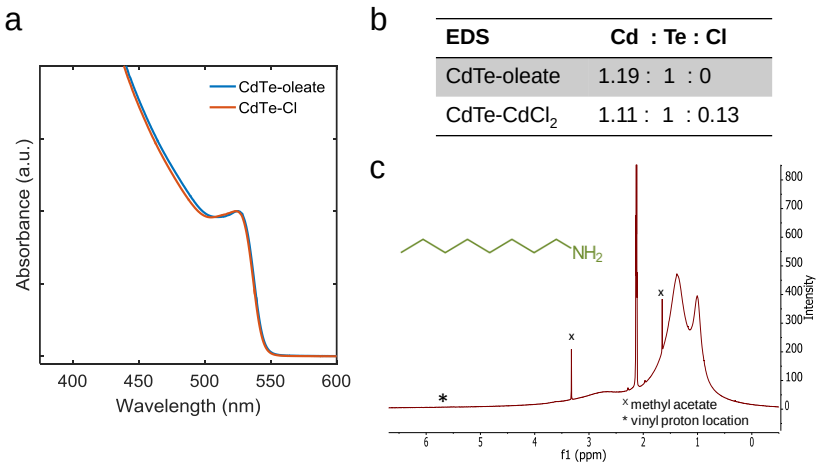

Figure 2.4. Characterization of CdTe-Cl nanocrystals

One of the outstanding questions for the chloride-terminated CdTe or CdSe NCs is the nature of the surface species. Owens et. al. conjecture that chloride exists in the form of surface $CdCl_2$ by a charge balance argument.[4] If we assume the core is stoichiometric CdTe (1:1) and excess cadmium species is Cd^{2+}, charge balance requires excess cadmium-to-chloride EDS signal to 1:2. However, this ratio is 1.2 in our system. A <2 ratio was reported for the analogous CdSe-$CdCl_2$ system.[4,3] This inconsistency suggests that our understanding of the surface species is incomplete. If we relax the assumption that the core is stoichiometric CdTe, but maintain Cd:Cl 1:2 ratio, then the core is Te deficient. We know that at grain boundaries in CdTe films, Cl substitutes for Te 1:1.[15] If substitution hold true for a CdTe NC surface, then we find the ratio Cd:(Te+Cl) surprisingly near unity. Until further investigation, we will have to settle for an incomplete view of the CdTe-Cl NC building block.

2.4 Conclusion

In this chapter a synthesis of a colloidally stable CdTe-Cl NC building block was demonstrated. CdTe-Cd-oleate NC with a quasi-spherical shape and wurtzite crystal was synthesized on the gram scale and characterized. A protocol was adapted to this system to obtain CdTe-Cl colloidally stabilized by octylamine. Future work for the nanocrystal chemistry include more complete characterization of the organic ligand component via H-NMR (i.e. # of Cd-oleate/nm^3). Better shape control is also desired. Ideally we would have a spherical particle with size control. Using size to control the Cd:Cl ration needs to also be demonstrate to increase the level of control this building block has for the downstream sintered films. Finally, a more complete model of the Cl species on the species needs to be investigated.

2.5 References

(1) Niles, D. W.; Waters, D.; Rose, D. *Appl. Surf. Sci.* **1998**.

(2) Panthani, M. G.; Kurley, J. M.; Crisp, R. W.; Dietz, T. C.; Ezzyat, T.; Luther, J. M.; Talapin, D. V. *Nano Lett.* **2014**, *14*, 670.

(3) Norman, Z. M.; Anderson, N. C.; Owen, J. S. *ACS Nano* **2014**, *8*, 7513.

(4) Anderson, N. C.; Owen, J. S. *Chem. Mater.* **2012**, *25*, 69.

(5) Kamal, J. S.; Omari, A.; Van Hoecke, K.; Zhao, Q.; Vantomme, A.; Vanhaecke, F.; Capek, R. K.; Hens, Z. *J. Phys. Chem. C* **2012**, *116*, 5049.

(6) Anderson, N. C.; Hendricks, M. P.; Choi, J. J.; Owen, J. S. *J. Am. Chem. Soc.* **2013**, *135*, 18536.

(7) Owen, J. S.; Park, J.; Trudeau, P.-E.; Alivisatos, A. P. *J. Am. Chem. Soc.* **2008**, *130*, 12279.

(8) Hens, Z.; Martins, J. C. *Chem. Mater.* **2013**, *25*, 1211.

(9) Peng, X.; Manna, L.; Yang, W.; Wickham, J.; Scher, E.; Kadavanich, a; Alivisatos, A. *Nature* **2000**, *404*, 59.

(10) Manna, L.; Scher, E. C.; Alivisatos, a. P. *J. Am. Chem. Soc.* **2000**, *122*, 12700.

(11) Jasieniak, J.; Mulvaney, P. *J. Am. Chem. Soc.* **2007**, *129*, 2841.

(12) Chen, O.; Yang, Y.; Wang, T.; Wu, H.; Niu, C.; Yang, J.; Cao, Y. C. *J. Am. Chem. Soc.* **2011**, *133*, 17504.

(13) Taylor, J.; Kippeny, T.; Rosenthal, S. J. *J. Clust. Sci.* **2001**, *12*, 571.

(14) Jasieniak, J.; MacDonald, B. I.; Watkins, S. E.; Mulvaney, P. *Nano Lett.* **2011**, *11*, 2856.

(15) Li, C.; Wu, Y.; Poplawsky, J.; Pennycook, T. J.; Paudel, N.; Yin, W.; Haigh, S. J.; Oxley, M. P.; Lupini, A. R.; Al-Jassim, M.; Pennycook, S. J.; Yan, Y. *Phys. Rev. Lett.* **2014**, *112*, 156103.

3 Chapter 3: Sintered CdTe nanocrystal films

3.1 Introduction

Sintering is a materials processing method where a powder compact or film is converted into a continuous body.[1–3] The goal of sintering is to increase the density of grain size of the material. The macroscopic driving force behind sintering is the elimination of high-energy interfaces. The initial powder can be any solid material with any size and distribution of sizes. Typically, the starting material is metellic or ceramic with micrometer sized particles with a relatively narrow size distribution, but sizes can reach the nanoscale domain. The product is typically a dense solid with large grain size. Sintering is most often induced by heating, but can also occur with combination of pressure or electrical charge. Sintering is often employed to shape materials that have a very high melting point that preclude injection molding such as refractory materials. Tungsten carbide and alumina are examples of materials that are sintered into manufactured components. Sintering also offer unique control of the density and grain size that determines a materials properties, most importantly, strength.

Since colloidal nanocrystals enable solution deposition of nanoparticle films with control composition, we proposed to employ sintering as a method to convert nanocrystalline deposits into much larger grain thin films. Since sintering offers robust control over the mechanical properties such as grain size, we expect to use this method to tune the electrical properties of resulting polycrystalline thin films for various properties. Understanding the fundamentals of sintering will enable us to control the grain composition and this electronic properties.

3.2 Sintering fundamentals

Sintering is a complex transformation of a many-bodied material into a single material. The process is so complex, it evades a single mathematical treatment. Those that exist are devised from basic principles, but generalized terms are found from empirical correlations which weaken their physical meaning. Following will be a summary of the fundamentals that pertain to the sintering of nanocrystals into polycrystalline thin films.

The goal of sintering is the conversion of a compact power into a dense body with grain size large than the initial powder size. The macroscopic driving force of sintering is the elimination of interfacial energy. Interfacial energy can manifest as solid surfaces in contact with a fluid or another solid. When this solid-solid interface partitions identically composed material but with different crystallographic orientation, we get a grain boundaries. Assuming the process occurs isothermally, a thermodynamic relationship for the Gibbs free energy of the system is[1–4]

$$\Delta G = \Delta(\gamma A)$$

During the sintering process, the powder compact experiences **coarsening** and **densification**. These two major physical processes are axes in the sintering process coordinate space illustrated in Figure 3.1. **Coarsening** occurs when the interfacial area is constant and the total area of this type of interface is reduces. If the interface is solid-vapor, coarsening is known as *coalescence*; if the interface is a grain boundary, it is called *grain growth*. **Densification** occurs

when the interface area is held constant and the interfacial energy is reduce. Here, high energy solid surfaces are replaced with low energy grain boundaries. Densification is not broken down into subcategories since the process is the same whether the coarse size is large or small.

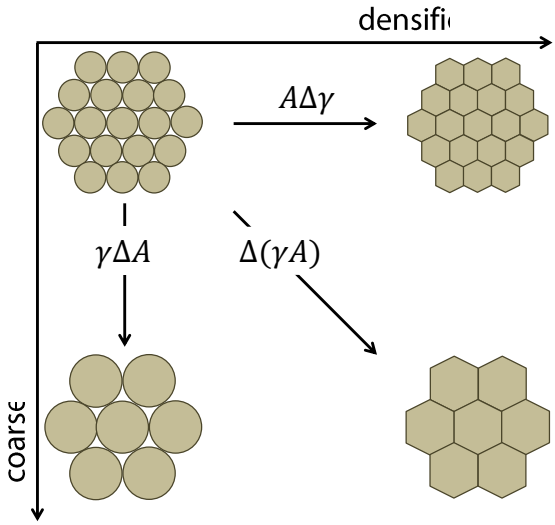

Figure 3.1. Two coordinates of sintering, densification and coarsening. Adopted from Ref. 1

Sintering proceeds along both coordinates simultaneously, but one process can dominate depending on the stage. Often, sintering is categorized into three phases that are dominated by one of these processes. Unimaginatively, these phases, or stages, are referred to as *initial*, *intermediate*, and *final*.[1,2] In the *initial* stage, coarsening dominates as adjacent particle coalesce into larger particles. In the *intermediate* stage, densification dominates as particles begin to interface creating grain boundaries. Merging particles divide up the empty spaces into voids, or pores. Pores are eliminated in this second phase as the sintered bodies densify. In the *final* stage, coarsening dominate again as grain boundaries migrate leading to grain growth. Even though a process dominates a stage, the other occurs simultaneously.

From a macroscopic perspective, sintering can be considering a form of recrystallization. This is especially true as the average particulate size of the powder tends towards the nanoscale and even cluster size. When we view sintering as a recrystallization, we can invoke the *Avrami equation*, or to give full credit, the *Johnson-Mehl-Avrami-Kolmogorov equation*.[5–8]

$$Y = 1 - \exp(-Kt^n)$$

Fraction recrystallized (or sintered in our case), Y, is related to time, t, with constant K and time exponent n. This relationship is derived from the assumption that nucleation of a second phase occurs randomly through the entire volume, and phase two growth isotropically from these nucleation sites. Constant K can be related to the nucleation rate $\dot{N}$ and growth rate of the second phase $\dot{G}$ by

$$K = \frac{\pi}{3}\dot{N}\dot{G}^3$$

This expression falls out from the derivation of the Avrami equation. Full strength of the Avrami equation requires expressions for the nucleation and growth rates, which are non-trivial to obtain. Therefore, K and n are typically fit from empirical data.

The Avrami equation typically yields a sigmoidal curve relating percent recrystallized as a function of time as seen in Figure 3.2a. If desired, one can qualitatively map the three stages on this curve. Avrami shows that increasing the temperature of recrystallization, or sintering, leads to fast conversion (Figure 3.2b).

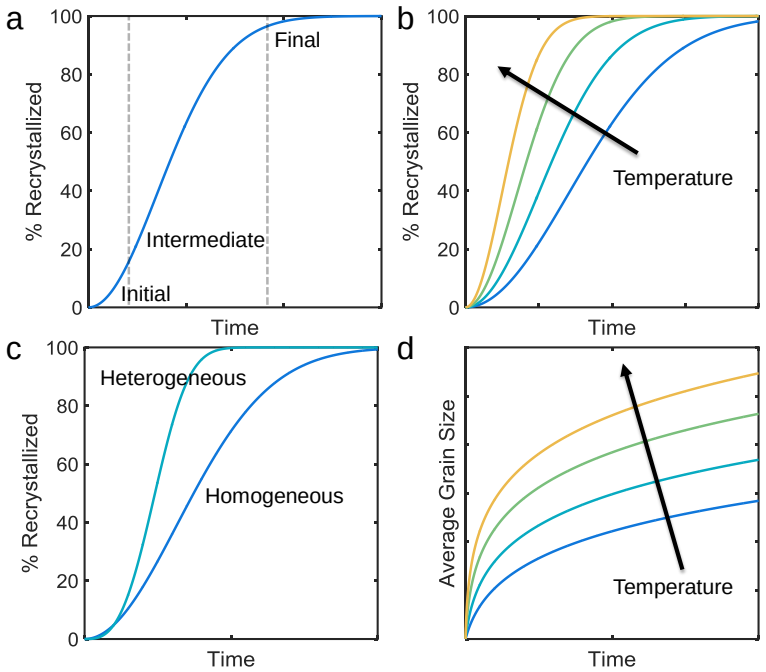

Figure 3.2. Mathematical modelling of sintering.

On key component of this model is the nucleation rate. Typically, nucleation occurs when a cluster is formed from the first phase due to random thermal fluctuations that spontaneously form the second phase. This is *homogenous nucleation*. In a second method, a second phase forms at an interface, such as a substrate crack or other imperfection. This is *heterogenous nucleation*, and this process has a lower energy barrier.[5] The Avrami equation can capture this reduced barrier by increasing n as shown in Figure 3.2c.

Grain size control is paramount to the sintering process. Although the Avrami equation captures the progress of recrystallization, it does not capture the physical intricacies of each phase. For example, the evolution of grain size as a function of time is not represented. To model grain growth, which dominates the final stage of sintering, we resort to the *general grain growth equation*[1,2,9]

$$D^m - D_0^m = Ct$$

Average diameter of the grains D is related time t and constant C. The exponent m is 2 in an ideal case, and increases for non-ideal behavior. Typically, constant C represents the diffusion of grain boundaries and invokes an Arrhnius relationship

$$C = C_0 \exp -\frac{Q}{RT}$$

Since heating is the easiest method to induce sintering, this expression permits us to model the grain growth as a function of time *and* temperature. This relationship is shown qualitatively in Figure 3.2d. This reinforces any material scientist's intuition that—yes, indeed—grains grow over time reaching a metastable size, and increasing the temperature increases the average metastable grain size.

Microscopic view of sintering offers us insight in controlling sintering and interpreting results. As previously mentioned, the reduction of surface area or surface energy drives sintering. At a microscopic scale, curvature is the driving force to merge to bodies, as in coalescence, or two grains, as in grain growth. The chemical potential μ of an atom to move from one body or grain to another is[1,9]

$$\mu_{coalecense} = \bar{V}\left(\frac{2\gamma_{sv}}{r_{sv}}\right)$$

$$\mu_{grain} = \bar{V}\left(\frac{2\gamma_{gb}}{D_{gb}}\right)$$

Chemical potential is proportional to molar volume $\bar{V}$ and surface energy γ (subscript sv refer to solid-vapor interface, gb grain boundary), and inversely proportional to either the radius of the particle r_{sv} or grain boundary D_{gb}. These simply stage that smaller particles will merge with larger ones in coalescence, or smaller grains will succumb to larger ones. This is shown in Figure 3.3.

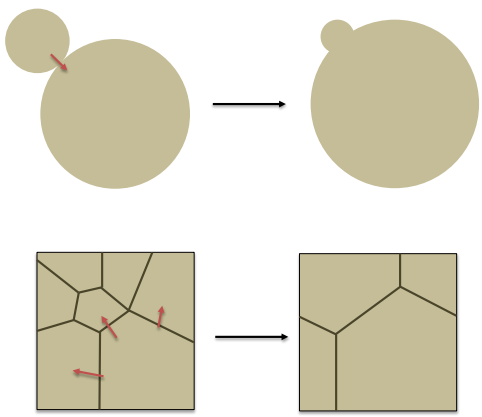

Figure 3.3. Microscopic driving forces of sintering

In this chapter we set out to explore the process sintering process to transform CdTe-Cl nanocrystal building blocks into polycrystalline films. We will start with the simplest process of solution deposition followed by heating to induce sintering. Our starting material is a binary compound with dilute amount of chloride creating the expectation for some exciting sintering phenomena. Ultimately, we will show how nanocrystal concentration will be used to control the grain structure permitting the tailoring of these polycrystalline films for various applications.

3.3 Methods

3.3.1 Materials

Chemical	Purity	prep	Supplier
Film Fabrication			
CdTe-Cl NCs	N/A	See Chapter 2 for synthesis	Me, Danny H.
Toluene	anhydrous, 99.8%	Dried over activated alumina, stored over 4A sieves at least 24hr before use	Sigma Aldrich
Toluene	anhydrous, 99.8%	As received	Sigma Aldrich
2-propanol (IPA)	anhydrous, 99.5%	As received	Sigma Aldrich
Methanol	anhydrous, 99.8%	As received	Sigma Aldrich
Dimethyl sulfoxide (DMSO)	anhydrous, 99.9%	As received	Sigma Aldrich

3.3.2 Sintered film formation

CdTe-Cl polycrystalline films were formed by sintering spin coated CdTe-Cl NC solution in an inert environment, unless specified otherwise. Native oxide/p^{++}-doped silicon substrates were cleaned by subsequent sonication in acetone and isopropanol, then dried with filtered nitrogen and finally exposed to air plasma (Herrick PDC-32G, high setting (18W) for 5 mins.) Substrates were then immediately brought into an argon glovebox. The CdTe-Cl NC solution was diluted with dried toluene to a desired concentration between 1-0.1 mM. A drop of this solution was deposited through a 0.2 μm PTFE filter onto a substrate affixed to a spin coater and subsequently rotated at 1,500 rpm for 30 sec. The NC film was sintered on a hotplate between 200-500°C for 10-600 sec as specified in the results. If multiple layers were desired, the film was let cool at least 20 sec on an aluminum block. In between layers, the film was rinse with various solvents including toluene (anhydrous, but not dried), IPA, methanol, and/or DMSO.

3.3.3 SEM

Scanning electron micrographs of sinter CdTe films were imaged using a *Zeiss Gemini Ultra-55* housed and maintained at the *Molecular Foundry* at *Lawrence Berkeley National Lab*.

Typically, film micrographs were imaged at an accelerating voltage of 3-5 kV and working distance of 2.8-5 mm and an aperture of 30 mm.

3.3.4 EDS

Elemental compositions of synthesized nanocrystals and sintered films were measured with an EDAX system typically operating at 10 kV, working distance of 10 mm, and variable aperture (often 60 mm).

3.4 Results

3.4.1 Single layers

Single layers of sintered CdTe-Cl exhibit recrystallization into a film with near-uniformity. Figure 3.4a is an illustration of the fabrication schematic accompanied with a typical cross sectional SEM images of as-deposited nanocrystals (NCs) and the resulting sintered film. The film in the SEM was deposited with a nanocrystal concentration ([NC]) of 0.5 mM at a spin coat speed of 1500 rpm and sintered at 350°C for 30 sec. During the sintering process, labile octylamine ligands desorbed from the nanocrystal surface in the initial nanocrystalline phase (average size ~5nm), which then recrystallizes into a second, polycrystalline film with grain size of 50-150 nm. A p-XRD pattern in Figure 3.4b captures this crystallographic transformation. The initial phase exhibits a predominately wurtzite crystal with nanocrystalline property as indicated by large peak broadening as predicted by the Scherrer relationship. The sintered phase shows a polycrystalline zinc blend crystal phase with some wurtzite phase impurities.[10,11]

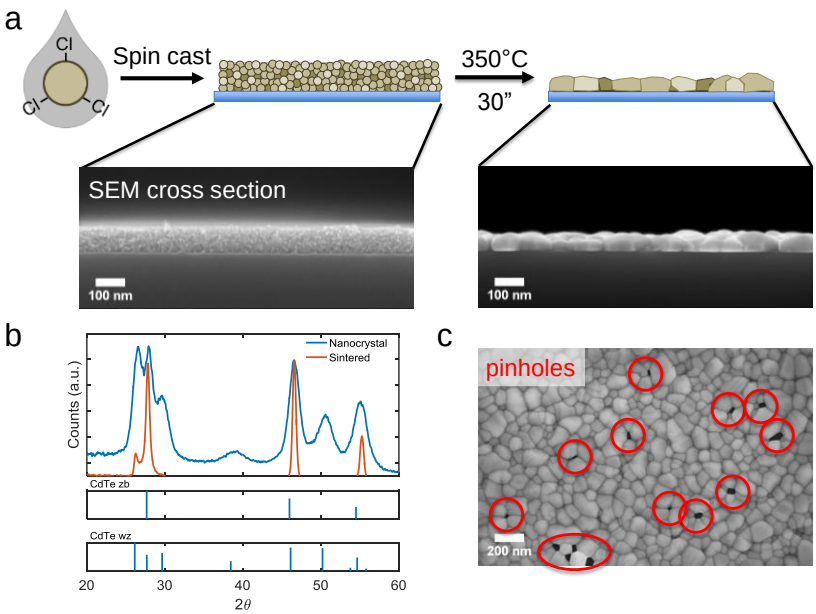

Figure 3.4. Sintering of a single layer of CdTe-Cl nanocrystals. (a) Illustration of sintering scheme with cross-sectional SEM images. (b) p-XRD of CdTe-Cl nanocrystals and sintered film. (c) Top-down SEM image of sintered films showing pinholes.

Due to the high void fraction of the initially deposited NC film, the film experiences significant dimensional changes. In typical sintering practice, the initial powder is compacted to

reduce suppress the formation of voids and/or minimize size contractions; this is not practiced here. The deposited NC film contracts from an initial thickness of 88±12 nm to 45±9 nm and the resulting polycrystalline film has an increased surface roughness compared to the initial NC film. Furthermore, the sintered film contains a high population of pinholes—holes spanning the height of the recrystallized films as shown in a top-down SEM image shown in Figure 3.4c. Pinholes cannot exist for opto-electrical applications that require the passage of current perpendicular to the plane of the film, but may be tolerated in applications in-plane. For example, solar cells require current to be passed orthogonal to the device stack; pinhole will lead to shunting rendering the device a mere resistor. Photoconductors, however, which pass charge through the film, may still function in the presence of pinhole.

As mentioned, during the sintering process, the labile octylamine ligands must desorb from the nanocrystal surface prior to, or during, nucleation and grain growth phases of recrystallization. TGA-DCS and FTIR was implemented to characterize the sintering process. The desorption temperature of octylamine is likely near boiling point, which is 175-177°C.The TGA-DCS sample was exposed to prolonged vacuum (~100 mtorr) to ensure all mass loss and heat changes were not caused by evaporating solvent molecules. The TGA-DCS result is shown Figure 3.5a. Mass loss onset begins around 150°C, reaches maximum mass rate just above 200°C, and ends by 350°C, yielding a total of 10% mass loss (assuming nearly all mass loss was octylamine.) The peak mass loss is just above the boiling point of octylamine, suggesting the desorption point is just above 200°C. Desorption of octylamine from the NC surface is accompanies with a net flow of heat to the sample, which is expected for desorption of a volatile species. Peak negative heat flow lies closely with the peak mass loss rate just above 200°C, corroborating ligand desorption temperature. During sintering, the reduction of surface energy is manifested as positive heat flow. Peak positive heat flow occurs just below 400°C. These two heat flow peaks are separated by over 150°C degrees showing that ligand desorption and sintering occur in two events. However, it is hard to be certain that these two event do not overlap. In the case that they do, we would expect both desorption and sintering occur below their respective heat flow peaks.

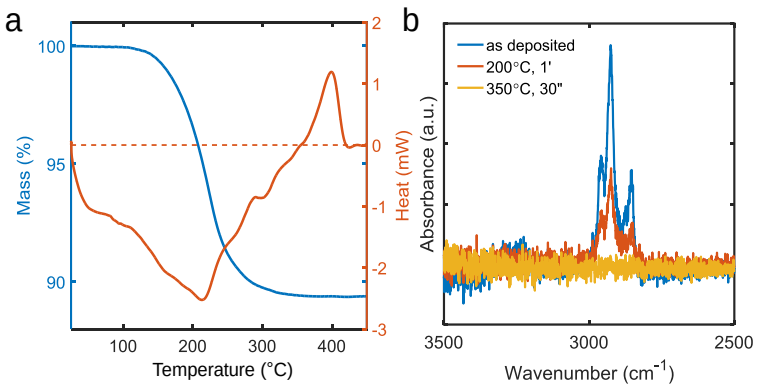

Figure 3.5. Characterization of thermochemistry and volatile organic component of CdTe-Cl nanocrystal before and after heating. (a) TGA-DSC data. (b) FTIR spectrum of ~300 nm film.

FTIR supports the conclusions from the TGA-DSC data. Here, the FTIR spectrum was measured for three ~300 nm films deposited on silicon with identical spin speed and [NC]. Figure 3.5b shows the FTIR spectrum window of 2500-3500 cm^{-1} where the C-H vibrations in the octlyamine alkyl chains should exist. A noticeable decrease in the C-H signal is observed between the as-deposited and the film gently heated for 200°C for 1 min, near the desorption temperature. The film heated at 350°C for 30 sec confirms the successful removal of the octylamine component of the colloidal CdTe-Cl building block. Any residual organic component is expected to reduce the electrical conductivity and light-absorbing properties of the sintered films reducing their expected performance in opto-electrical applications.

Single layered sintered NC films are rapidly formed from nanocrystalline precursor films at short time lengths and moderate heating. A layer of NCs with average size of 5 nm can be quickly transformed into a polycrystalline film with grain size 50-150 nm is an impressive feat for integrating this solution-processed material into low cost commercial manufacturing lines. During the sintering process, the octylamine ligands desorb just above 200°C and sintering and grain growth occurs above 300°C. One major limitations is the formation of pinholes, rendering these films inadequate for solar cell applications that pass charge orthogonal to the film plane.

3.4.2 Multilayered: Influence of [NC]

This method of sintering NCs into polycrystalline films produces fairly thin films that may limit their applications. For example, films on the order of a micron are needed to achieve upwards of 100% absorption near the band gap for a dense film. Pinholes reduce the density and therefore average absorbance (if normalized by volume), reduce electrical performance, or provide shunt pathways in layered device architecture such as solar cells. A layer-by-layer method can be implemented to build up thicker films to enhance absorbance.[12–14] In this film fabrication scheme, a layer of NCs is deposited and sintered. Once sintered, another layer of NCs is deposited and sintered. This process is repeated to create thicker films. NC deposited in each layer fill the voids form in sintering reducing pinhole formation. This method can also be exploited to control the grain structure when an understanding of recrystallization and grain growth are considered.

Grain structure can be controlled by the amount of nanocrystals deposited during each sintered layer. When a thick layer of NCs is deposited at each layer, grainy film populated with voids and pores is expected. On the other hand, a dense film with columnar grain structure will evolve when each layer deposits a thin layer of NCs. For colloidal NCs deposited from solution, nanocrystal concertation ([NC]) can be used to control, the thickness, or amount, or NCs in between each layer. Figure 3.6 illustrates how [NC] can control grain structure control in layer-by-layer sintering of NC films.

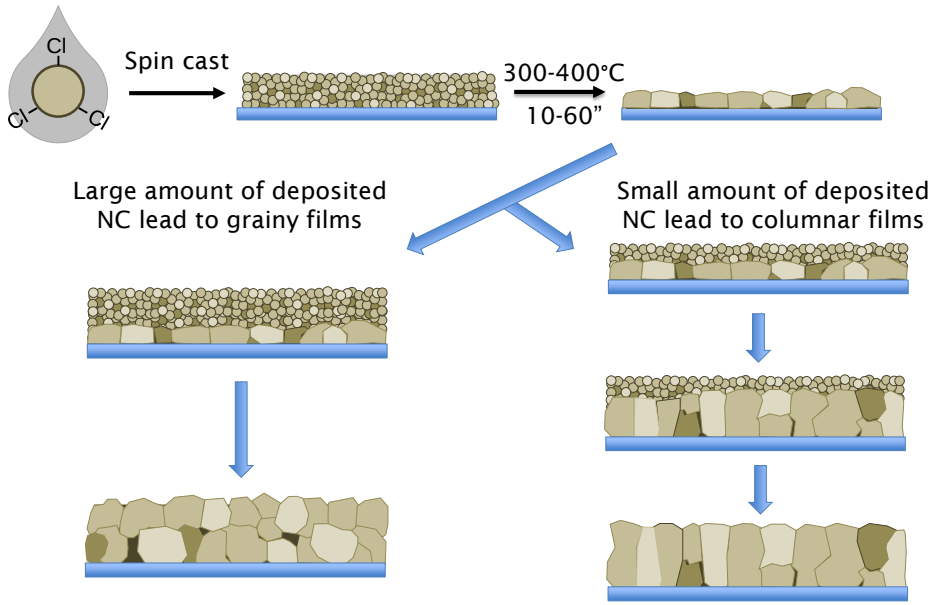

Figure 3.6. Illustration of grain structure control in layer-by-layer sintered films.

Recrystallization and grain growth theory can be invoked to show how [NC] will determine grain structure. We know that heterogenous nucleation occurs at a greater rate than homogeneous nucleation. The initial sintered layer in the layer-by-layer process is called the “seed” layer. In the sintering process, the NCs at the interface with the underlying sintered layer will undergo heterogeneous nucleation creating a burst of nucleation at this polycrystalline-NC interface. NCs far from this interface will experience the slower homogenous nucleation forming far fewer nuclei. Once nuclei form, coalescences and grain growth is expected to occur at a similar rates regardless of the nucleation process. One can envision a crystallization front moving upwards into the NC layer, incorporating NCs and nuclei formed from homogenous nucleation. If the NC layer is thin, the homogeneous nuclei will be small and the driving force high to merge with the incipient grain front. In this regime, called the *low [NC]*, we expect the grain structure to be columnar and dense. If this NC layer is thick, the moving grains interface will encounter larger and larger grains derived from homogenous nucleation with a decreasing driving force to merge. In this *hi [NC]* regime, films will be grainy and full of voids or pores. The major tradeoff between these two regimes is the number of layers required to achieve the same thickness; lower [NC] need many more layers than films fabricated with higher [NC].

The first layer in the layer-by-layer (LBL) method is called the *seed* layer and the grain structure is important in understanding the grain structure of the LBL film. Figure 3.7 shows SEM images of sintered films formed from a single layer of NCs with decreasing [NC]. The films formed at the highest [NC] is thick and has a larger average grain size compare to the films from the lowest [NC]. In fact, the film formed at 0.12 mM is non-continuous with. Here, the pores manifest as voids in the film creating a lattice-like appearance. The film from [NC] = 0.48 mM has voids at the top and bottom of the film creating pores. Observing the first layer already begins to support the notion that films formed from high [NC] will yield a porous film.

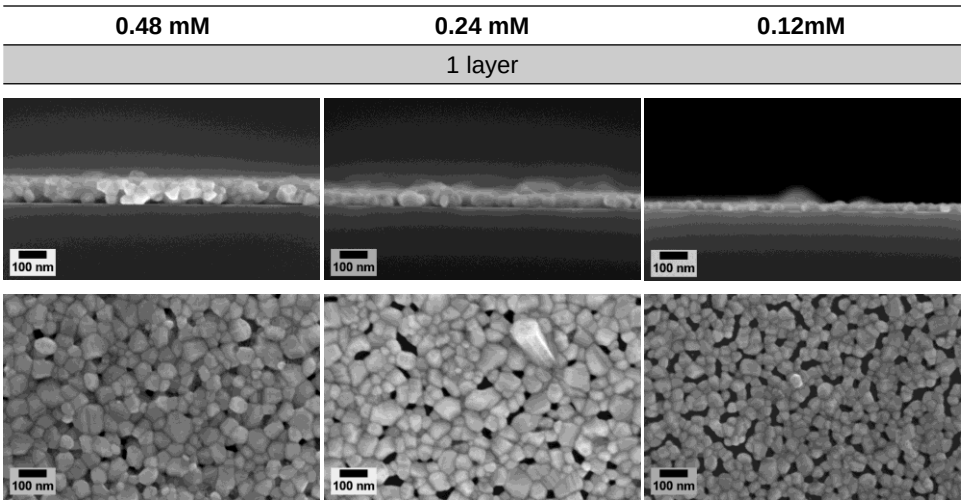

Figure 3.7. SEM images of a single layer of sintered CdTe-Cl NCs.

Films are grown from the seed layers by sintering multiple NC layers controlling the morphology using the [NC] of the depositing NC solution. As [NC] is decreased from 0.48 mM to 0.12 mM the film structure changes from porous and grainy to continuous columns as shown in the cross-sectional SEM images in Figure 3.8. This is consistent with our understanding of recrystallization from nucleation to grain growth. A dominant zinc blend crystal structure for the CdTe films is confirmed by p-XRD for all three films reported in Figure 3.9. However, all three films exhibit some wurtzite crystal character. This are most likely the result of a high population of stacking faults or other defects that change the ABCABC plane order in zinc blende to ABABAB in wurtzite. Interestingly, the film grown with [NC] = 0.48 mM has a significantly larger wurtzite compent compared to the other two films. The {111} peak in 0.48 and 0.12 mM is significantly reduced compared to the {200} and {311} suggesting a crystal orientation with respect to the substrate. However, this claim must be supported by more rigorous XRD techniques to produce a pole plot.

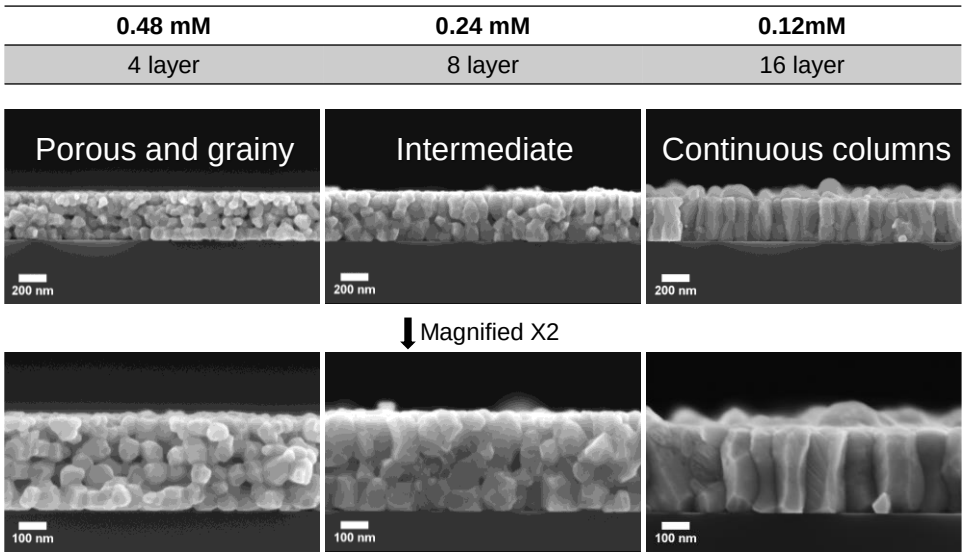

Figure 3.8. Cross-sectional SEM images of sintered films showing the effect of NC concentration on the resulting grain morphology.

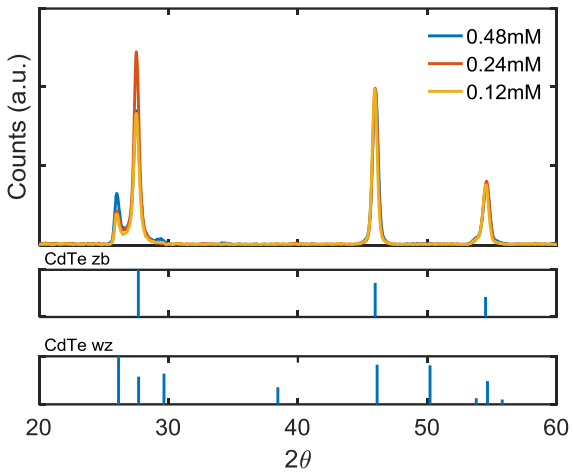

Figure 3.9. p-XRD of sintered films in Figure 3.8.

Many physical properties of CdTe films are determines by the grain structure. Controlling the morphology is the first step in engineering a films for a specific application. For example, we expect that a dense films with continuous, columnar grains are ideal for devices that require the transfer of charge orthogonal to the film plane, such as a solar cell.

3.4.3 Temperature and grain size

Temperature is a dramatic determiner of recrystallization and grain growth dynamics. Increasing temperature adds more energy to a system to overcome activation barriers. In these sintered films higher temperature increases nucleation rate and speeds up grain boundary diffusion. This translates to larger meta-stable grain size as predicted by the generalize grain growth equation.

Increasing the temperature at which each layer of sintered NC increases the average grain size in the films. To demonstrate this effect, three films were made using [NC] and time that is known to yield columnar grains at 350°C: [NC] = 0.12 mM and a sintering time of 30 sec. Using these conditions, three films were made at three temperatures: 300, 350, and 400 °C. Cross sectional SEM images and average grain size are reported in Figure 3.10 below.

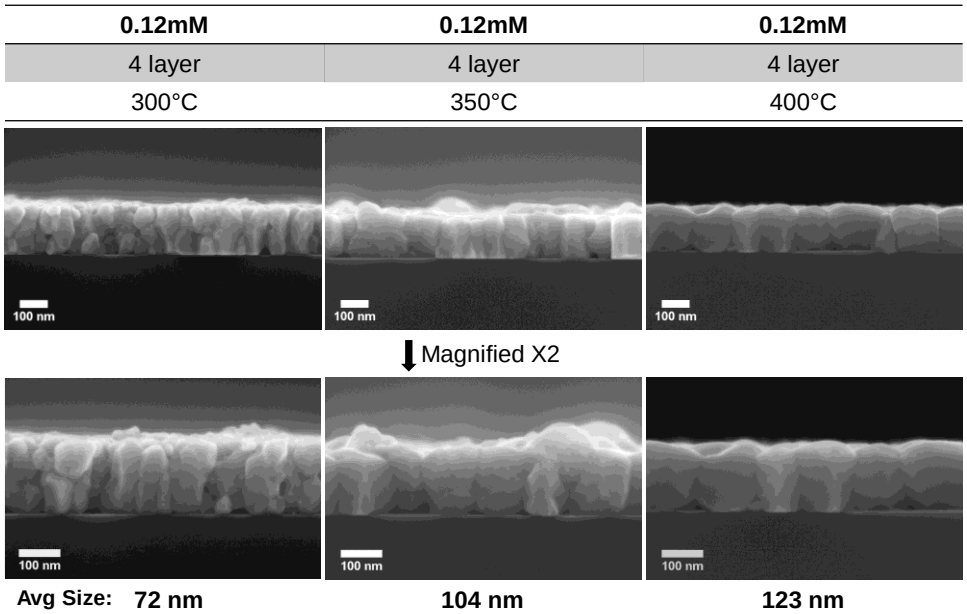

Figure 3.10. Cross sectional SEM images of sintered films showing effect of sintering temperature on grain structure.

Higher temperature not only increases the average grain size, but also increases the quality of the columnar grains. This is not unlike the effect of [NC] on the grain structure of the sintered films. At the low temperature, we observe a mix mode of columns and what appears to be "broken" columns, like an ancient Roman ruin. This is the result of two effects caused by lower temperature: (1) recrystallization theory shows that the phase change is slower at a lower temperature (Figure 3.2b) and (2) the grain growth equation shows the meta-stable grain size is smaller with lower temperature (Figure 3.2d.) Therefore, the combination of slower nucleation and grain boundary diffusion results in incomplete grain growth and a smaller size limit. At the high temperature regime, recrystallization is rapid and the meta-stable grain size is larger. This is obvious with large grains with nearly parallel grain boundaries perpendicular to the substrate.

3.4.4 Chloride composition and rinsing

Elemental composition of sintered films is also an important characteristic to track along with grain structure. In fact, these two properties may be linked: films with higher GB populations should have a higher chlorine content. CdTe films exposed to a *chloride activation* treatment have a chloride composition of 1-2% for both conventionally grown films[15] and sintered CdTe NCs,[14] measured with XPS and assumed to be a bulk value. In grain boundaries, the chloride content is about 25% greater than the grain interior.[16] Our CdTe-Cl NC building blocks have a 5-6% chloride

content. Therefore, we expect that these films will experience and excess of chloride. If there is a saturation concentration 1-2%, where does the excess chloride go?

Compositional analysis on the films displayed in Figure 3.8 and Figure 3.10 show chloride content is dependent on [NC] and temperature. Top-view SEM images of the films and EDS results are shown in Figure 3.11. The SME images reveal a high-contrast feature spotting the film surface for the 0.12 mM film. EDS mapping (data not shown) showns that these regions have a higher chlorine content than surrounding areas suggesting these are $CdCl_2$ crystals. Similar features were witnessed in sintered CdSe-Cl NC films and identified as $CdCl_2$.[17] The two higher [NC] films appear to have a highly porous top layer compared to the 0.12 mM film. This is consistent with the grain structure observed from the cross-section in Figure 3.8. The EDS results of these three films reveals that the chloride content decreases with increasing 0.12 mM.

[NC]	0.48 mM	0.24 mM	0.12 mM
Layers	4 layers	8 layers	16 layers
Temp.	350°C		
Time	30 s		
Side View	See Fig XXX		
	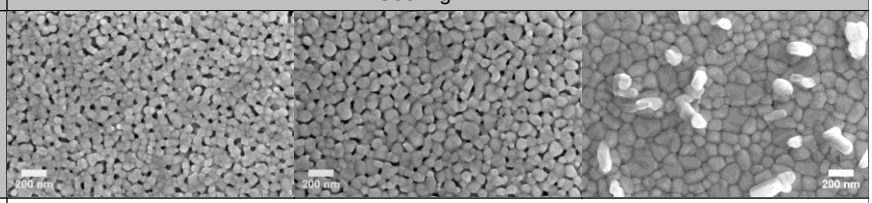		
Elem.	EDS Atomic %		
Cd	48.7	50.0	49.6
Te	45.9	45.2	46.0
Cl	5.4	4.8	4.4

Figure 3.11. SEM images and EDS results from films sintered with varying [NC] in Figure 3.7.

Chloride content significantly decreased with increased temperature according to EDS measurements on the films from Figure 3.10. Top-view SEM images and EDS results are presented in Figure 3.12. Observing the top layer of the three films, we notice that the top layer of the films have fewer pores as the temperature increases. This is consistent with the grain structure seem from the corresponding cross-sections of these films (Figure 3.10)—the more continuous the columnar structure, the less porous the top layer. However, there appears to be an anomaly in the presence of surface $CdCl_2$: only the film sintered at 350°C appears to possess these high-contrast features. Regardless of the surface $CdCl_2$, there is a strong correlation between high sintering temperature and reduced chloride content.

Chloride content and the presence of surface chloride can easily be explained by (1) the high segregation energy of chloride in CdTe GBs and (2) the temperature dependence of $CdCl_2$ vapor pressure. As previously mentioned, chloride has a favorable segregation energy in the CdTe GBs that encourage Cl concentration more than 25% higher than the surrounding CdTe.[16] In addition, $CdCl_2$ has a vapor pressure that increased with temperature.[18] A grainy film has a high

population of GBs that can therefore absorb a high concertation of chloride acting like a chloride sponge. These films have high Cl content and no visible surface $CdCl_2$: Figure 3.11 left and center films, Figure 3.12 left film. Films sintered at high temperatures will have no surface $CdCl_2$ as it will have sublimed, and a lower Cl content due to lower GB population caused by large grains enabled by a higher temperature. These films have low Cl content and no visible surface $CdCl_2$: Figure 3.12 left film. Then there is the space in the middle: relatively low chloride content with visible surface $CdCl_2$. These films have columnar grains and low GB population, but are sintered at a temperature that permits the build-up of surface $CdCl_2$.

[NC]	0.12 mM		
Layers	8 layers		
Temp.	300°C	350°C	400°C
Time	30 s		
Side View	See Fig XXX		
	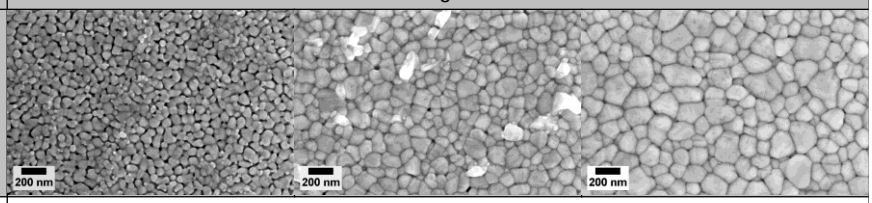		
Elem.	EDS Atomic %		
Cd	48.4	49.1	49.6
Te	47.5	48.4	49.6
Cl	4.1	2.5	0.8

Figure 3.12. SEM images and EDS results from films sintered at increasing temperature in Figure 3.10.

Next, we further explored the how chloride content and the presence of surface $CdCl_2$ was affected by sintering time and solvent solubility. We've established that CdCl2 may sublime from the surface. This is both a function of temperature and time—higher temperature speeds sublimation, while longer time for a given temperature will reduce the surface chloride. An ionic crystal, $CdCl_2$ is soluble in polar solvents as shown in Table 3.1.[19,20] In all previous films, isopropanol (IPA) was used as the intra-layer solvent. $CdCl_2$ was not found in the solubility tables. IPA is less polar than ethanol (EtOH). Using the MeOH and EtOH solubility values, we can extrapolate that value for IPA is to be around 1 g/ml. Therefore, we expect a lower Cl content *and* surface $CdCl_2$ when rinsing with a more soluble solvent.

Table 3.1. $CdCl_2$ solubility in polar solvents.

Solvent	CdCl2 solubility (g/ml)
EtOH	1.48
MeOH	2.15

DMSO	18

Films fabricated using low [NC] were fabricated to explore our understanding of the effect of solvent polarity and sintering time on the Cl content and surface $CdCl_2$. Fabrication parameters, SEM images of the films, and EDS results are presented in Figure 3.13. Compared to the control films (Figure 3.13, left), we increased the time 4-fold (center) and then increased the polarity of the solvent by using methanol (right.) All film exhibit similar film morphology—generally continuous columnar grain with few pores visible form the top. The control film has a significant population of $CdCl_2$ surface crystals, while the other two films have sparse coverage of small high-contrast features that are likely $CdCl_2$. In both the longer time and MeOH films, the Cl content has been significantly reduced. EDs error is around 1% suggesting that these two method are similarly effective at reducing both the Cl content and surface CCl_2.

[NC]	0.12 mM		
Layers	8 layers		
Temp.	350°C		
Time	30 s	120 s	30 s
Rinse	IPA		MeOH
	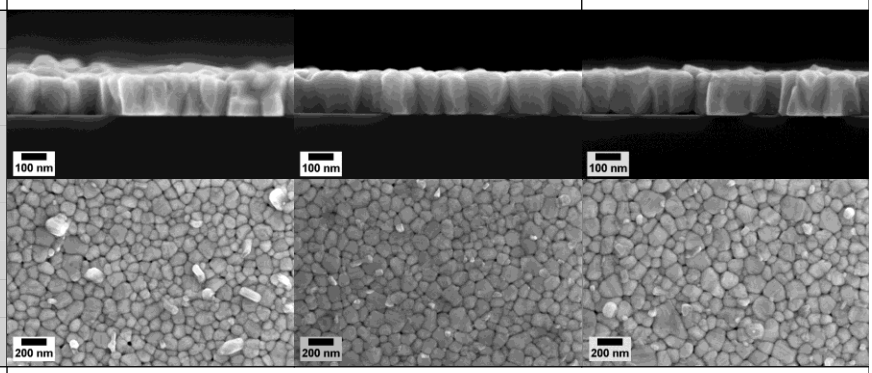		
Elem.	EDS Atomic %		
Cd	48.9	49.3	49.3
Te	47.5	49.4	49.1
Cl	3.6	1.3	1.6

Figure 3.13. SEM images and EDS results from films fabricated with different intra-layer rinsing solvents.

The presence of excess $CdCl_2$ on the film surface has implication on grain growth. Grain boundary pinning in a phenomena where an insoluble species retards the diffusion of grain boundaries resulting in suppressed grain growth. Therefore, controlling the excess $CdCl_2$ is paramount to controlling the film structure. At this point we know that increasing temperature and intra-layer rinsing are powerful methods to reduce surface $CdCl_2$.

Increasing solvents solubility and increasing temperature both promoted larger grain growth. A parameter space of two different temperatures and two solvents were used in addition

to no rinsing was explored. Film fabrication conditions and SEM images are presented in Figure 3.14. At 350°C, increasing the solubility of $CdCl_2$ leads to larger grain growth and less visible surface $CdCl_2$ (Figure 3.14, films A-C). DMSO is a very strong solvent for $CdCl_2$ and leads to the largest grains. We observe a strange circular pattern for the surface $CdCl_2$. This is a result of rinsing the surface with DMSO in which $CdCl_2$ is readily soluble followed by toluene, which $CdCl_2$ is insoluble. Having a low vapor pressure, DMSO requires much longer tie to dry off the films during spinning; in this experiment, toluene was added before DMSO complexly dried leading to the $CdCl_2$ to rapidly recrystallize in a droplet-like shape.

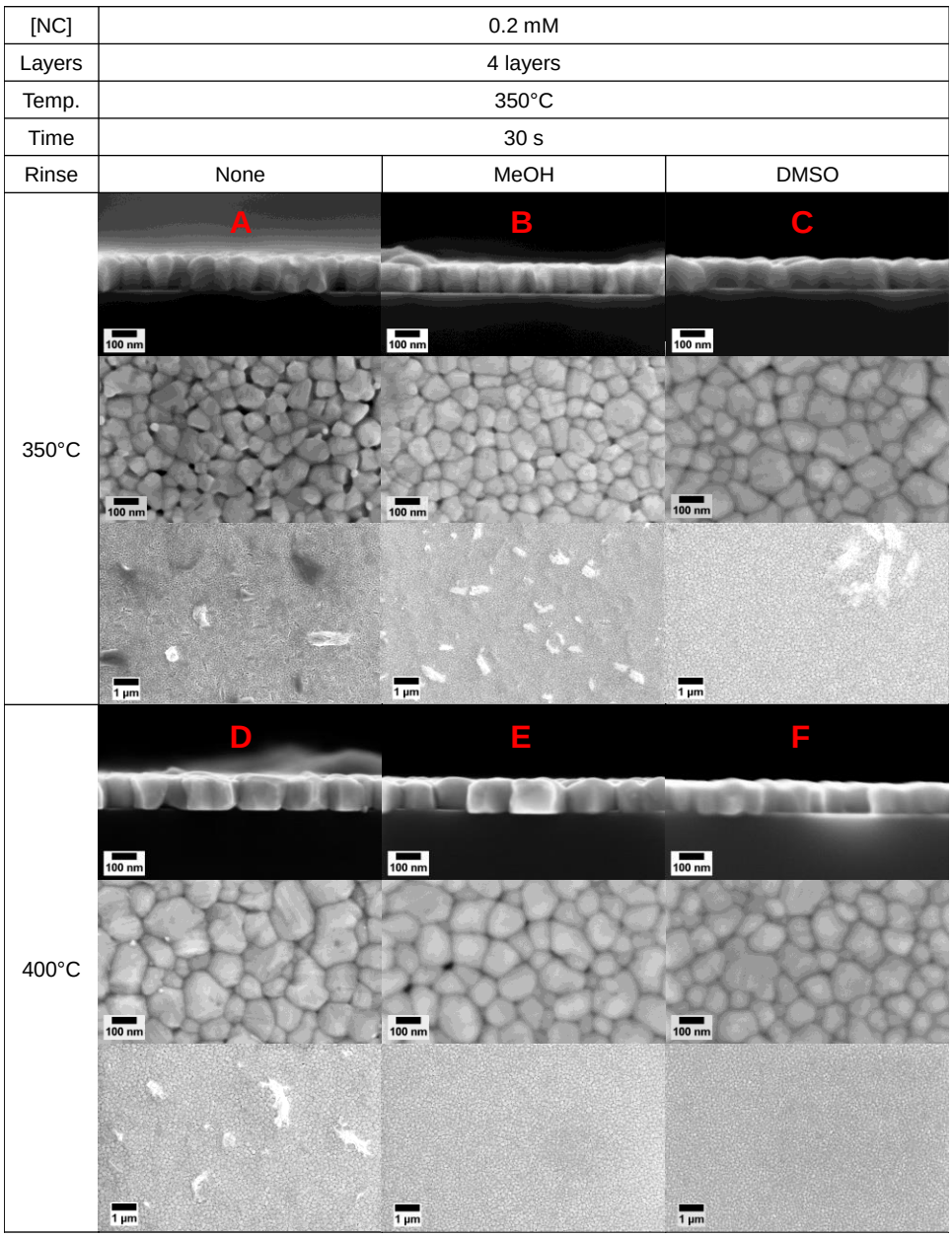

Figure 3.14. Films with 3 difference intra-layer rinses at 350 and 400°C.

Increasing the temperature to 400°C reduces the importance of the solvent polarity. All films sintered at this temperature show large grain growth—larger than the films sintered at 350°C, which is consistent with the grain growth equation and previous results (Figure 3.10.) However, a surface $CdCl_2$ is still prevalent on the films not exposed to a solvent (Figure 3.14, film D), whereas no surface $CdCl_2$ is observed in films that have been rinsed with a solvent with 2.15 mg/ml or higher (Figure 3.14 films E and F.) Therefore, higher temperature reduces the importance of the solubility strength.

The presence of excess $CdCl_2$ influences the grain structure by inhibiting growth. However, the amount $CdCl_2$ on the surface depending on the solvent rinse and the time and temperature at which sintering occurs. Less excess $CdCl_2$ can accumulate if it is removed from rinsing or sublimation as previously discussed. We present a simple model to frame these interconnected physical processes by identifying the simplest and most obvious processes in Figure 3.15. First, $CdCl_2$ has a solubility limit in the CdTe. $CdCl_2$ beyond this amount—the excess bulk $CdCl_2$—must diffuse to the surface, which is presumably faster at higher temperatures. Surface $CdCl_2$ sublimes from the surface—this is similarly dependent on time and temperature. Any excess $CdCl_2$ remaining after the sintering and rinsing process will act to inhibit grain growth via grain boundary pinning illustrated at the bottoms of Figure 3.15.

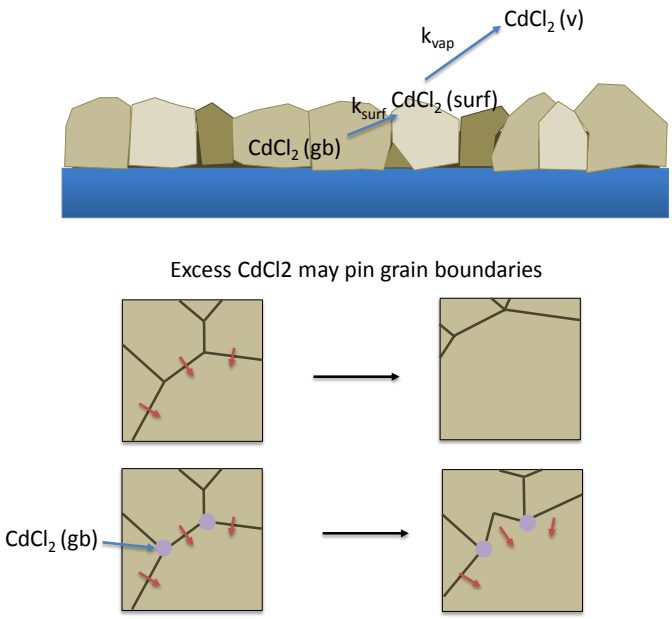

Figure 3.15. Schematic to influence of excess CdCl2 on grain structure.

3.4.5 Incorporation of oxygen

Oxygen is a parameter that conventional films processes report as important to electrical conductivity. Previous studies claim that oxygen promotes grain growth, suppresses grain growth, facilitates defect formation, and creates oxides that change grain boundary migration as well as facilitate better doping. The best sintered CdTe NC solar cells are sintered in air, but at an exact

temperature and time—sinter too long and they authors claim the film over-oxidized.[12] In this subsection we seek to observe how sintering in air influences the grain morphology.

Films sintered in air with a high [NC] exhibit less faceted grains. Cross sectional SEM images and fabrication conditions for a simple experiments are shown in Figure 3.16. The grains in the air-sintered film appear to be smoother and less faceted compared to the one sintered in an inert environment. There is a hypothesis that the CdTe-oxide create some eutectic point that permit better grain boundary movement.

[NC]	1 mM	
Layers	1 layers	
Temp.	350°C	
Time	30 s	
Rinse	None	
Env.	Ar	Air
	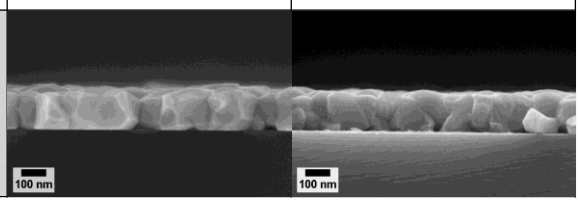	

Figure 3.16. Infleunce of oxygen on grain morphology.

Grain structure in these sintered CdTe-Cl NC films has shown to be influenced by both excess $CdCl_2$ and oxygen in the sintering environment. Solvents have shown to have reduce the excess $CdCl_2$ leading to larger grain growth with fewer pores. TO understand how these two grain growth promoted interplay, we changed both the solvent and sintering atmosphere in sintered films in the high [NC] regime (i.e. grainy and porous.) Sintering conditions and SEM images are presented in Figure 3.17. The control film, A, was sintered with IPA and in an inert environment. Increasing the solvent solubility value (using MeOH over IPA) yielded a dramatically denser film as seen with film B as indicated by film thickness. If the films was rinsed with IPA but sintered in air, the film was slightly denser, seen in film C. Rinsing with methanol also yielded a top layer with pores, but no cracks as seen in the other two films. These results suggest that excess $CdCl_2$ has a strong effect on the grain morphology than the sintering environment. However, the effect of air cannot not be discounted.

[NC]	0.5 mM		
Layers	4 layers		
Temp.	350°C		
Time	30 s		
Env.	Argon	Argon	Air
Rinse	IPA	MeOH	IPA

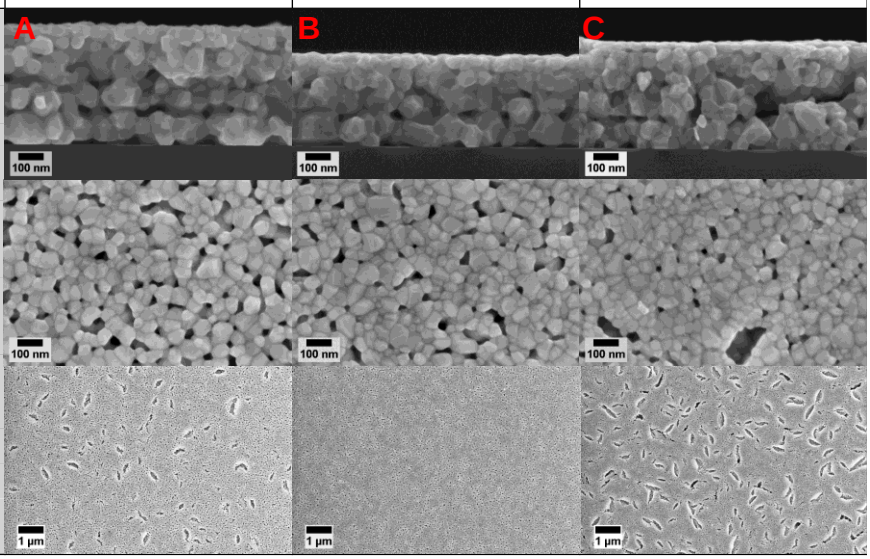

Figure 3.17. Influence of intra-solvent rinse and air on grain morphology at *high* [NC].

Employing several parameters demonstrate the range of control we have over these layer-by-layer sintered films. Inter-layer solvent removes excess surface $CdCl_2$ to achieve films with larger grains and fewer pores while the presence of air promotes less faceted grain growth. In this final experiment, we show that in the low [NC] regime, sintering in air with solvent lead to the dense films. In this experiment, solvent polarity was increased, and one film was rinse with IPA while being sintered in air. The sintering conditions and SEM images are present in Figure 3.18. The control sample, Film A, was sintered in argon and exhibits poor columnar grain structure and significant surface $CdCl_2$. As the solvent $CdCl_2$ solubility value increased from IPA (film B) to MeOH (film C), the film become less grainy and porous. The reduction in porosity from A-C is evident from the top-view. As porosity is reduced yielding a denser film, the thickness decreases as seen in the cross sectional SEM images. Finally, the film rinsed with IPA and sintered in air produced the films with lowest pore population seen from the top-view and densest films evidenced by the thinnest film from the cross section. The grain structure also exhibits a "smooth" texture compared to the more faceted appearance of films sintered in an inert environment.

[NC]	0.2 mM			
Layers	5 layers			
Temp.	350°C			
Time	30 s			
Env.	Argon	Argon	Argon	Air
Rinse	None	IPA	MeOH	IPA

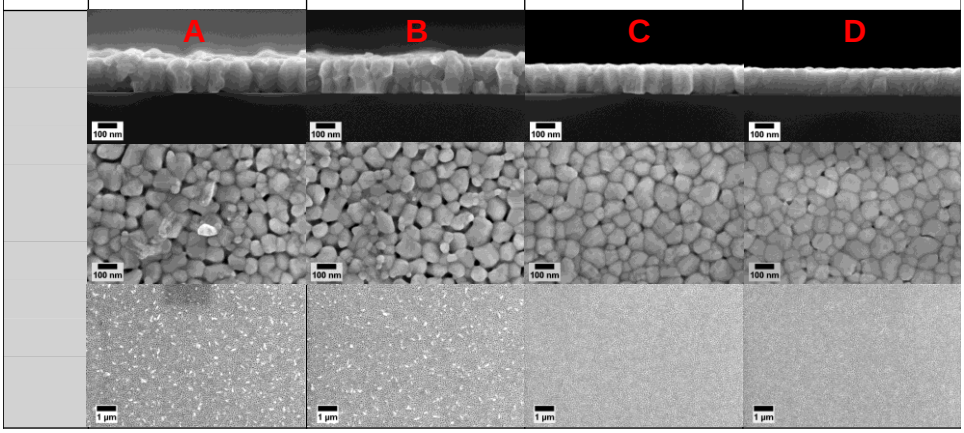

Figure 3.18. Influence of intra-solvent rinse and air on grain morphology at high [NC].

3.5 Conclusion

Layer-by-layer sintering CdTe-Cl NCs into polycrystalline films has demonstrated to be a highly complex physical and chemical transformation with seemingly endless parameter space. We presents a simple model that highlights the most obvious physical processes. Although the removal of $CdCl_2$ is desirable for large grains growth, there is an unknown amount that must remain that facilitates grains growth and improve the electrical properties of the film. Without additional characterization methods need to be implemented to track the crystal structure as a function of treatment. Most importantly, electronic characterization needs to be implemented to show synergies between grain structure and crystallographic purity.

3.6 References

(1) Kang, S.-J. L. *Sintering: Densification, Grain Growth, and Microsctructure*; Elsevier: Burlington, MA, 2005.

(2) Rahaman, M. N. *Sintering of Ceramics*; 1st ed.; CRC Press: Boca Raton, 2008.

(3) Barsoum, M. In *Fundamentals of Ceramics*; McGraw-Hill: New York, 1997; pp. 331–390.

(4) Chen, I.; Wang, X. *Nature* **2000**, *404*, 168.

(5) F.J. Humphreys and M. Hatherly. *Recrystallization and Related Annealing Phenomena*; 2nd ed.; Elsevier B.V., 2004.

(6) Harada, M.; Kamigaito, Y. *Langmuir* **2012**, *28*, 2415.

(7) Kirsch, B. L.; Richman, E. K.; Riley, A. E.; Tolbert, S. H. *J. Phys. Chem. B* **2004**, *108*, 12698.

(8) Avrami, M. *J. Chem. Phys.* **1939**, *7*, 1103.

(9) Ohring, M. *Material Science of Thin Films: Deposition and Structure*; 2nd ed.; Academic Press: San Diego, 2002.

(10) Peng, X.; Manna, L.; Yang, W.; Wickham, J.; Scher, E.; Kadavanich, a; Alivisatos, A. *Nature* **2000**, *404*, 59.

(11) Manna, L.; Scher, E. C.; Alivisatos, a. P. *J. Am. Chem. Soc.* **2000**, *122*, 12700.

(12) Jasieniak, J.; MacDonald, B. I.; Watkins, S. E.; Mulvaney, P. *Nano Lett.* **2011**, *11*, 2856.

(13) MacDonald, B. I.; Martucci, A.; Rubanov, S.; Watkins, S. E.; Mulvaney, P.; Jasieniak, J. J. *ACS Nano* **2012**, *6*, 5995.

(14) Panthani, M. G.; Kurley, J. M.; Crisp, R. W.; Dietz, T. C.; Ezzyat, T.; Luther, J. M.; Talapin, D. V. *Nano Lett.* **2014**, *14*, 670.

(15) Niles, D. W.; Waters, D.; Rose, D. *Appl. Surf. Sci.* **1998**.

(16) Li, C.; Wu, Y.; Poplawsky, J.; Pennycook, T. J.; Paudel, N.; Yin, W.; Haigh, S. J.; Oxley, M. P.; Lupini, A. R.; Al-Jassim, M.; Pennycook, S. J.; Yan, Y. *Phys. Rev. Lett.* **2014**, *112*, 156103.

(17) Norman, Z. M.; Anderson, N. C.; Owen, J. S. *ACS Nano* **2014**, *8*, 7513.

(18) George, L. C.; Doerr, R. M.; Visnapuu, A. *J. Chem. Eng. Data* **1969**, *14*, 23.

(19) Seidell, A. *Solubilities of inorganic and metal organic compounds*; 3rd ed.; Van Nostrand: New York, 1940.

(20) Gaylord Chemical Company. Dimethyl Sulfoxide (DMSO) Solubility Data, 2007.

4 Chapter 4: Solar cells from solution-processed, sintered CdTe-Cl nanocrystal films

4.1 Introduction

Cadmium telluride solar cells have recently made strides in both modular and lab-scale efficiency, the later reaching greater than 21%.[1] Achieving these efficiency milestones has brought great optimism for thin film solar cell efficiency to compete with crystalline silicon. With a theoretical limit at AM1.5 around 30%, CdTe solar cells have room for improvement but may be limited by poor understanding of the electronic properties of the cadmium telluride film. This film undergoes a complex reaction with chloride upon thermal treatment to achieve improved performance, a step called "chloride activation."[2–4] Fortunately, recent research findings have started to elucidate the role of chloride in CdTe films: the chloride dopes the grain boundaries facilitating better charge separation and transport.[5–10] All record setting devices are sproduced from CdTe films fabricated by physical vapor deposition, a deposition method with throughput and material usage limitations, and potentially high operational costs due to vacuum and heating energy demands.[2] Nanocrystals offer an alternative path to polycrystalline thin film fabrication by means of solution processing.[11–14] Solar cells fabricated from sintered CdTe NCs have rapidly increased in efficiency with the most recent report over 12%.[13]

Recent findings reveal that chloride (Cl) atoms preferentially segregate at CdTe grain boundaries and facilitate charge separation and transport[5–8,15]. Therefore, controlling grain structure is imperative to developing high performing CdTe solar cells. We propose an alternative to standard physical deposition methods: sintered CdTe nanocrystals surface modified with chloride (CdTe-Cl NC) deposited from solution. By eliminating the "$CdCl_2$ activation" step in conventional methods, sintering layers of CdTe-Cl NC building blocks promises better control over grain structure that will yield better performance with higher throughput and lowered costs.

In this chapter, we aim to utilize semiconductor nanocrystals as a means to controllably study the effect of chlorides and other processing conditions on grain boundaries. Nanocrystal surface chemistry, as discussed in Chapter 2, permits control on the chlorine content introduce permitting meticulous studies on the influence of the halide on the film. A solution-processed method to efficient CdTe films promises a more robust, and perhaps lower cost route to achieving high-efficient thin film solar cells.

4.2 Methods

4.2.1 Materials

Chemical	Purity	prep	Supplier
Film Fabrication			
CdTe-Cl NCs	N/A	See Chapter 2 for synthesis	Me, Danny H.

Toluene	anhydrous, 99.8%	Dried over activated alumina, stored over 4 Å sieves at least 24hr before use	Sigma Aldrich
Toluene	anhydrous, 99.8%	As received	Sigma Aldrich
2-propanol (IPA)	anhydrous, 99.5%	As received	Sigma Aldrich
Methanol	anhydrous, 99.8%	As received	Sigma Aldrich
ZnO sol-gel			
Zinc acetate dihydrate	≥98%	As received	Sigma Aldrich
Ethanolamine, purified by redistillation	≥99.5%	As received	Sigma Aldrich
2-methoxyethanol	97%	As received	Sigma Aldrich
Contacts			
Aluminum evaporation slug	99.999%	As received	Sigma Aldrich
Solar cell substrates			
Indium tin oxide on glass, 10 x 14 mm, 145±10 nm thick	20±2 ohms/sq.	As received	Thin Film Devices

4.2.2 Sintered film formation

CdTe-Cl polycrystalline films were formed by sintered spin coated CdTe-Cl NC solution and annealed in an inert or air environment adopting previous methods.[12,13] Indium tin oxide on glass substrates were cleaned by subsequent sonication in acetone and isopropanol for 5 mins each, then dried with filtered nitrogen, and finally exposed to air plasma (Herrick PDC-32G, 200 mTorr air, high setting (18W) for 5 mins.) Substrates were then immediately brought into an argon glovebox. The CdTe-Cl NC solution (dispersed in toluene) was diluted with dried toluene to a desired concentration between 0.1-1 mM. A drop of this solution was deposited through a 0.2 µm PTFE syringe filter on a substrate affixed to a spin coater and subsequently rotated at 1500 rpm for 30 sec. The NC film was sintered on a hotplate between 250-500°C for 10-120 sec as specified in the results. For multiple layers, the film was let cool at least 20 sec on an aluminum block. In between layers, the film was rinsed with various solvents including toluene (anhydrous, but not dried), IPA, methanol, and/or DMSO, as specified in the results, using 20 drops each. *If* a polar solvent was used, a 20 drop toluene rinse preceded, and finished with ~10 drops toluene prior to the next layer. All solvents used to rinse were filtered through 0.2 µm PTFE syringe filter and 20 drops were deposited while the substrate was spinning at 1500 rpm.

Several measures were taken to avoid "comet" formation during each layer. First, the syringe filter tip for the NC solution was kept in toluene between depositions to ensure that NCs did not dry on the tip creating particles. Second, substrate were handled (cleaning, transferring to/from plasma chamber and glovebox) in a Teflon microscope slide cover rack (a.k.a. coverslip rack.) Finally, during the rinsing of the films, solvents were permitted to completely dry before adding the next layer (DMSO required up to 90s to dry.)

4.2.3 ZnO sol gel

Zinc oxide layers were deposited in air following previously established protocols.[12,13,16] A 0.45 M (by zinc atomic concentration) was prepared by combining 363.7 mg (1.657 mmol) of zinc acetate dehydrate, 101.2 mg (1.657 mmol) ethanolamine, and 3.71 ml of 2-methoxyethanol in a glass vial. The solution was stirred at room temperature for 30 mins before using. 2-3 drops of this zinc acetate solution was deposited through a 0.2 µm PTFE syringe filter on the sintered CdTe film and rotated at 3000 rpm for 60 sec. The substrate was then annealed at 300°C for 2 mins.

4.2.4 Aluminum contacts

Aluminum contacts were deposited in a thermal evaporator housed within a nitrogen glovebox. Nearly complete solar cell devices were loaded onto a custom-made mask. The film located in the bus bar area was scratched with a diamond scribe in order for the evaporated aluminum to deposit on, and make contact with, the underlying ITO layer. Aluminum was deposited once the evaporator reached and initial pressure of $1x10^{-6}$ Torr, and during evaporation, rarely above $2x10^{-6}$ Torr. Evaporation occurred at rate of 3-5 Å/s to a thickness of 100 nm.

4.2.5 J-V and EQE measurements

J-V curves were measured within an argon glovebox using an old *Oriel* solar simulator that was certified AAA by *Newport* in May 2015. The light source was kept outside the glovebox requiring light to pass through a glass opening in the underside of the glovebox. External quantum efficiency was measured using custom set-up that also passed light through this opening. Custom *LabView* programs were used to measure and record data.

4.2.6 SEM

Scanning electron micrographs of sinter CdTe films were imaged using a *Zeiss Gemini Ultra-55* housed and maintained at the *Molecular Foundry* at *Lawrence Berkeley National Lab*. Typically, film micrographs were imaged at an accelerating voltage of 3-5 kV and working distance of 2.8-5 mm and an aperture of 30 mm.

4.3 Fabrication process

Solar cells are fabricated adopting an architecture commonly implanted in the organic photovoltaic community.[17] Indium tin oxide acts as the transparent conducting oxide (TCO) and hole collector, while a ZnO sol gel, paired with aluminum, conducts electrons, as seen in Figure 4.1. This device structure deviates from the conventional CdTe solar cell which is usually paired with CdS as the n-type layer.[2] Selected not for optimum performance, this architecture is easy to fabricate and therefore prove the performance of our sintered CdTe films. Devices implementing

this structure achieved over 12%, revealing that it has the potential to turn heads in the CdTe community.[13]

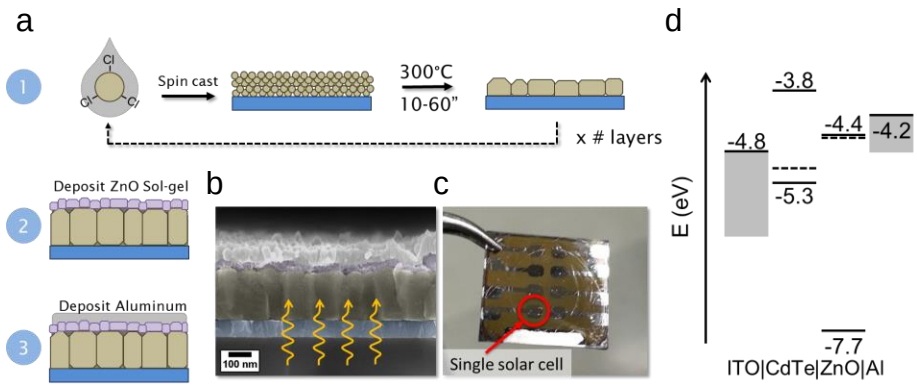

Figure 4.1. (a) Solar cell device fabrication scheme. (b) Cross sectional SEM image of device structure. (c) Photograph of substrate showing 8 individual cells and bus bar. (d) Band diagram of device.

Our devices were fabricated in a superstrate configuration illustrated in Figure 4.1a. First, a sintered CdTe NC film is deposited from implementing the layer-by-layer process discussed in Chapter 2. Next, a ZnO sol-gel is deposited from solution and formed upon heating. Finally, an aluminum contact is thermally evaporated. A SEM cross sectional image of a completed device is shown in Figure 4.1b, and a photograph of a substrate with eight individual solar cells is shown in Figure 4.1c. A band diagram of the device structure is illustrated in Figure 4.1d.

4.4 Initial solar cells: grain control and influence of air

Initial solar cells devices of this project lacked in performance but proved two major hypotheses. Solar cell fabrication and film quality were developed in parallel permitting hypothesis to be tested at a preliminary stage at the expense of impressive results (i.e. high PCE.) But this approach—building and testing cells and films—helped guide further film development as discussed in Chapter 3.

After establishing that [NC] controlled grain morphology, the first hypothesis naturally evolved: columnar grained films will yield better performing devices than grainy films. Traditionally, grain boundaries (GBs) are perceived as charge scattering zones in charge transport, and recombination centers for excited state carriers. In CdTe films exposed to chloride, these grain boundaries are converted into n-type electron highways. In either model, we hypothesizes that GBs parallel to the flow of charge will provide ideal charge transport compared to any non-parallel grain structure such as GBs oriented normal to the device structure. Even if the GB are chlorinated, their n-type nature will inhibit hole transfer when orthogonal to the current direction. Therefore, we hypothesize that the columnar grain structure obtained from low [NC] will outperform the porous, grainy structure obtained at high [NC]. Previous modelling efforts of the current flow with chloride-doped GBs parallel and perpendicular to the device stack has shown that performance always improves with grain size, even when columnar.[18] However, these report has a difference

size regime (1-10 microns) than our system (~100 nm.) Furthermore, it is hard to measure the electron transport—Cl GB concertation relationship weakening the strength of such model.

The second hypothesis is that sintering CdTe NCs in air will add a CdTe-oxide component to the films improving its charge transport and therefore performance. Previous sintered CdTe devices have been sintered only in air. Even though the vast body of CdTe literature shows that some amount of oxygen must be present to achieve good performance, this has not been proven in sintered NC cells. However, researchers have mentioned an optimal sintering time is required to optimize between grain growth and over-oxidation.[12] An optimal temperature was also reported in an different group.[13] Here we seek to observe to performance difference in solar cells that incorporate sintered CdTe NC films fabricated in an inert and air environment.

The influence of grain morphologies on cells performance was first tested. Two [NC] were selected to achieve the two difference grain structure regimes established in Chapter 3: 0.5 mM for a grainy texture, and 0.2 mM for the columnar structure. The number of layers was adjusted to achieve similar films thickness of around 700 nm. CdTe films were deposited layer-by-layer in an inert environment onto clean ITO substrates. Each layer was sintered at 350°C for 30 sec, then rinsed with hexanes (10 drops) and isopropanol (20 drops) before the next layer. A ZnO sol-gel was deposited on the CdTe film outside the glovebox and the device was completed by the thermal evaporation of aluminum.

The influence of sintering environment on device performance was tested by preparing the columnar grain-structured film in air using the exact same [NC] (0.2 mM) and number of layer (20). This device was fabricated on the same day suing the same ZnO sol-gel and aluminum contact to ensure a quality control sample.

Results support the two hypotheses that a (1) columnar structure dramatically improves solar cell performances compared to that of a grainy structure, and (2) a columnar film sintered in air adds an additional boost. SEM cross-sectional images in Figure 4.2a-c reveal that a grainy, porous structure was obtained at high NC concentration (Figure 4.2a), whereas a columnar structure was obtained in films fabricated with a lower [NC] (Figure 4.2b-c.) The film sintered in air appears to exhibit a similar "smoothing out" of the grain structure features compared to its counterpart sintered in an inert atmosphere (see similar results in Chapter 3.) The columnar structure achieves >10x improvement in the best performing device (see J-V curve, Figure 4.2d) and 12x improvement in efficiency on average (table in Figure 4.2d.) This result lends a strong support of the columnar over grainy structure. One of the most noticeable observation is the sharp decrease in series resistance from the grainy to columnar films. This supports the hypothesis that the presence of GBs nonparallel to the current direction scatters charges leading to high series resistance. Incorporating of a CdTe-oxide component into the films appears to improve both V_{oc} and J_{sc} leading to better performance. The physical reasoning of this result still needs to be investigated further. This grain structure appears to be also similar to the record sintered CdTe NC solar cell suggesting that we are on the right path.[13]

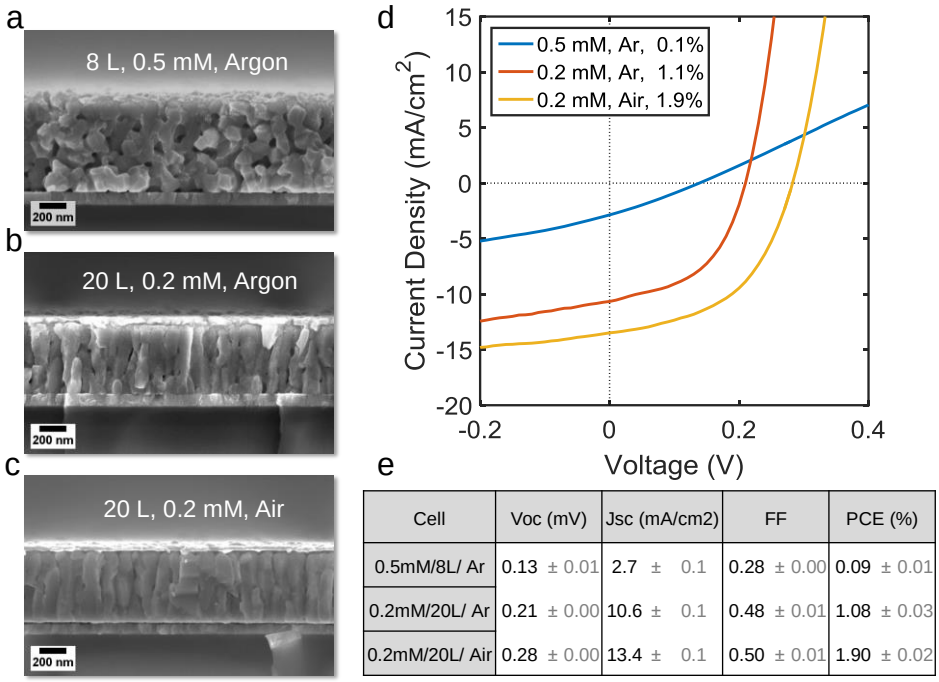

e

Cell	Voc (mV)	Jsc (mA/cm2)	FF	PCE (%)
0.5mM/8L/ Ar	0.13 ± 0.01	2.7 ± 0.1	0.28 ± 0.00	0.09 ± 0.01
0.2mM/20L/ Ar	0.21 ± 0.00	10.6 ± 0.1	0.48 ± 0.01	1.08 ± 0.03
0.2mM/20L/ Air	0.28 ± 0.00	13.4 ± 0.1	0.50 ± 0.01	1.90 ± 0.02

Figure 4.2. Initial solar cells showing grain structure-performance relationship. (a-c) Cross-sectional SEM images of cells fabricated with (a) 8L, 0.5 mM in argon, (b) 20L, 0.2 mM in argon, and (c) 20L, 0.2 mM in air. (d) J-V curves of best cells from devices fabricated in a-c. (e) Average J-V metrics for best 3 devices.

4.5 Optimizing temperature, [NC], and sintering time

After establishing the sheer importance of grain structure on the performance of solar cells incorporating sintered NC films, we optimized a few key parameters using a ~150 nm thick test device. Although lower [NC] yields dense, columnar films ideal for solar cells, the tradeoff is that more layers, and thus more time, is required to build up films thickness. In order to explore numerous parameters quickly while minimizing NC used per experiment, we identified ~150 nm as the minimal film thickness required to prevent shunting and establish diode J-V behavior. This selected thickness also corresponds to a local maximum in the theoretical J_{sc} vs. thickness relationship.[12] We will refer to this as the *test* device.

Three most salient parameters initially explored was sintering temperature, [NC], and sintering time. We knew from Chapter 3 that all three of these parameters determine films structure: temperature determines the meta-equilibrium grain size and growth rate, time dictates how close to the meta-equilibrium state, while [NC] controls grain morphology.

The highest performing test cells fabricated at these parameters was at a temperature of 300°C, [NC] of 0.15 mM, and a time of 20 sec. Average efficiency is plotted in Figure 4.3 and average J-V metrics are summarized in Table 4.1. The [NC] data is consistent with our preliminary results (Figure 4.2) where performance quickly drops off above 0.2 mM. We would expect that the performance to only improve with a decrease in [NC] as this would lead to denser, more continuous grains. However, we must keep in mind that lower [NC] require more layers, which means the underlying layers experience an longer integrated annealing time. There is some chance

that the performance starts to drop of below 0.15 mM due to the diffusion of indium from the ITO into the CdTe layer leading to n-type doping of CdTe and reduction of the ITO work function which manifest as lower V_{oc} and poor performance. This was observe in similar solar cells.[19] This interface appears to be crucial to the performance of these devices and one of the controlling aspects of the performance of these cells.

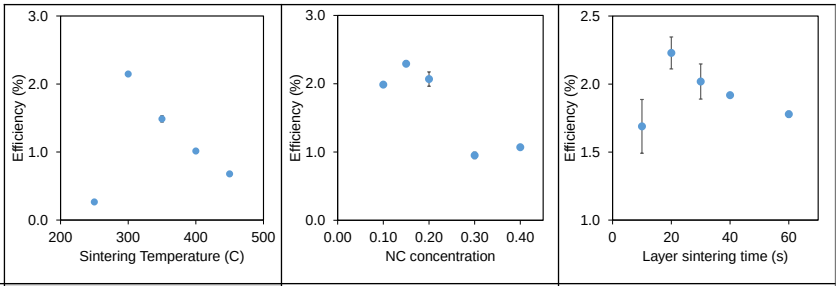

Temperature		300C	300C
[NC]	0.2 mM		0.15 mM
Time	60 sec	20 sec	

Figure 4.3. Optimizing ~150nm solar cell. Average cell efficiency based on 3 best devices for temperature (left), [NC] (center), and sintering time (right).

The low sintering temperature is surprising and inconsistent not only with previously reported results, but also with the TGA-DSC data obtained in Chapter 3. This observation may also be linked to the ITO-CdTe interface. The optimal conditions for devices sintered in air was 15-20 s and 350°C.[12,13] However, this optimal may be different for films sintered in an inert environment. One possible explanation: oxides, which have speculated to passivate GBs, do not form in an inert environment leading to a lower optimal temperature. According to the TGA-DSC data (Chapter 3), some portion of the ligand remains at 300°C and the sintering event doesn't occur until ~350-400°C. The temperature inconsistency may simply be due to an inaccurate measurement of the hotplate temperature. We have found that measuring hotplate surface temperature is a non-trivial endeavor as these instruments exhibit large non-homogeneities across the surface. We used a surface-specific probe from VWR to measure the temperature. Unfortunately, this device shows a large range of temperatures depending on the pressure exerted on the probe. However, the diffusion of indium from the ITO into the CdTe may be the thermally activated event determining cell performance. Cell performance dramatically drops off below 300°C. Between 250 and 300°C is assumed to be a critical temperature for activating significant grain growth required to facilitate charge transport.

Table 4.1. Average cell J-V metrics for three optimization parameters identified in Figure 4.3.

Temp (°C)	Voc (mV)	Jsc (mA/cm2)	FF	PCE (%)
250	0.23 ± 0.01	3.5 ± 0.0	0.33 ± 0.00	0.3 ± 0.0
300	0.32 ± 0.00	15.5 ± 0.7	0.43 ± 0.02	2.1 ± 0.0
350	0.26 ± 0.00	14.6 ± 0.4	0.39 ± 0.00	1.5 ± 0.0
400	0.26 ± 0.00	11.9 ± 0.3	0.33 ± 0.00	1.0 ± 0.0
450	0.26 ± 0.00	8.9 ± 0.2	0.29 ± 0.01	0.7 ± 0.0
[NC] (mM)				
0.1	0.28 ± 0.00	16.2 ± 0.6	0.44 ± 0.01	2.0 ± 0.0
0.15	0.33 ± 0.01	16.4 ± 0.4	0.43 ± 0.01	2.3 ± 0.0
0.2	0.36 ± 0.02	16.8 ± 0.2	0.34 ± 0.00	2.1 ± 0.1
0.3	0.26 ± 0.00	11.6 ± 0.3	0.31 ± 0.01	1.0 ± 0.0
0.4	0.32 ± 0.00	11.0 ± 0.2	0.30 ± 0.00	1.1 ± 0.0
Time (s)				
10	0.36 ± 0.03	15.5 ± 0.6	0.30 ± 0.00	1.7 ± 0.2
20	0.34 ± 0.00	16.4 ± 0.2	0.40 ± 0.02	2.2 ± 0.1
30	0.33 ± 0.01	15.3 ± 0.4	0.40 ± 0.01	2.0 ± 0.1
40	0.32 ± 0.00	14.2 ± 0.1	0.42 ± 0.00	1.9 ± 0.0
60	0.30 ± 0.00	14.5 ± 0.1	0.41 ± 0.00	1.8 ± 0.0

An optimum time of 20 sec was found for these test devices. Sinter time determines the integrated heating of the ITO-CdTe interface: longer times yield lower performance. The steady decrease in V_{oc} with layer sintering time is consistent with this hypothesis. However, below 20 sec, efficiency drops off due to an increase in series resistance in the devices. At times below 20 sec, continuous grains may not have the time to form producing a more grainy-like structure. Cross-sectional SEM could support this claim, but has not been obtained yet.

We understand that true optimization requires the entire grid to be explored as there variables often synergize. This interaction is obvious when combining our understanding of how time and temperature determine grain size in recrystallization and grain growth. Add [NC] into the mix and the combinatorics grows much larger. To explore the synergistic effects of these parameters, we chose to explore a small space of time and temperature while holding [NC] at 0.15 mM: 20 and 60 s and 300, 350, 400°C. Table 4.2 summarizes the average J-V metrics for the best 3 devices (by PCE). The best overall performing device appears at the minimum of the combined parameter space at 300°C and 20 sec, and the worst performing device exists at the extreme of the two parameter tests, 400°C and 60 sec. However, it is difficult to make a generalization on the main controlling parameter—temperature or time—by looking at the four device between these two extremes. This grid demonstrates that optimization is not easy and generating physical explanations for the results is even more difficult. Either way, the location of the best and worse device is consistent with the hypothesis that the indium diffusion into the CdTe controls the performance in the devices.

Table 4.2. Average cell J-V metrics for optimization time and temperature.

Time (s)	Temp (°C)	Voc (mV)	Jsc (mA/cm2)	FF	PCE (%)
20	300	0.32 ± 0.02	16.8 ± 0.4	0.30 ± 0.00	1.63 ± 0.11
20	350	0.21 ± 0.01	12.6 ± 0.1	0.30 ± 0.01	0.79 ± 0.06
20	400	0.21 ± 0.01	9.7 ± 0.4	0.27 ± 0.01	0.53 ± 0.04
60	300	0.29 ± 0.01	15.6 ± 0.1	0.34 ± 0.01	1.57 ± 0.01
60	350	0.24 ± 0.00	17.2 ± 0.9	0.36 ± 0.01	1.50 ± 0.05
60	400	0.22 ± 0.00	8.0 ± 0.3	0.25 ± 0.01	0.44 ± 0.03

4.6 Importance of glovebox oxygen partial pressure

Sintering atmosphere plays in important part in the performance of sintered solar cells as demonstrated in the initial solar cells in Section 4.4. Oxygen was identified as an important parameter in the composition of the sintering atmosphere in 4.4. We found that even minute amounts of oxygen influenced solar cell performance. This was discovered by comparing the control devices over time for each experiment during device optimization.

For numerous optimizations, a control device was fabricated to ensure that solar cell performance was a function of the test parameter such as temperature, [NC], or time and not changing with differences in other fabrication steps such as ZnO sol-gel or aluminum deposition. By tracking the oxygen ppm of the glovebox, we identified that performance was influenced by small changes in O_2 partial pressure. Control device fabrication parameters were 6 layers of 0.15 mM CdTe-Cl NCs sintered at 300°C for 60 sec. Figure 4.4 reports the trend of cell efficiency with glovebox O_2 partial pressure.

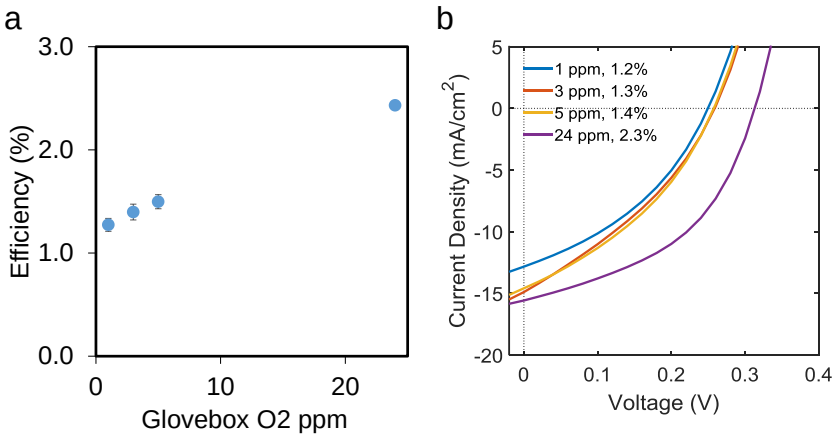

c

O2 ppm	Voc (mV)	Jsc (mA/cm2)	FF	PCE (%)
1	0.26 ± 0.00	13.1 ± 0.3	0.37 ± 0.01	1.27 ± 0.06
3	0.27 ± 0.01	14.8 ± 0.2	0.36 ± 0.01	1.40 ± 0.08
5	0.27 ± 0.01	13.4 ± 0.3	0.41 ± 0.00	1.50 ± 0.07
24	0.32 ± 0.00	16.9 ± 0.2	0.45 ± 0.01	2.43 ± 0.01

Figure 4.4. Influence of glovebox oxygen partial pressure on solar cell performance. (a) Average efficiencies vs. O_2 ppm. (b) J-V curves for best devices for each O_2 ppm. (c) Summary of average J-V metrics for best 3 devices.

Cell performance increases with increasing O_2 ppm. This result is consistent with previous findings that cell sintered in air yield better performance than those sintered in an inert atmosphere. Keep in mind that the cell reported here were sintered for 60 sec, which is much longer time than those sintered in air. While this is an important finding, it only expands the number of parameters needed to be explored—or controlled—to extract meaningful relationships between a selected parameters.

4.7 Solar cell performance based on films sintered in air

In this section we further explore the effect of sintering atmosphere on device performance. Preliminary results in Section 4.4 demonstrated that the presence of oxygen is crucial in obtaining the highest performance from a sintered NC solar cell. Here, we explore the air-sintered devices on our optimized 150 nm *test cells*.

By sintering CdTe films in air and varying temperature, we found that the best device at 300°C. Taking inspiration from previous reports[12,13,20,21], we sintered films for 20 sec at three temperatures, 300, 350, 400°C. Results can be found in Figure 4.5. Even though the films were sintered in air, the optimal temperature appears to be same as that for cells sintered in an inert atmosphere (comparatively, considering O_2 level in the glovebox was ~10ppm, many orders or magnitude lower than air.) Discovering the optimum temperature is consistent with the hypothesis that diffusion of indium into the CdTe film. This temperature is an optimum between growing large grains while minimizing indium diffusion.

a

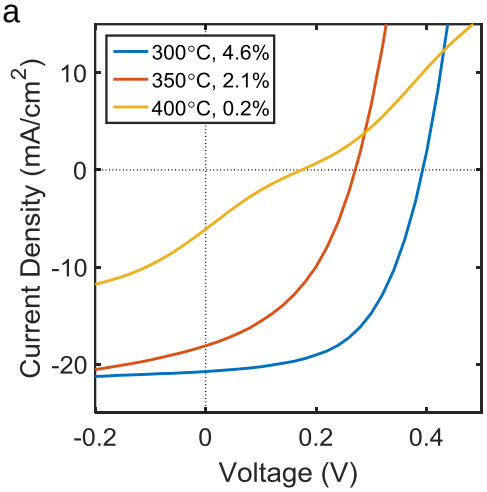

b

Temperature (°C)	Voc (mV)	Jsc (mA/cm2)	FF	PCE (%)
300	0.39 ± 0.01	20.4 ± 0.7	0.56 ± 0.01	4.52 ± 0.09
350	0.27 ± 0.01	18.0 ± 0.3	0.41 ± 0.01	2.03 ± 0.10
400	0.17 ± 0.01	6.2 ± 0.2	0.20 ± 0.00	0.21 ± 0.00

Figure 4.5. Temperature dependence of solar cells sintered in air. (a) J-V curves of best devices. (b) Summary of average J-V metrics from best 3 devices.

Devices sintered in air outperform those sintered in an inert environment as shown in Figure 4.6. Best performing the air-sintered device is nearly double that of devices sintered in nitrogen, and the average efficiency is more than double. This is consistent with the preliminary devices which demonstrated nearly double the efficiency by sintering in air. Sintering in air—which incorporates various oxides of cadmium and tellurium—appears to dramatically increase the V_{oc}. This boost is 100 mV on average. This increase in V_{oc} may be the result of many physical changes: passivating GBs, incorporation of a higher bandgap material (CdO E_g = 2.1 eV) [22], higher grain structure quality, or a combination.

a

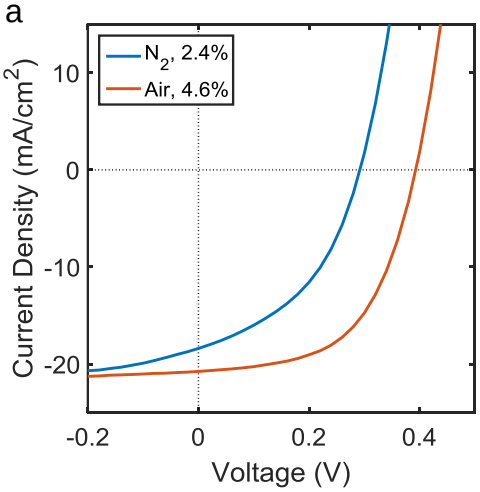

b

Fab. Atm.	Voc (mV)	Jsc (mA/cm2)	FF	PCE (%)
Air	0.29 ± 0.01	17.6 ± 0.6	0.42 ± 0.02	2.16 ± 0.19
N_2	0.39 ± 0.01	20.4 ± 0.7	0.56 ± 0.01	4.52 ± 0.09

Figure 4.6. Comparing performance of solar cells sintered in nitrogen and air. (a) J-V curves of best devices. (b) Summary of average J-V metrics from best 3 devices.

To date, the best solar cell achieve—evaluated by efficiency—was the 150 nm device sintered with [NC] = 0.15 mM at 350°C for 20 sec in air, as shown above.

4.8 MoO_x electron blocking layer and sintered solar cell performance

Low open circuit voltage plagues the baseline performance of these sintered CdTe-Cl NC solar cells. Implementing ITO as the hole-collector (anode) is one obvious weakness to the current device architecture. At ~-4.8 eV, the work function of ITO contacts the CdTe mid-gap. This reduces the chemical potential of the extracted holes and therefore V_{oc} *and* permits electron collection reducing photocurrent. We propose that these weaknesses can be mitigated by adding MoO_x to improve the electronic structure of the anode.[23] Like the device architecture, this strategy was borrowed from the organic PV community. Depositing MoO_x between ITO and CdTe layer improves V_{oc} two ways: (1) acts as an electron blocking layer at the hole-selective contact, and (2) provides a deep work function to collect holes from a deep valence band in the CdTe. In fact, making ohmic contact with CdTe's deep valence band has been a historical problem in the CdTe solar community.[2]

Figure 4.7a illustrates the band structure modified by MoOx (CdTe electronic affinity and band gap from Ref. 2.) The diagram reveals how the deep work function increases the chemical potential of the collected hole which contributes to a higher quasi-fermi level and therefore V_{oc}.

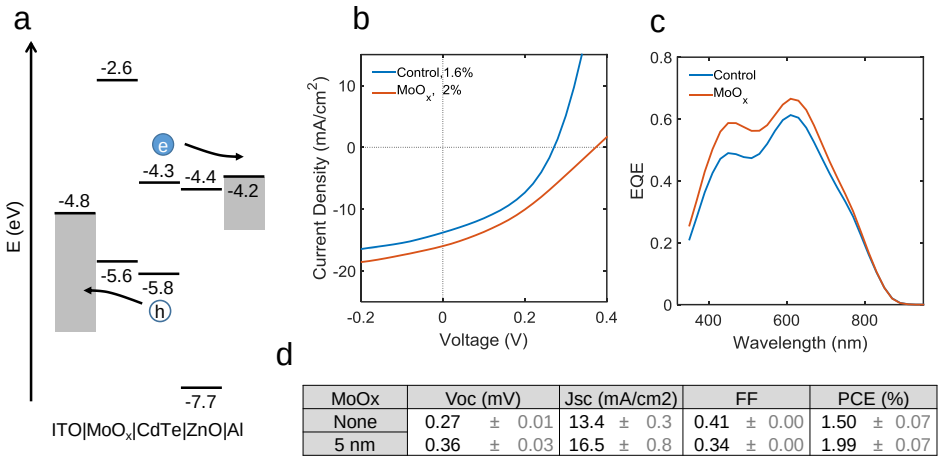

MoOx	Voc (mV)	Jsc (mA/cm2)	FF	PCE (%)
None	0.27 ± 0.01	13.4 ± 0.3	0.41 ± 0.00	1.50 ± 0.07
5 nm	0.36 ± 0.03	16.5 ± 0.8	0.34 ± 0.00	1.99 ± 0.07

Figure 4.7. Influence of a MoOx electron blocking layer on sintered solar cells. (a) Band diagram. (b) J-V curves of best devices. (c) EQE of best devices. (d) Summary of average J-V metrics from best 3 devices.

Solar cell efficiency improvement in our test-size 150 nm sintered CdTe-Cl NC cells was demonstrated. MoO_x (Mo(VI) oxide powder, *Sigma Aldrich*, used as received) was thermally evaporated onto a cleaned ITO substrate to a thickness of 5 nm, well above the minimal thickness to develop the famously deep work function.[24] Using the layer-by-layer method, approximately 150 nm of CdTe was deposited from 0.15 mM NC solution inside a nitrogen glovebox. Cell performance significantly improved compared to the control device fabricated on the same day with the same ZnO sol-gel and Al contact as shown in Figure 4.7b-d. Efficiency improved by 33% on average. V_{oc} is also increased by 33% or 90 mV. This was expected with a deeper hole-collecting work function (~-4.8 eV in ITO vs. ~5.6 eV in MoO_x). The increase in photocurrent is most likely a result of both the increase in V_{oc} and the blocking of electron current at the ITO. An increase in the EQE across all wavelengths is consistent with the improvements in J_{sc}. One tradeoff with adding the MoO_x is a reduction in fill factor, which is a result of a significant reduction in series resistance. This result validates that MoO_x or similar deep work function materials can be added to the ITO to boost V_{oc} and therefore performance in sintered CdTe-Cl solar cells.

4.9 Conclusion and Outlook

Thus far, we have found that the best cells are fabricated by sintering 0.15 mM NC solution in air at 300°C for 20 sec. This device is far from optimal but shows great promise as a result of the immense amount of control our CdTe-Cl building block affords. Oxygen appears to be a crucial aspect to these CdTe devices. Using air as an oxygen source may cause over-oxidation and limit the sintering time and temperature. Chloride composition can be controlled not only by the NC size, but also by the rinsing and sintering method. One major hurdle is overcoming thermal effects. In order to grow larger grains, we need to be able to sinter at higher temperatures. The ITO-CdTe interface maybe limiting this parameter due to indium diffusion. With higher thermal stability, FTO maybe a better transparent electrode for this system. Finally, at 150 nm, the test devices are far from an optimal thickness. Once an optimal device structure and fabrication conditions care identified, thicker films will greatly enhance performance.

4.10 References

(1) First Solar Achieves Efficiency, Durability Milestones http://investor.firstsolar.com/releasedetail.cfm?ReleaseID=895118 (accessed Oct 15, 2015).

(2) McCandless, B. E.; Sites, J. R. In *Handbook of Photovoltaic Science and Engineering*; Luque, Antonio, Hegedus, S., Ed.; John Wiley and Sons: West Sussex, United Kingdom, 2011; pp. 601–641.

(3) Kumar, S. G.; Rao, K. S. R. K. *Energy Environ. Sci.* **2014**, *7*, 45.

(4) Bonnet, D. *CdTe Thin-Film PV Modules*; Elsevier Ltd, 2012.

(5) Li, C.; Poplawsky, J.; Wu, Y.; Lupini, A. R.; Mouti, A.; Leonard, D. N.; Paudel, N.; Jones, K.; Yin, W.; Al-Jassim, M.; Yan, Y.; Pennycook, S. J. *Ultramicroscopy* **2013**, *134*, 113.

(6) Li, C.; Wu, Y.; Poplawsky, J.; Pennycook, T. J.; Paudel, N.; Yin, W.; Haigh, S. J.; Oxley, M. P.; Lupini, A. R.; Al-Jassim, M.; Pennycook, S. J.; Yan, Y. *Phys. Rev. Lett.* **2014**, *112*, 156103.

(7) Poplawsky, J. D.; Paudel, N. R.; Li, C.; Parish, C. M.; Leonard, D.; Yan, Y.; Pennycook, S. J. *Adv. Energy Mater.* **2014**, *4*, n/a.

(8) Visoly-Fisher, I.; Cohen, S. R.; Gartsman, K.; Ruzin, a.; Cahen, D. *Adv. Funct. Mater.* **2006**, *16*, 649.

(9) Visoly-Fisher, I.; Cohen, S. R.; Ruzin, A.; Cahen, D. *Adv. Mater.* **2004**, *16*, 879.

(10) Visoly-Fisher, I.; Cohen, S. R.; Cahen, D. *Appl. Phys. Lett.* **2003**, *82*, 556.

(11) Gur, I.; Fromer, N. A.; Geier, M. L.; Alivisatos, A. P. *Science (80-.).* **2005**, *310*, 462.

(12) Jasieniak, J.; MacDonald, B. I.; Watkins, S. E.; Mulvaney, P. *Nano Lett.* **2011**, *11*, 2856.

(13) Panthani, M. G.; Kurley, J. M.; Crisp, R. W.; Dietz, T. C.; Ezzyat, T.; Luther, J. M.; Talapin, D. V. *Nano Lett.* **2014**, *14*, 670.

(14) Olson, J. D.; Rodriguez, Y. W.; Yang, L. D.; Alers, G. B.; Carter, S. a. *Appl. Phys. Lett.* **2010**, *96*, 242103.

(15) Li, C.; Wu, Y.; Pennycook, T. J.; Lupini, A. R.; Leonard, D. N.; Yin, W.; Paudel, N.; Al-Jassim, M.; Yan, Y.; Pennycook, S. J. *Phys. Rev. Lett.* **2013**, *111*, 096403.

(16) Ohyama, M. *J. Am. Ceram. Soc.* **1998**, *32*, 1622.

(17) Yip, H.-L.; Jen, A. K.-Y. *Energy Environ. Sci.* **2012**, *5*, 5994.

(18) Troni, F.; Menozzi, R.; Colegrove, E.; Buurma, C. *J. Electron. Mater.* **2013**, *42*, 3175.

(19) Chambers, B. a.; Macdonald, B. I.; Ionescu, M.; Deslandes, A.; Quinton, J. S.; Jasieniak, J. J.; Andersson, G. G. *Sol. Energy Mater. Sol. Cells* **2014**, *125*, 164.

(20) MacDonald, B. I.; Martucci, A.; Rubanov, S.; Watkins, S. E.; Mulvaney, P.; Jasieniak, J. J. *ACS Nano* **2012**, *6*, 5995.

(21) Crisp, R. W.; Panthani, M. G.; Rance, W. L.; Duenow, J. N.; Parilla, P. a; Callahan, R.; Dabney, M. S.; Berry, J. J.; Talapin, D. V; Luther, J. M. *ACS Nano* **2014**, *8*, 9063.

(22) Babu, V. J.; Vempati, S.; Uyar, T.; Ramakrishna, S. *Phys. Chem. Chem. Phys.* **2015**, *17*, 2960.

(23) Sun, Y.; Seo, J. H.; Takacs, C. J.; Seifter, J.; Heeger, A. J. *Adv. Mater.* **2011**, *23*, 1679.

(24) Irfan, I.; Ding, H.; Gao, Y.; Small, C.; Kim, D. Y.; Subbiah, J.; So, F. *Appl. Phys. Lett.* **2010**, *96*, 243307.

5 Chapter 5: Sintered CdTe-Cl films for ultra-high gain photodetectors

Reproduced with permission from: Yingjie Zhang†, Daniel J. Hellebusch†, Noah D. Bronstein, Changhyun Ko, D. Frank Ogletree, Miquel Salmeron, A. Paul Alivisatos. Submitted for publication in *Nature Nanotechnology* on October 15, 2015. †These authors contributed equally to this work.

5.1 Introduction

Photodetectors, devices that convert photons to electricity, are widely used in digital imaging, optical communications, remote sensing, night-time surveillance, medical imaging, *etc.*[1-3] Their sensitivity, *i.e.*, the ability to differentiate signal from noise, is key for high-fidelity photon detection and imaging, especially when the signal is weak. In order to achieve superior sensitivity, a high gain is crucial to amplify the signal far above the noise baseline. One way to accomplish this is to multiply the photogenerated charge carriers in a single carrier transport and collection cycle, as done in photomultiplier and avalanche photodiode devices, which achieve typical gains of 10^3 – 10^8 carriers per incident photon.[4,5] However, the required high bias (100s to 1000s of volts) and their bulky nature restrict their integration with micro-electronics for digital imaging, and the electron multiplication processes give rise to excess noise. The other approach towards high gain is to collect each photocarrier multiple times over many transport cycles in simple, two-terminal devices with semiconductor channels.[3,6-8] These devices, known as photoconductors (a subset of photodetectors), are designed to trap the minority charge carriers for a long time, enabling majority carriers to recirculate through the device many times before recombining. In this way, multiple carrier collection occurs with the absorption of one photon. Small and simple in design, photoconductors are compatible with modern micro-electronics, and can be integrated as, for example, pixel sensors in the widely used CMOS (complementary metal–oxide–semiconductor) technologies.

The performance of a photoconductor device depends critically on the deliberate control of minority carrier trapping with the goal of achieving long carrier lifetime while preserving the high-mobility, low-noise majority carrier transport. Typically, minority carriers are retained in sub-bandgap states or electrostatic barriers induced by defects, dopants, electronic junctions, or a combination of these factors.[1,6-9] However, these minority carrier traps are often in the pathway of majority carrier transport. This leads to carrier scattering, reducing mobility, inducing transport noise, and therefore limiting the photon sensitivity.

5.2 Methods

5.2.1 Nanocrystal synthesis

CdTe nanocrystals (NCs) capped with cadmium oleate ($Cd(Oleate)_2$) with sizes of approximately 5 nm were synthesized by hot injection following a procedure modified from one previously reported.[28] Specifically, 4.8 g CdO, 42 g oleic acid, and 40 g octadecene were combined in a 500 ml three-neck round bottom flask. This mixture was degassed under vacuum at 100 °C for an hour. Meanwhile, two identical solutions of Te in tributylphosphine (TBP) were prepared: 1.5 g Te and

12 ml TBP were added to a 24 ml vial and heated to 220 °C until the powder dissolved and the solution became clear and yellow (~90 mins). Once a clear yellow solution was reached it was cooled to room temperature. After degassing the contents of the flask the head space was backfilled with argon and heated to 270 °C to form the cadmium oleate complex indicated by a color change from red to clear and colorless. Once the temperature stabilized at 270 °C, the flask was quickly removed from the heating mantle and the Te/TBP solutions were swiftly and simultaneously injected though 16 gauge needles into the hot solution. Upon injection the clear solution quickly changed to a dark color. The flask was quickly cooled to room temperature by spraying air and isopropanol from a wash bottle on the flask. After the solution cooled, the flask was connected to a distillation apparatus and the volatiles were vacuum distilled at 130 °C and 55 mtorr until ~40 ml of liquid remained. The crude product in the still pot was transfer via cannula to a Schlenk flask and stored in an argon-filled glovebox.

5.2.2 Nanocrystal purification

NCs were isolated and purified in an argon atmosphere. Approximately 10 ml of the crude product was added to a 50 ml centrifuge tube, filled with methyl acetate to ~40 ml total volume, and then centrifuged at 8000 rpm for 5 mins. The clear supernatant was disposed and the formed dark colored pellet with small amount of white content was dispersed in a small amount (~3-4 ml) of pentane. Methyl acetate was added to a total volume of 50 ml creating a turbid solution which was centrifuged at 8000 rpm for 5 mins. The nearly clear supernatant was disposed and the pellet was cleaned with 3 additional pentane/methyl acetate washing steps. By the last step, the pellet no longer contained a white residue. Finally, the pellet was dispersed in 20 ml of toluene and filtered into a clean glass vial with a 0.2 µm PTFE syringe filter. The solution was then dried under vacuum until all volatiles were removed. The dried residue was dispersed in toluene reaching a concentration of 1.5 mM determined from optical absorbance.[29]

5.2.3 Nanocrystal surface modifcation with chloride

CdTe NCs surface reaction was performed in an argon environment by adopting protocols established for CdSe-Cd(oleate)$_2$ NCs.[13,14] It is crucial to remove the residual water from all reagents and solvents using rigorous drying methods. To begin, 4 µmol CdTe-Cd(oleate)$_2$ NCs (2.7 ml of 1.5 mM NC solution) was added to a glass vial. TBP was added to the NC solution to a concentration of 500 mM. While the solution was stirred, 1.4 ml of trimethylsilychloride (TMSCl) was added (12 TMSCl molecules per nm^2 of NC surface). After the solution stirred for 1 hr, the volatiles were removed by vacuum distillation at room temperature (a small amount of liquid remained, presumably the TBP). After distilling for ~ 1 hr, 3 ml of toluene was added to the remaining product and the vial was shaken to facilitate uniform mixing and then centrifuged at 4000 rpm for 5 mins. The clear supernatant was disposed and 5 ml of toluene was added to pellet and stirred. 147 µL octylamine (3 molecules per nm^2 of NC surface) was added and the NCs immediately dispersed. After stirring for 1 hr, methyl acetate was added to flocculate the solution, which was then centrifuged at 4000 rpm for 5 mins. The supernatant was then disposed. The toluene/octylamine/methyl acetate step was repeated two more times. The final pellet was dispersed in ~5 ml toluene, filtered with a 0.2 µm PFTE syringe filter into a clean glass vial, and

then dried under vacuum for ~1 hr. The dark residue was dispersed in toluene to a desired NC concentration.

5.2.4 Film and device fabrication

Nanostructured CdTe polycrystalline films were formed by sintering spin coated CdTe NC solution in an inert environment. 300 nm SiO_2 / n++ Si or quartz substrates were cleaned by subsequent sonication in acetone and isopropanol, then dried with filtered nitrogen and finally exposed to oxygen plasma. A drop of CdTe NC in toluene solution (typically around 0.5 mM) was deposited on the substrate and spin coated at 1500 rpm. The substrate was then placed on a hotplate held at 350 °C for 30 s to 5 mins, yielding a polycrystalline film with thickness ~50–100 nm. In cases where thicker films was desired, the spin-coating and annealing procedures were repeated multiple times (layer-by-layer deposition). Thick films can also be fabricated using higher NC concentrations. Field effect transistor (FET) and photoconductor devices were fabricated by thermal evaporation (using shadow masks) of 60 nm indium and 40 nm gold on the CdTe polycrystalline film deposited on SiO_2/Si and quartz substrates, respectively. Channel length and width are determined by optical microscopy and/or atomic force microscopy on the final devices.

5.2.5 Local microscopy and spectroscopy characterization of the sintered film

CdTe films were prepared on n++ Si substrates (with native oxide) for local imaging and spectroscopy measurements.

Zeiss Gemini Ultra-55 scanning electron microscope (SEM) was used to image the top-view and cross-section morphology of the fabricated 1 layer and multiple layer films. Energy-dispersive X-ray spectroscopy (EDS) was performed during SEM imaging which also confirmed the existence of Cl in the CdTe film.

Nano-Auger electron spectroscopy was performed on 1 layer CdTe films using an Omicron system equipped with a field emission gun as an electron source. The vacuum level was 10^{-10} mbar, and the spatial resolution was ~10 nm limited by the diameter of the focused electron beam.

Conductive AFM (CAFM) and Kelvin probe force microscope (KPFM) was performed on 1 layer CdTe films using an Agilent AFM (with home-built feedback loop for the KPFM) in an inert atmosphere. Cr/Pt coated tips with a spring constant of ~0.2 N/m (from BudgetSensors) were used for CAFM, while Ti/Pt coated tips with a spring constant of ~2 N/m and a resonance frequency of ~70 kHz (from Olmpus) were used for KPFM. Surface potential was calibrated by setting that of the grounded Au film to -5.1 V (taking its work function to be 5.1 eV)[18]

5.2.6 Device measurements

All measurements were performed under inert atmosphere. DC I-V curves were measured using a Keithley 2636a dual source-meter. For photocurrent measurements, a xenon lamp combined with a monochromator was used to generate monochromatic visible/near-infrared light, which was collimated and directed towards the sample. Light intensity was controlled by neutral density filters and measured using a commercial Si photodiode (FDS1010 from Thorlabs). Photocurrent was determined from the DC current under illumination after subtracting the dark

DC current. Spectral responsivity measurements (Fig. 3b) were performed under a modulation of 75 Hz for different photon wavelengths.

Dark noise current (I_{noise}) was measured using an SR830 lock-in amplifier from Stanford Research Systems, following a previously reported procedure.[6] The measured I_{noise} is given in units of $A\sqrt{Hz}$. We calculated the noise equivalent power using the equation $NEP = I_{noise}\sqrt{B}/R$, where $B \approx 0.1\ Hz$ is the intrinsic bandwidth of the detector, and R is the responsivity.

To validate the accuracy of the NEP measurement technique, we performed the same measurement on the FDS1010 Si photodiode. From the measured dark noise current and the responsivity of the Si diode, we obtained a noise equivalent power similar with the specified NEP. Therefore we believe the measured noise current and NEP for the CdTe detectors are also accurate.

Transient photocurrent measurements (Fig. 4) were performed by generating light pulses from an LED (M660L3 from Thorlabs) using an Arduino electronics board, with the transient current measured by a digital oscilloscope (TDS 640 from Tektronix). Gate pulses were generated and synchronized with the light pulses using the Arduino board.

5.3 Results and discussion

5.3.1 Materials properties and device design

Here we present a novel strategy to engineer a heterogeneous system with unprecedented photo-sensitivity by sequestering the majority and minority carriers in different local domains using grain boundary delta doping (GBDD). We take advantage of the discovery by Cahen *et al.* that chloride doping at grain boundaries (GBs) in CdTe polycrystalline films establishes local p-n junctions that localize electrons in the GB regions, and direct holes towards the grain interiors (GIs).[10,11] We engineer the grain boundary doping, density and connectivity by exploiting the versatile surface chemistry of colloidal nanocrystals, and fabricate a photoactive film via kinetically controlled sintering of Cl-capped CdTe nanocrystals (Fig. 1a,b, Supplementary Fig. S1). In the last decade, there have been significant advances in surface modification of colloidal nanocrystals[12-14], and GBDD is a new concept that relies upon preparing nanocrystals surface modified with the eventual dopant atoms, in this case Cl. During the sintering of the nanocrystals, Cl selectively segregates to the grain boundaries, doping these regions n-type. The engineered GBDD establish built-in electric fields making the grain interiors (GIs) fully depleted (Fig. 1c.) These fields guide hole trapping in GIs and facilitate electron percolation along the GBs (Fig. 1d). Our film properties contrast with those of the traditional top-down deposited CdTe polycrystalline films, which have micron scale grains[10,11] significantly larger than those in our films (~50–200 nm.) The potential in these large grains is mostly flat with small band bending only near the GBs (~100 mV), due to the less effective Cl doping in GBs and the small depletion region width (~200 nm.) Although used for efficient solar cells, these films are not applicable for high-gain photoconductors since photocarriers in the flat band and low-barrier GB regions are subject to rapid recombination due to the overlap of the transport pathways of electrons and holes (holes can tunnel through GBs), yielding short carrier lifetimes (ns – μs).[15,16]

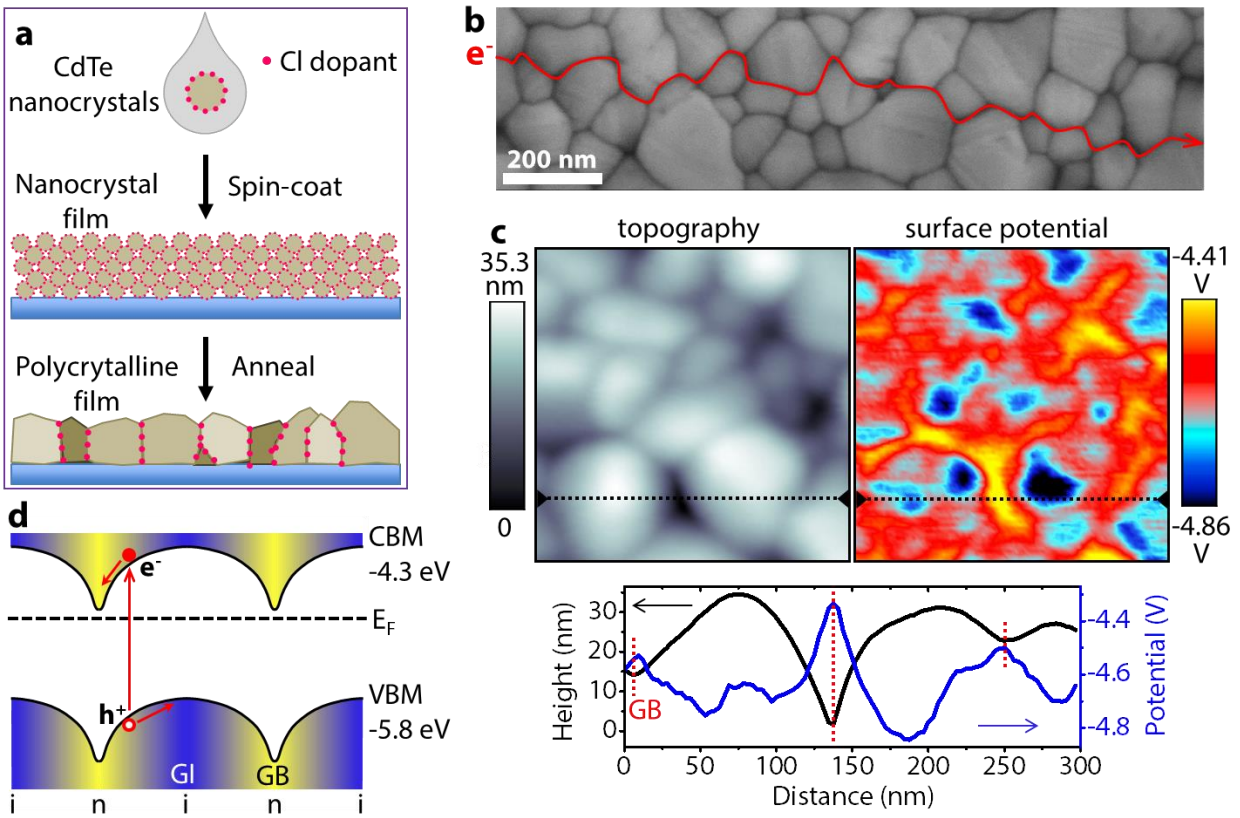

Figure 5.1. Material properties and device design. a, Schematic of the fabrication of a polycrystalline film from colloidal CdTe nanocrystals. Chloride-capped CdTe colloidal nanocrystals were spin coated onto a substrate forming a film, which was subsequently annealed at 350 ℃ in an argon environment for 0.5–5 min. b, Scanning electron microscopy (SEM) image of the polycrystalline film. Red line and arrow represents a pathway along GBs for electron percolation. c, KPFM topography and surface potential image obtained simultaneously on one area and representative line profiles. d, Schematic of the band diagram in real space, illustrating how the photoexcited electrons slide down to the GBs while holes move towards grain interiors (GIs). n: n-type; i: intrinsic.

Our bottom-up fabricated device has several advantages compared to previous high-gain detectors: (i) long carrier lifetime up to ~10 s, due to the long spatial separation between electrons and holes (10s of nm) and the large electrostatic potential barriers (100s of mV) between them; (ii) low-noise electron transport with high mobility, achieved by GBDD and trap-passivation in the GBs; (iii) tunable response time since the electrostatic barrier can be overcome by pulsed injection of electrons leading to rapid recombination; (iv) low-cost solution-processable and scalable fabrication process, where the thickness of the film can be tuned by changing the concentration of the nanocrystal solutions and/or by repeating the spin-coating and annealing procedures multiple times.

The spatial heterogeneity in doping, electrostatic potential and electronic transport – critical to the designed photodetector – are characterized by local microscopy and spectroscopy techniques. Nano-Auger spectroscopy confirmed that Cl is concentrated in the GBs of the sintered polycrystalline film (Supplementary Fig. S2.) Local potential variations are resolved by Kelvin

probe force microscopy (KPFM)[17,18], confirming that the GIs are fully depleted. We found that the Fermi level of GBs and GIs are ~-4.4 – -4.5 eV and ~-4.8 – -4.9 eV (relative to vacuum level), respectively (Fig. 1c and Supplementary Fig. S3), although these are average values over the ~20 nm spatial resolution of the KPFM. Since the conduction band minimum (CBM) and valence band maximum (VBM) are at ~-4.3 eV and ~-5.8 eV respectively (relative to vacuum level),[19] we conclude that the GBs are heavily n-doped while the GIs are weakly n-doped or nearly intrinsic. Spatial current mapping using conductive atomic force microscopy (CAFM) revealed a higher conductivity in GBs compared to GIs (Supplementary Fig. S4), as expected from the higher carrier concentration and trap passivation in the GBs. Note that a previous work showed the process of sintering Cl-capped CdSe nanocrystals into a high mobility film, but neither the spatial distribution of Cl nor its role in doping was identified or discussed.[14]

5.3.2 Electronic transport

Field effect transistor (FET) measurements under dark conditions confirmed n-type electronic transport (Fig. 2.) Since the GBs form a network with a large electrostatic electron confinement energy (~0.4 eV with no or small gate bias) and a higher conductivity than the GIs, we expect the GBs to be the dominant electron transport pathways. From the gate bias-dependent current, we obtain a spatially averaged field-effect mobility of μ_{FET}~5.2±2.3 cm^2/(Vs) and a conductivity of σ~10^{-4} – 5×10^{-3} S/cm at V_G = 0 V from devices made from several batches of CdTe nanocrystals, with the best μ_{FET}~10 cm^2/(Vs). The actual mobility and conductivity of the GBs can be much larger since most of the volume of the material is occupied by the GIs which are inactive for transport in the dark. Quantitative carrier concentration analysis from the KPFM and FET results further confirms that electron transport occurs mainly through GB regions (see the Supplementary Information.)

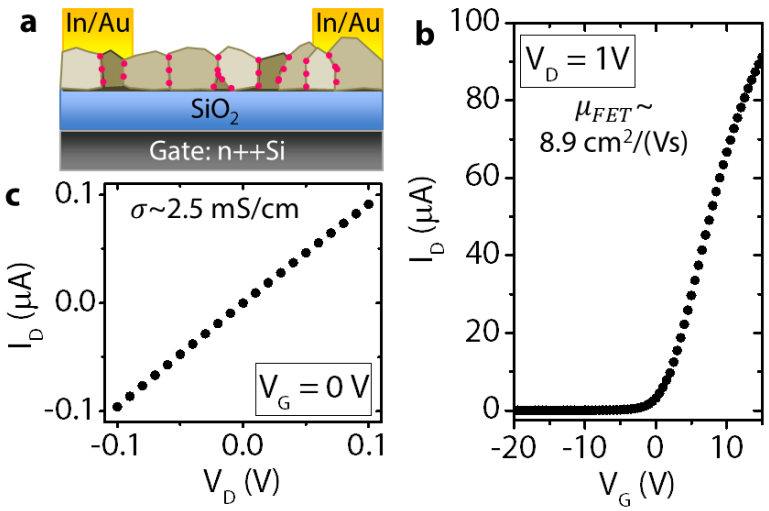

Figure 5.2. Electronic transport. a, Schematic of FET structure. b, Drain current (I_D) – gate bias (V_G) curve, with a fixed drain bias V_D = 1 V. Mobility is calculated from the slope of the curve at V_G > 0. c, I_D – V_D curve at V_G = 0 V, where conductivity is obtained as the slope of the curve. FET channel width: 3 mm; length: 40 μm; thickness: 50 nm. SiO_2 thickness: 300 nm. Measurements were performed in the dark.

5.3.3 Photoconduction

To explore the photosensitivity of the material, we fabricated photoconductor devices based on 300–400 nm thick CdTe films (Fig. 3a, inset.) Figure 3 reports the performance of two representative devices with channel widths of 2 mm and 80 μm and the same length of ~5 μm. Photocurrent was generated by shining collimated, monochromatic light onto the entire channel region of the device. Our devices have a large dynamic range, sensitive to light intensities varying over 8 orders of magnitude (Fig. 3a, Supplementary Fig. S5.) The photoconductive gain and responsivity (photocurrent divided by incident photon power) increases with the decrease of photon power, a typical behavior for high-gain photoconductors due to the dispersion in the activation energies of the carrier trapping sites.[8,9] Our devices show an external photoconductive gain of $G_{ext} \approx 8 \times 10^9$ and a responsivity of $R \approx 3 \times 10^9\, A/W$ at a power of $5 \times 10^{-9}\, mW/cm^{-2}$ for a wavelength of 500 nm. Both values are independent of the channel width and are the highest among all the visible and infrared photoconductors known in literature. We found that the film absorbs ~65% of the incoming light, and thus the internal gain (the number of collected carriers per absorbed photon) is of the order of 10^{10}. The internal gain can be approximated as $G_{int} = \tau_{lifetime}/\tau_{transit}$, where $\tau_{lifetime}$ is the minority carrier lifetime, while $\tau_{transit}$ is the transit time of the majority carrier (time to move form source to drain.) Therefore, we expect the gain to increase with decreasing channel length up until the grain size limit.

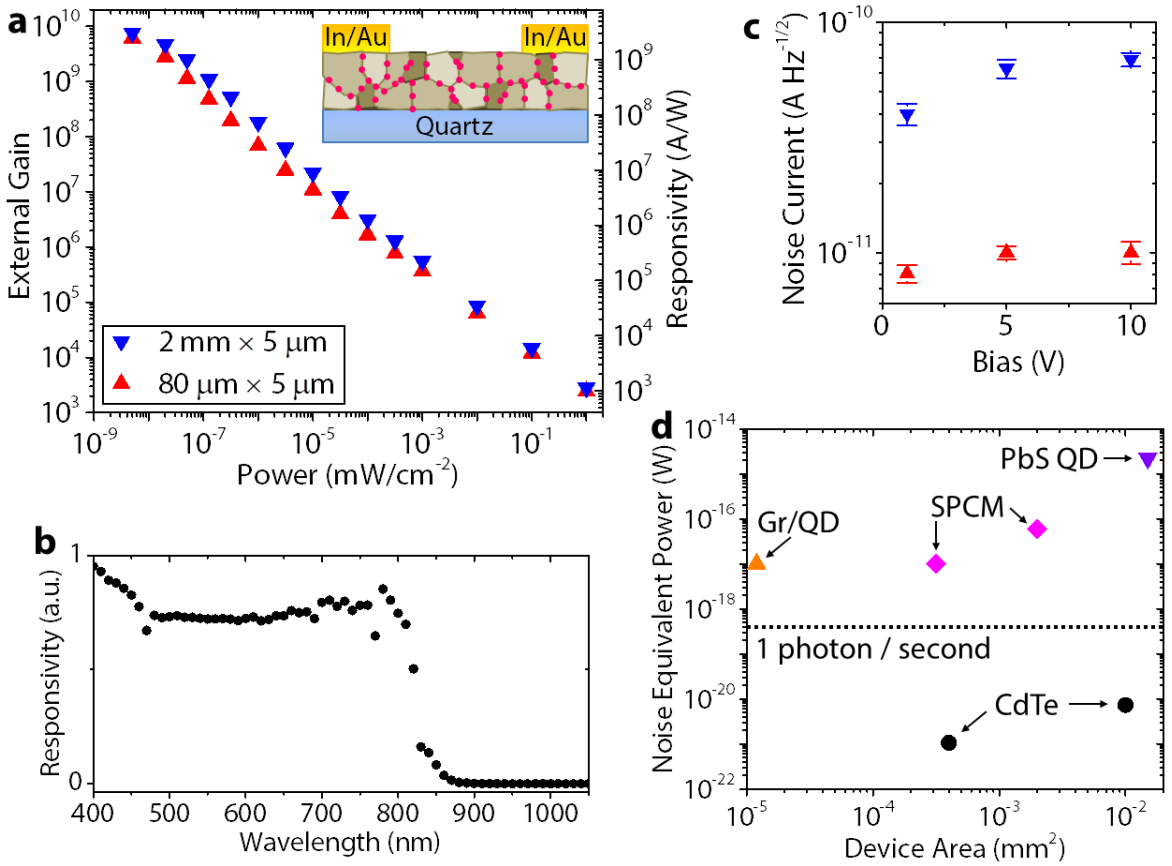

Figure 5.3. Photoconduction. a, External photoconductive gain and responsivity of two representative photoconductor devices, measured with 500 nm monochromic light. Inset: schematic of the device structure. Channel thickness: 320 nm; length: 5 μm; width: 2 mm and 80 μm, as noted. Bias: 10 V (photocurrent is nearly constant over the bias range 4–15 V, Supplementary Fig. S5). b, Spectral response of the device with 2 mm channel width. c, Noise current under dark condition of the two devices under different bias. Each error bar represents the standard deviation of several measurements. d, Noise equivalent power (NEP) of our two CdTe devices and other high-sensitivity devices. The values of CdTe detectors correspond to the case of 10 V bias (nearly the same for 4–15 V). Gr/QD: graphene-quantum dot hybrid[8], SPCM: single photon counting module (the most sensitive class of detectors based on inorganic crystalline semiconductors, where the NEP is calculated from the dark count rates of 25 and 150 counts per second, respectively)[20], PbS QD: PbS quantum dot (NEP calculated from the D^* value obtained at 10 Hz modulation frequency in Ref. 6).

These photodetectors are responsive to photons with wavelength smaller than ~850 nm, the bandgap of bulk CdTe (Fig. 3b), covering the entire visible and a small part of near-infrared spectrum. The responsivity is nearly constant over the range of 400–800 nm, which makes them highly valuable for visible camera applications.

To determine the sensitivity of the device, we measured the dark noise current and calculated the noise equivalent power (NEP), which represents the minimum detectable power at which the signal-to-noise ratio is unity (Fig. 3c,d) (see Methods.) We found that the NEP is $7.3 \times 10^{-21}\ W$ and $1.1 \times 10^{-21}\ W$ for the devices with 2 mm and 80 μm channel width, respectively, corresponding to 1 photon per ~55 seconds and 1 photon per ~360 seconds. We expect even lower NEP with smaller device area. This is an extremely high sensitivity compared to other high-performance detectors, such as PbS quantum dot photodetectors[6], graphene-quantum dot hybrid

photodetectors[8], and commercial single photon counting modules (SPCM) made from Si avalanche photodiodes (Fig. 3d).[20] In cases where the photon flux is smaller than 1 photon per second, device operation speed is not a limiting factor and our detector has significant advantage over others in accurate photon sensing.

The ultralow noise level can be attributed to the unique electronic properties of GBs and the percolation transport mechanism. It has been shown that Cl in the GBs of CdTe pushes the sub-bandgap defect states towards the VBM while moving the Fermi level close to the CBM.[21] Since the GBs in our device are heavily doped with Cl, we expect the sub-bandgap states to be filled lying far below the Fermi level and thus do not contribute to carrier trapping and scattering. This leads to a strong suppression of the trapping-detrapping (or generation-recombination) noise that typically dominates disordered semiconductors.[6,22,23] Therefore in our films the GBs provide smooth, uniform n-type pathways for electron transport. This is in sharp contrast with traditional polycrystalline films where the majority carriers are generated and transported through GI regions and are scattered at GBs which possess different chemical potentials than the GIs.[10,11]

5.3.4 Temporal response

Besides the gain and noise level, a photodetector's temporal response also determines the extent of its applications. As previously explained, high gain in photoconductors requires long carrier lifetime, and as a result these detectors typically have slow response, in the scale of 10^{-2} – 10^4 seconds.[8,9] Figure 4a shows the time-resolved photocurrents of our photoconductor under two different light intensities. At high intensity, the photocurrent decay consists of two components: a fast decay of ~1 ms, and a slow decay of ~10 s. At lower intensity, the slow component dominates. The rise time for both power levels is in the scale of 1 ms. We can estimate that at low light $\tau_{lifetime} \approx 10\,s$. Taking $G_{int} \approx 10^{10}$, we calculated $\tau_{transit} \approx 1\,ns$, which corresponds to a mobility of ~60 $cm^2/(Vs)$ (see the Supplementary Information.) This mobility is an order of magnitude higher than the measured bulk FET mobility, likely due to the volume averaging effect of the latter value, as mentioned above. Therefore, we expect that the actual mobility in the GBs to be in the scale of several 10s of $cm^2/(Vs)$.

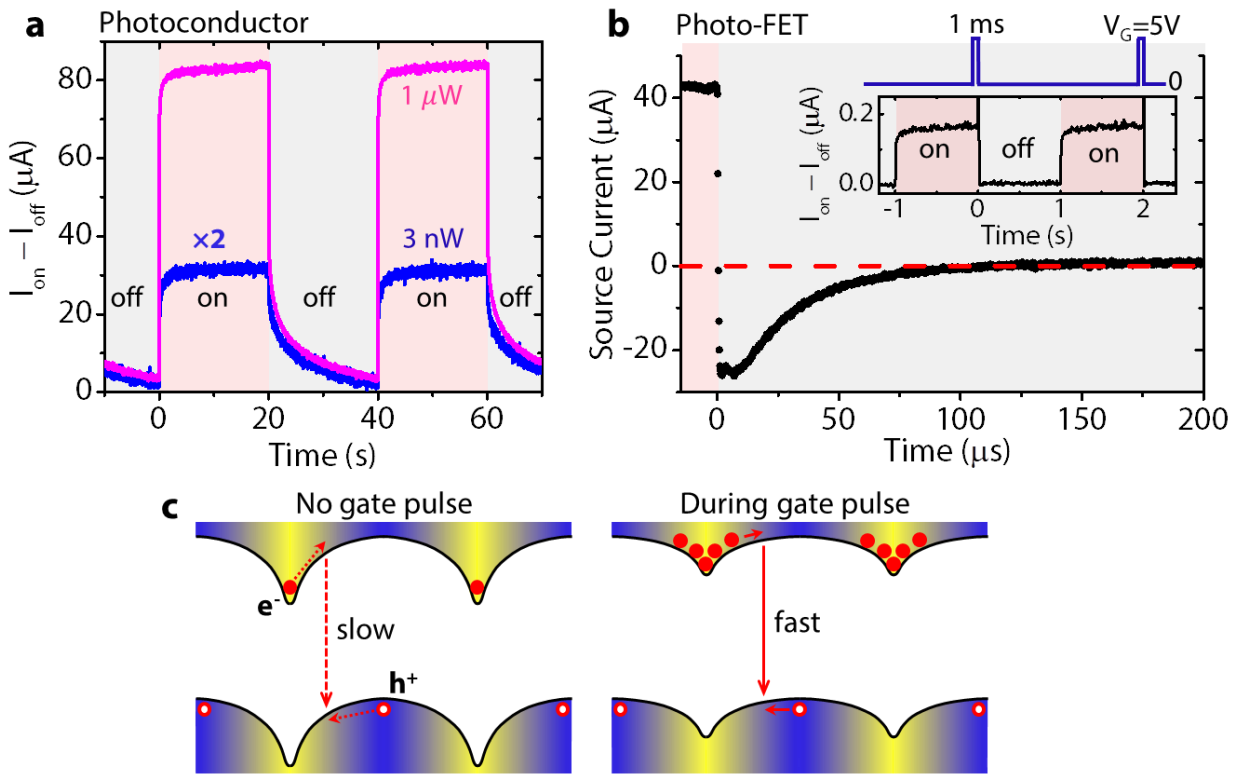

Figure 5.4. Temporal response. a, Time trace of the photocurrent in a photoconductor, with the on/off modulation of 660 nm light with two different intensities, 1 μW and 3 nW (over the channel region). Note that the photocurrent at 3 nW light was amplified by a factor of two for better comparison with the other one. Channel geometry: 2 mm (width) × 5 μm (length) × 320 nm (thickness). Bias: 1 V. b, Transient photocurrent in a photo-FET, in the presence of a 1 ms gate pulse synchronized with the on-to-off switch of the 660 nm light at 0.4 μW. Both the short-time current response (<200 μs) and long-time modulated current (figure inset) are shown. Channel geometry: 3 mm (width) × 40 μm (length) × 70 nm (thickness). V_D = 1 V. c, Schematic of the band bending and carrier recombination with or without the gate pulse reset.

One strategy to improve the device response speed in high-gain detectors is to apply a gate voltage pulse.[8,24] Reset or quenching circuits are also widely used in photomultipliers and avalanche photodiodes.[20] Since the hole traps in our device are electrostatic in nature, we expected that a positive gate pulse would flood the channel with electrons causing partial band flattening between the GIs and GBs, which reduces the electrostatic barrier yielding efficient electron-hole recombination (see the Supplementary Information). We employed this mechanism in a photo-FET (the same device structure as shown in Fig. 2a) and implemented a reset protocol: a 5 V gate pulse applied for 1 ms (Fig. 4b.) The source current rapidly decreased and changed sign within 1 μs (switch time of the light), and gradually returned to the original dark current value within ~100 μs. This sign switch, not reported before, reveals that the source-drain transport current (electrons injected from the source to the channel and collected by the drain) decayed within 1 μs after the gate was switched off, and the injected electrons left the channel via the source and drain electrodes within ~100 μs. Therefore, when the gate pulse was applied, the photocurrent decay mechanism changed from slow hole decay to fast electron decay, increasing the speed by five orders of magnitude. The absence of the sluggish minority carrier decay current confirms our proposed

mechanism of electron-hole recombination upon application of the gate pulse and is consistent with the proposed electrostatic trapping scheme (Fig. 4c). Note that this strategy is not as efficient in photoconductor devices that employ (or partially employ) sub-bandgap trap states which require higher pulse voltages to obtain only a modest improvement in response speed.[8,9]

Specific detectivity $D^{\star}$ is a standard measure of the detector sensitivity that represents the intrinsic materials properties, independent of the device geometry.[1,2] We can calculate the specific detectivity $D^{\star} = \sqrt{AB}/NEP$ from the measured NEP, intrinsic bandwidth ($B \approx 0.1\ Hz$, inverse of $\tau_{lifetime}$), and the device area A. In our devices $D^{\star}$~5×10^{17} Jones ($cm\sqrt{Hz}/W$), the highest reported for all the visible and infrared photodetectors operating at room temperature. In comparison, the specific detectivity of single-crystal silicon photodiodes is ~1×10^{13} Jones[25], and that of the graphene-quantum dot hybrid photodetector (one of the most sensitive photoconductor devices) is 7×10^{13} Jones.[8]

5.4 Conclusion

This solution-processed, scalable detector with remarkable sensitivity and rapid response enabled by GBDD is compatible with both video-rate pixelated imaging and large-area photon detection, and should excel in applications where the detection of low levels of photons is demanded (see the Supplementary Information.) There are many situations where the photon source is naturally weak. For example, at night time the trace amounts of light from moon, star, or other celestial objects can be close to or lower than 1 photon per second. Our detector, with extremely low NEP, may have advantage in this case for color night vision.[26] There are other situations where reducing the photon exposure is highly desirable, for example in medical X-ray detectors where X-ray generates electron-hole pairs in semiconductors and create electrical signals.[27] The much higher detectivity in our polycrystalline CdTe device compared to single-crystalline counterparts could enable significant reduction of X-ray dosage, promising for reducing negative radiation effects on the human body during the X-ray imaging process.

5.5 Acknowledgements

The authors thank Peter Denes and Jianbo Gao for discussion on photodetectors. Device fabrication and measurement was supported by the "Self-Assembly of Organic/Inorganic Nanocomposite Materials" program, Office of Science, the Office of Basic Energy Sciences (BES), Materials Sciences and Engineering (MSE) Division of the U.S. Department of Energy (DOE) under Contract No. DE-AC02-05CH11231 (Y.Z., N.D.B. and M.S.). Nanocrystal synthesis and thin film preparation was supported by the "Physical Chemistry of Inorganic Nanostructures" program by the Director, Office of Science, Office of Basic Energy Sciences, of the United States Department of Energy under Contract DE-AC02-05CH11232 (D.J.H and A.P.A). It used resources of the Molecular Foundry, supported by the Office of Science of the U.S. Department of Energy.

5.6 Supporting Information

5.6.1 Supplementary Text

Carrier concentration analysis

Carrier concentration can be calculated and compared from the KPFM and FET transport results. From KPFM results, we found that the Fermi levels (E_F) at GBs and GIs are ~0.1 – 0.2 eV and ~0.5 – 0.6 eV below the CBM (E_c), respectively. Taking the conduction band effective density of states (DOS) to be $n_c = 8 \times 10^{17}$ cm^{-3},[19] we can calculate the electron carrier density at the GBs and GIs from $n = n_c \exp(-\frac{E_c - E_F}{kT})$.[30] This gives electron carrier concentration in the range of $10^{14} - 10^{17}$ cm^{-3} and $10^{7} - 10^{10}$ cm^{-3} for GBs and GIs, respectively.

From FET transport results, we can determine the carrier concentration from $n = \frac{\sigma}{e\mu_{FET}}$ (e is the absolute value of the elementary charge). Although the conductivity and mobility calculations are subject to volume averaging effects due to the nature of the percolation transport, we expect the calculated carrier concentration to be a good estimate of the carrier density in the conduction pathways since the volume factors from σ and μ_{FET} cancel out. In this way we obtain $n \sim 10^{14} - 5\times10^{15}\ cm^{-3}$. The carrier density estimated from the FET results agree well with that of the grain boundaries estimated from KPFM results, which is an evidence that electrons concentrate in and conduct through the GBs.

Mobility calculation from transit time

While from FET data we can only obtain spatially averaged mobility, using transit time we can extract the actual mobility of the electron conduction pathways. The mobility by definition is $\mu = v/E$, where v is the (unsaturated) drift velocity and E is the electric field. The velocity can be calculated from the transit time as $v = L/\tau_{transit}$, where L=5 μm is the channel length. At the threshold voltage for velocity saturation $V_{Bias} = 4$ V (see Fig. S5), the transit time can be extracted from the internal gain as $\tau_{transit}$ = 1 ns (see main text), while the electric field can be calculated as $E = V_{bias}/L$. Therefore we have $\mu = L^2/(V_{bias} \cdot \tau_{transit})$ = 62.5 cm^2/(Vs).

Calculation of gate bias induced electrostatic barrier reduction

Here we present a simple model to calculate the decrease of the electrostatic trapping barrier in the GIs induced by the application of a gate bias V_G=5 V. Given that the capacitance per unit area of the 300 nm thick SiO_2 is C_{ox}=1.15×10^{-8} F/cm^2, we can obtain the injected carrier density (per unit area) $\sigma = C_{ox}V_G/e$=3.6×10^{11} cm^{-2}. Using an average grain size of d≈100 nm, we obtain an average number of electrons per grain $n_{Gr} = \sigma d^2 \approx 36$. Assuming that all the electrons are located at the GB regions, and considering that each GB is surrounded by two grains, each hole in the center of the grain interacts with $2n_{Gr}$=72 electrons in the nearest GBs that are r≈50 nm away. Therefore the Coulomb interaction energy is $E_{Coulomb} = 2n_{Gr}\frac{1}{4\pi\epsilon_0\epsilon}\frac{e^2}{r}$ ≈190 meV. Here ϵ_0 is the vacuum permittivity and ϵ=11 is the dielectric constant of CdTe.[31] This estimated Coulomb energy between the holes in GI centers and nearby electrons in GBs (induced by the 5 V gate bias) is about half of the original band bending between the GI and GB. We thus expect the gate induced electron flooding in the channel to cause significant band flattening. Note that this simple calculation assumes that electrons are all localized in GBs, which is not strictly valid since the injected electrons in GBs will repel each other and diffuse towards the GI regions. This spreading out of

the electrons is also responsible for rapid electron-hole recombination. The exact value of the barrier reduction and carrier distribution is beyond the scope of this discussion.

Examples of potential applications

(1) Visible camera applications. Our CdTe detector, compatible with CCD and CMOS technologies, has a high signal-to-noise ratio and a good response speed (1 ms with gate pulse reset) capable of video-rate imaging. Therefore it has great potential for pixelated imaging in visible cameras. In the currently dominated digital camera technology, the active pixel layer is made of single crystal silicon with a thickness of a few microns. In our CdTe detector we found that a ~300 nm thick film is capable of absorbing around two thirds of the visible light. Therefore our CdTe polycrystalline layer can potentially replace Si as the pixel layer, with the advantage that the smaller thickness will reduce pixel crosstalk. The low-cost solution processing and the ease of integration with the CCD and CMOS integrated circuits are appealing for this application.

(2) Night-vision cameras. Currently there are two types of commercial night-vision cameras: thermal imaging and image intensifier. A thermal imaging camera detects infrared light emitted by objects, and a contrast is formed if an object has a different temperature from its surroundings. This is effective in identifying warm objects in cool environments when little or no visible light is present. However, these cameras cannot directly resolve the color of the objects, losing an important feature for object identification. Moreover, objects with similar temperature cannot be distinguished. An image intensifier camera multiplies the light emitted by faint objects but requires high power, and has limited light amplification and signal-to-noise ratio. Our CdTe detector, with unprecedented sensitivity, should be capable of resolving objects under extremely low light conditions, such as the light from the moon and stars. The visible light can thus be detected to obtain images with true color. In the range of 700 – 850 nm, we can also detect a small part of the near-infrared light that provides an additional imaging channel.

A comparison of the night time illuminance level with the NEP of our photodetector reveals the advantage of the detector in night vision. The total starlight at overcast night can be as low as $3 \times 10^{-5} - 1 \times 10^{-4}\ lux$, corresponding to a photon intensity of $4 \times 10^{-12} - 1.5 \times 10^{-11}\ W/cm^2$ at a wavelength of 555 nm.[32] Using a camera where each pixel has an area of $2 \times 2\ \mu m^2$, the equivalent photon flux that needs to be detected per pixel is $2 \times 10^{-19} - 6 \times 10^{-19}\ W$ (~1 photon per second). As we can see from Fig. 3d, our CdTe photodetector has significant advantage over other detectors in detecting this low level of light.

(3) X-ray and Gamma ray detectors. Single crystal CdTe diodes have already been used as commercial detectors at these very short wavelengths, since CdTe has high stopping powers for X-ray and Gamma rays.[33] To detect these high energy photons a thick device (~1 mm) is required. Our polycrystalline CdTe film can be scaled to this thickness by, for example, spray coating of nanocrystals before sintering. The high sensitivity of the detector would make it possible to image low levels of X-ray, which is important for medical applications where low X-ray dosage is desired.

(4) Cherenkov particle detection. Cherenkov radiation is an important feature revealing the speed of charged high-energy particles.[34] From the radiation position and angle the speed and nature of the particle could be tracked down. Currently Cherenkov detectors used in particle detection experiments are in the form of photomultiplier tubes (PMTs), which are expensive and demand a huge amount of power to operate, especially since thousands of the meter-sized PMTs are needed to detect trace amounts of particles. Since our detector has the highest detectivity to date and can be scaled to very large sizes due to the solution processability, we expect it to have potential impacts in the area of particle detection.

5.6.2 Supplementary figures

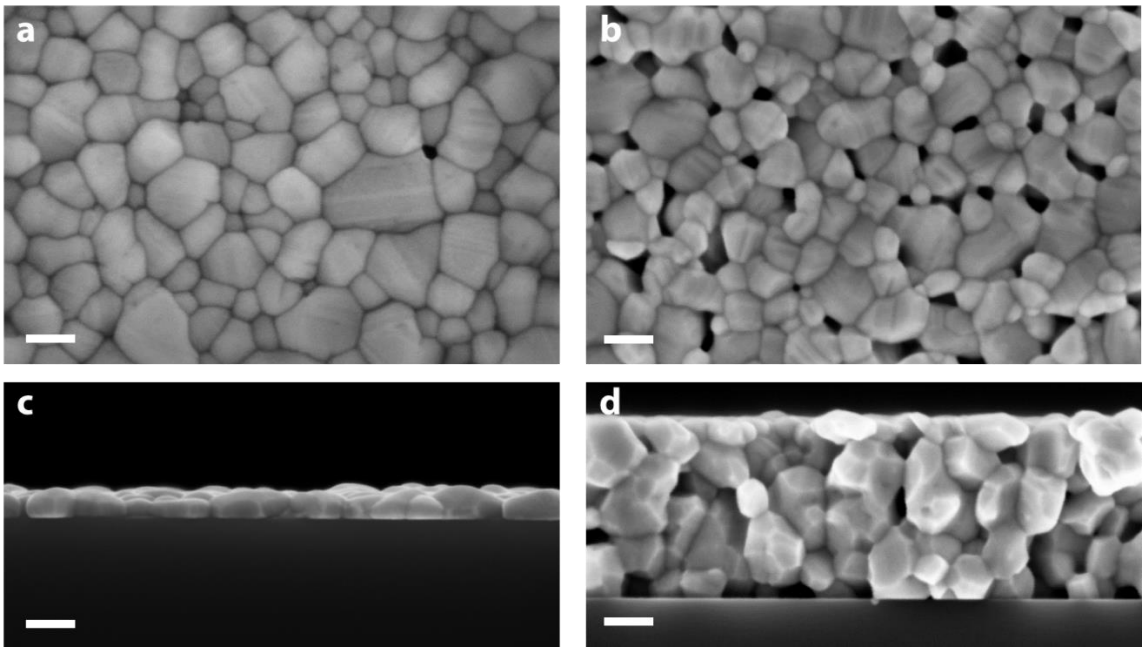

Fig. S1. Scanning electron microscopy (SEM) images of the sintered CdTe polycrystalline film. (**a** and **b**) top-view and (**c** and **d**) cross-section images of a ~50 nm thick film and a ~360 nm thick film, respectively. Similar grain sizes (~50 – 200 nm) are observed, revealing the scalability of the fabrication process. Scale bar: 100 nm.

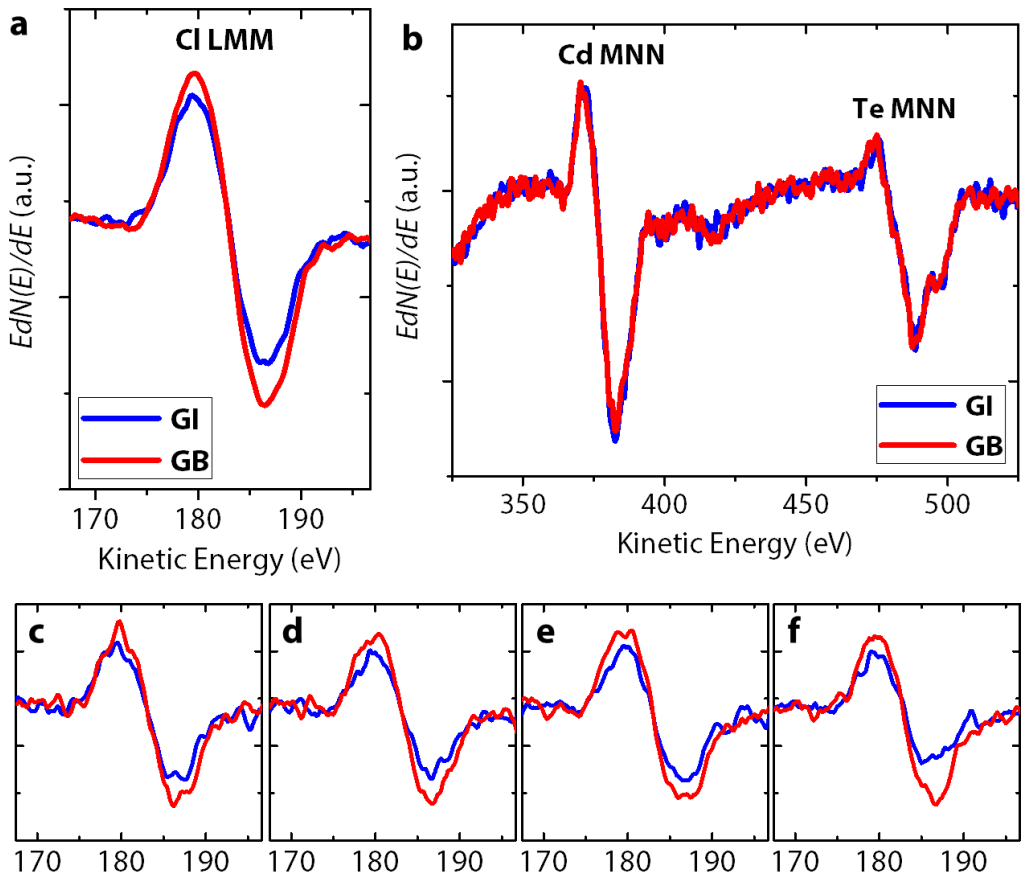

Fig. S2. Nano-Auger electron spectroscopy of the CdTe polycrystalline film. (**a**) Cl Auger peaks of the grain interior (GI) and grain boundary (GB) regions. Each spectrum is an average over 11 spectra from different GI or GB regions. Identical parameters were used to take the spectra at GBs and GIs. The peak-to-peak height in the spectra reveals the relative amount of Cl species. The result shows that the density of Cl species is higher in the GBs than in the GIs. Accurate quantitative values of the concentration are difficult to obtain due to the large size of the incident electron beam spot (~10 nm) compared to the GB size (~1 nm), and the possible e-beam induced evaporation of Cl. Also note that the Auger spectroscopy is sensitive to only the top ~1 nm surface region of the sample, which may not accurately represent the bulk properties. Due to these reasons, the actual ratio of the concentration of Cl in the GBs and GIs can be much larger than the ratio of the peak-to-peak height in the Auger spectra. (**b**) Cd and Te Auger peaks in a GI and a nearby GB, revealing that the concentration of these species is the same, within the noise level, in the GI and the GB (averaged over ~10 nm). (**c** to **f**) Representative Cl Auger peaks at individual GI and nearby GB regions. X and Y axes are the same as those in (**a**).

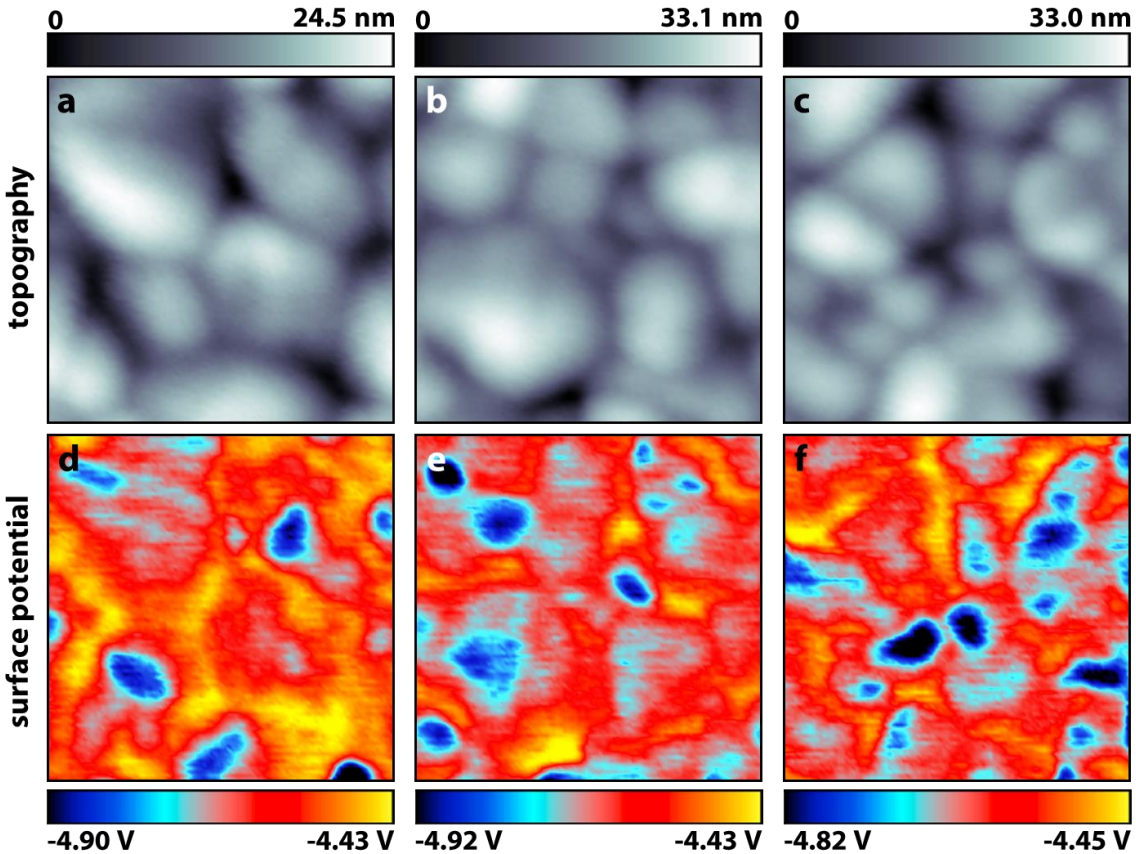

Fig. S3. Kelvin probe force microscopy (KPFM) images of the CdTe films. (**a** to **c**) topography images. (**d** to **f**) Simultaneously obtained surface potential images. Image size: 300 × 300 nm^2. GBs in general have higher surface potential (lower work function) than GIs, although the topography and potential features are not fully correlated (see also Fig. 1c). This is evidence that cross-talk artifacts are absent in our KPFM results.

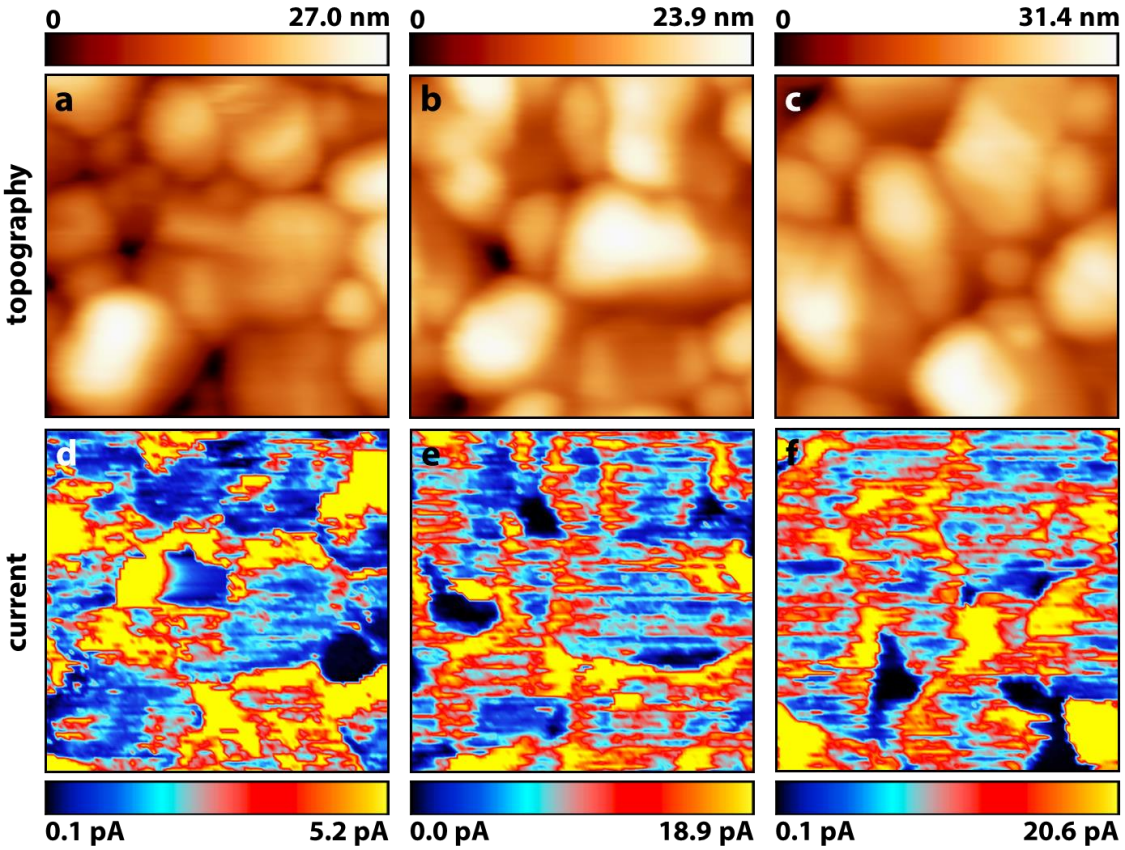

Fig. S4. Conductive atomic force microscopy (CAFM) images. (**a** to **c**) topography and (**d** to **f**) current images on the same areas. Image size: 300 × 300 nm^2. Higher current is consistently observed on the GBs compared to GIs. The absolute magnitude of the current fluctuates in different samples due to variations in tip-sample contact resistance, which is typical for the CAFM technique.

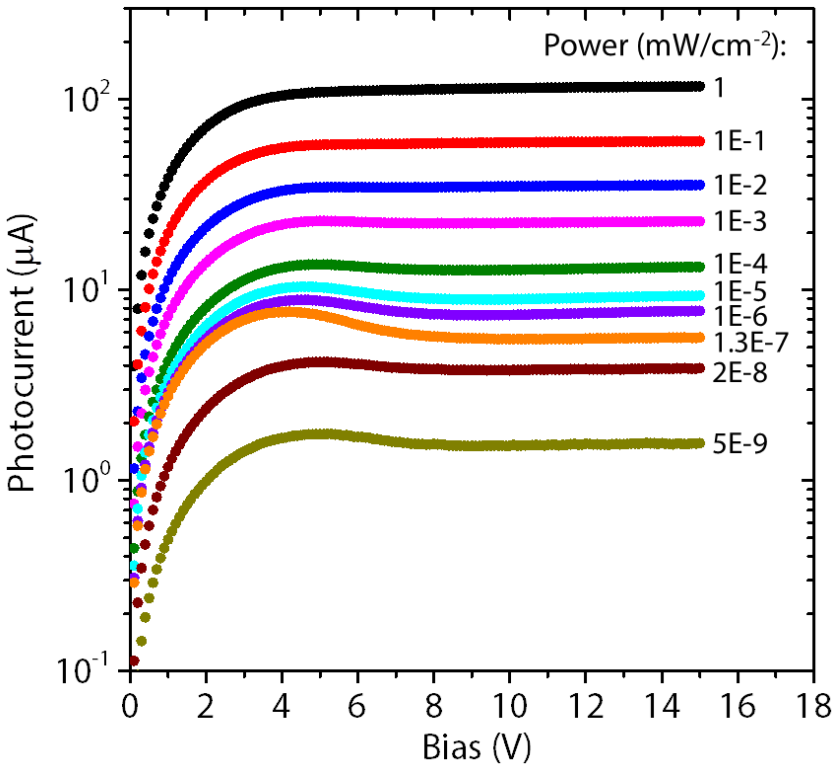

Fig. S5. Photocurrent *vs* bias at different photon power. Channel width: 2 mm; length: 5 μm; thickness: 320 nm. Substrate: quartz. Photon wavelength: 500 nm. Photocurrent saturates at ~4 V, and remains almost constant at higher bias. Photocurrent values at 10 V bias were used to calculate the responsivity and external gain shown as the inverted triangle points in Fig. 3a.

5.7 References

Reference for Supporting Information below main text references

1. Konstantatos, G. & Sargent, E. H. Nanostructured materials for photon detection. *Nature Nanotech.* **5,** 391–400 (2010).

2. Koppens, F. H. L. *et al.* Photodetectors based on graphene, other two-dimensional materials and hybrid systems. *Nature Nanotech.* **9,** 780–793 (2014).

3. Sukhovatkin, V., Hinds, S., Brzozowski, L. & Sargent, E. H. Colloidal quantum-dot photodetectors exploiting multiexciton generation. *Science* **324,** 1542–1544 (2009).

4. Yamazaki, I., Tamai, N., Kume, H., Tsuchiya, H. & Oba, K. Microchannel-plate photomultiplier applicability to the time-correlated photon-counting method. *Rev. Sci. Instrum.* **56,** 1187–1194 (1985).

5. Levine, B. F. & Bethea, C. G. Single photon detection at 1.3 μm using a gated avalanche photodiode. *Appl. Phys. Lett.* **44,** 553–555 (1984).

6. Konstantatos, G. *et al.* Ultrasensitive solution-cast quantum dot photodetectors. *Nature* **442,** 180–183 (2006).

7. Lee, J.-S., Kovalenko, M. V., Huang, J., Chung, D. S. & Talapin, D. V. Band-like transport, high electron mobility and high photoconductivity in all-inorganic nanocrystal arrays. *Nature Nanotech.* **6,** 348–352 (2011).

8. Konstantatos, G. *et al.* Hybrid graphene-quantum dot phototransistors with ultrahigh gain. *Nature Nanotech.* **7,** 363–368 (2012).

9. Lopez-Sanchez, O., Lembke, D., Kayci, M., Radenovic, A. & Kis, A. Ultrasensitive photodetectors based on monolayer MoS_2. *Nature Nanotech.* **8,** 497–501 (2013).

10. Visoly-Fisher, I., Cohen, S. R. & Cahen, D. Direct evidence for grain-boundary depletion in polycrystalline CdTe from nanoscale-resolved measurements. *Appl. Phys. Lett.* **82,** 556–558 (2003).

11. Visoly-Fisher, I., Cohen, S. R., Ruzin, A. & Cahen, D. How polycrystalline devices can outperform single-crystal ones: Thin film CdTe/CdS solar cells. *Adv. Mater.* **16,** 879–883 (2004).

12. Owen, J. S., Park, J., Trudeau, P.-E. & Alivisatos, A. P. Reaction chemistry and ligand exchange at cadmium−selenide nanocrystal surfaces. *J. Am. Chem. Soc.* **130,** 12279–12281 (2008).

13. Anderson, N. C. & Owen, J. S. Soluble, chloride-terminated CdSe nanocrystals: Ligand exchange monitored by ^{1}H and ^{31}P NMR spectroscopy. *Chem. Mater.* **25,** 69–76 (2013).

14. *Norman, Z. M., Anderson, N. C. & Owen, J. S. Electrical transport and grain growth in solution-cast, chloride-terminated cadmium selenide nanocrystal thin films. ACS Nano* **8,** 7513–7521 (2014).

15. Ahrenkiel, R. K. *et al.* Spatial uniformity of minority-carrier lifetime in polycrystalline CdTe solar cells. *Appl. Phys. Lett.* **64,** 2879–2881 (1994).

16. Long, Q., Dinca, S. A., Schiff, E. A., Yu, M. & Theil, J. Electron and hole drift mobility measurements on thin film CdTe solar cells. *Appl. Phys. Lett.* **105,** 042106 (2014).

17. Zhang, Y., Ziegler, D. & Salmeron, M. Charge trapping states at the SiO_2–oligothiophene monolayer interface in field effect transistors studied by Kelvin probe force microscopy. *ACS Nano* **7,** 8258–8265 (2013).

18. Zhang, Y. *et al.* Charge percolation pathways guided by defects in quantum dot solids. *Nano Lett.* **15,** 3249–3253 (2015).

19. Khosroabadi, S. & Keshmiri, S. H. Design of a high efficiency ultrathin CdS/CdTe solar cell using back surface field and backside distributed Bragg reflector. *Opt. Express* **22,** A921–A929 (2014).

20. Single photon counters from Thorlabs with model number: SPCM20A, SPCM50A.

21. Li, C. *et al.* Grain-boundary-enhanced carrier collection in CdTe solar cells. *Phys. Rev. Lett.* **112,** 156103 (2014).

22. Carbone, A. & Mazzetti, P. Grain-boundary effects on photocurrent fluctuations in polycrystalline photoconductors. *Phys. Rev. B* **57,** 2454–2460 (1998).

23. Lai, Y. *et al.* Low-frequency (1/f) noise in nanocrystal field-effect transistors. *ACS Nano* **8,** 9664–9672 (2014).

24. Jeon, S. *et al.* Gated three-terminal device architecture to eliminate persistent photoconductivity in oxide semiconductor photosensor arrays. *Nature Mater.* **11,** 301–305 (2012).

25. Gong, X. *et al.* High-detectivity polymer photodetectors with spectral response from 300 nm to 1450 nm. *Science* **325,** 1665–1667 (2009).

26. Waxman, A. M. *et al.* Progress on color night vision: visible/IR fusion, perception and search, and low-light CCD imaging. *Proc. SPIE* **2736,** 96–107 (1996).

27. Verger, L., Bonnefoy, J. P., Glasser, F. & Ouvrier-Buffet, P. New developments in CdTe and CdZnTe detectors for X and γ-ray applications. *J. Electron. Mater.* **26,** 738–744 (1997).

28. Panthani, M. G. *et al.* High efficiency solution processed sintered CdTe nanocrystal solar cells: The role of interfaces. *Nano Lett.* **14,** 670–675 (2014).

29. Kamal, J. S. *et al.* Size-dependent optical properties of zinc blende cadmium telluride quantum dots. *J. Phys. Chem. C* **116,** 5049–5054 (2012).

References for Supporting Information

30. Sze, S. M. *Physics of Semiconductor Devices* (Wiley, New York, ed. 2, 1981).

31. Strzalkowski, I., Joshi, S. & Crowell, C. R. Dielectric constant and its temperature dependence for GaAs, CdTe, and ZnSe. *Appl. Phys. Lett.* **28,** 350–352 (1976).

32. Rich, C. & Longcore, T. Ed. *Ecological Consequences of Artificial Night Lighting* (Island Press, Washington, DC, 2006).

33. X-Ray & Gamma Ray Detector from Amptek, model number: XR-100T-CdTe.

34. Becker-Szendy, R. *et al.* IMB-3: A Large water Cherenkov detector for nucleon decay and neutrino interactions. *Nucl. Instrum. Meth. A* **324,** 363–382 (1993).

6 Chapter 6: In Situ Transmission Electron Microscopy of Cadmium Selenide Nanorod Sublimation

6.1 Introduction

Despite many advances in the study of nanostructured materials, it remains challenging to develop descriptions of the thermodynamic and kinetic factors that lead a given nanostructure to be stable as these materials are typically in non-equilibrium states. In the case of colloidal nanocrystals, valuable insight into their stability has often come from studies of the transformation of their size, shape, and faceting during growth.[1,2] Such studies have been greatly expanded recently with the advent of high resolution real-time electron microscopy for *in situ* characterization. Nanoparticle growth,[3–5] coalescence,[6,7] and phase changes including melting,[8,9] sublimation,[8,10–13] and crystallographic transformations,[14] have been investigated at the single particle level providing valuable information on the stability and formation of these structures. Collectively these studies begin to describe how these kinetically trapped structures are influenced by the nature of their surface modifications, with ligands playing a key role in manipulating interfacial energies and contributing to stabilization. Here we investigate the sublimation of nanorods. In addition to providing insight into facet stability, observing the sublimation of nanocrystals may serve as a useful complementary approach to directly observing the growth of nanocrystals. While growth and sublimation may occur under different thermodynamic conditions such as pressure, sublimation can shed light on the growth mechanisms if the microscopic steps for the inverse and forward processes are similar. The extension to anisotropic structures offers the opportunity to better understand the relative stability of the diverse crystal facets.

We chose to study Cadmium chalcogenide (CdE, E = S, Se, Te) nanocrystals because their physical and chemical properties have been extensively studied. CdE nanostructures have been applied to a variety of optical and optoelectronic applications such as display phosphors,[15] biological markers,[16] and photovoltaics.[17] Early studies of colloidal II-VI structures focused on dots, or nearly spherical shapes, until approaches to make nanorods were developed. Nanorods form under similar conditions to quantum dots except for the presence of a selectively binding surface ligand, which is believed to retard the growth of one set of facets relative to the others.[2] Anisotropic nanostructures provide a means for building more complex, directional nanostructures sequentially,[18,19] and their broken symmetry leads to optical and electronic properties distinct from their spherical counterparts, including polarized emission[20] and enhanced absorption and charge transport.[21] Exploring sublimation provides insight into facet stability and the influence of surface ligands on these anisotropic nanostructures. Here we study the sublimation of one such model system, CdSe nanorods.

6.2 Experimental Section

6.2.1 Chemicals

Cadmium oxide (CdO) powder (99.99+%), selenium (Se) powder (100 mesh, 99.99%), anhydrous toluene (99.8%), anhydrous ethanol (99.5%), anhydrous methanol (99.8%), anhydrous 2-propanol (99.5%), octylamine (99%, subsequently dried over 4 Å molecular sieves), and nonanoic acid (96%, subsequently dried over 4 Å molecular sieves) were purchased from Sigma Aldrich (St. Louis, MO). N-octadecylphosphonic acid (ODPA, 99%) was purchased from PCI Synthesis (Newburyport, MA), and tri-n-octylphosphine (TOP, 97%), and n-tributylphosphine (TBP, >97%) was purchased from Strem Chemicals (Newburyport, MA).

6.2.2 CdSe nanorod synthesis and purification

CdSe nanorods with the dimensions of approximately 4 x 25 nm were synthesized by hot injection following a previously reported procedure[1] with slight modification. Specifically, 207 mg CdO, 1.09 g ODPA, and 2.77g TOPO were combined in a 25 ml three-neck round bottom flask. This mixture was degassed under vacuum at 150 °C for an hour. After degassing, the flask was backfilled with argon and heated to 320 °C to form the cadmium phosphonate complex. Once the solution became clear, the solution was then cooled and degassed under vacuum at 150 °C for an hour. Meanwhile, 63 mg Se, 1.456 g TOP, 207 mg TBP, and 340 mg toluene was combined in an argon-filled glovebox and stirred until clear. After degassing the cadmium complex, the flask was backfilled with argon and heated. Upon reaching 320 °C, the selenium complex was rapidly injected through a rubber septum into the flask. The temperature was reset to 250 °C. After 60 min., the heating mantle was removed and the flask allowed to cool. Once the temperature was below 100 °C, 10 mL toluene and 2 mL octylamine were injected into the flask to prevent solidification upon cooling to room temperature.

Nanocrystals were isolated and purified in an argon atmosphere. Ethanol was added to the reaction solution to flocculate the nanocrystals which were then centrifuged at 4000 rpm for 10 min. The supernatant was decanted and the precipitate redispersed in toluene. The particles were purified by additional flocculations and centrifugation steps using toluene/ethanol, toluene + nonanoic acid/methanol (4:1 v/v), and toluene/propanol as the solvent and anti-solvent, respectively. Purified nanorods were dispersed in toluene and stored in an argon environment.

6.2.3 Low thermal drift TEM substrates.

We used Aduro Thermal E-chips with a holey carbon support film (part no. E-AHA21) purchased from Protochips, Inc. (Raleigh, NC). These MEMS devices consisted of a proprietary ceramic membrane perforated with 7 µm in diameter holes with 7 µms pitch layered with a ~20 nm amorphous carbon film with 2 µm holes spaced 2 µm apart. Protochips, Inc. calibrated the temperature of each device individually.

6.2.4 TEM sample preparation

TEM samples were prepared in an argon environment by depositing 5 µL of a 10 µM solution of CdSe nanorods at the center of the Aduro E-chip and letting dry. Care must be taken not to break the fragile membrane by contacting it with the pipette tip. Sample temperature was controlled using the Protochips' software and calibration files.

6.2.5 TEM Imaging

CdSe nanocrystal sublimation dynamics were imaged using FEI TitanX microscope at the National Center for Electron Microscopy using a Gatan Orius 830 Camera. Acceleration voltage was set at 80kV to prevent excessive knock-on damage of the nanocrystal. Previous experiments with a similar nanocrystal system (zinc blend CdTe) revealed particle disintegration at 300 kV at room temperature. The average beam current density was 5 nA. Images were recorded with Gatan Microscope V1.8 TEM Imaging and Analysis (TIA). Videos frames were 512x512 pixel arrays with a 12 bit/pixel dynamic range integrated for 0.2 second with a readout time of 0.2s. This yields a 0.4 sec. frame-to-frame interval. Videos were saved in Gatan's *.ser* file type.

6.2.6 Image processing

TEM videos were processed using custom code in *Matlab* utilizing the *Image Processing Toolbox*. Videos were converted to stacks of 512x512 pixels 16 bit grayscale images for easier use with Matlab's Imaging Processing Toolbox functions. Image contrast was adjusted by saturating the intensities of lowest and highest 1% pixels. Nanorod dimensions were measured every five frames using a custom Matlab script.

6.3 Results and Discussion

In this work, we present direct imaging of sublimation in CdSe nanorods under vacuum at a series of temperatures below and above the bulk transition temperature. At the TEM column pressures of 10^{-7} Torr, the sublimation point is predicted to be 389±5 °C;[22] we studied sublimation at 370, 390, 420, and 450°C. Colloidal CdSe nanorods with a Wurtzite crystallographic structure were synthesized following methods established in the literature. The tetradecylphosphonate surfactant retards growth on the non-polar $(10\bar{1}0)$ and $(11\bar{2}0)$ facets, therefore growth occurs along the c-axis which is parallel or antiparallel to the [0001] direction.[23] A dilute solution of nanorods dispersed in toluene was drop casted onto a commercially available, low-thermal drift TEM grid and sublimation of these nanostructures was recorded. The temperature ramp rate for these grid is 10^6 °C/s permitting virtually isothermal heating conditions. Videos of CdSe nanorod sublimation at 370, 390, 420, and 450 °C can be found in Videos S1-4 and selected frames can be found in Figure S1 in the Supporting Information below.

6.3.1 Anisotropic sublimation

Nanorod sublimation proceeded anisotropically from the ends along the c-axis of the Wurtzite crystal structure. We identify the observed phenomena as sublimation since no remnant of a solid, which would manifest as mass-thickness contrast in the TEM image, formed upon the cooling substrate. CdSe nanorod sublimation dynamics at 370 °C is represented in Figure 1, which contains four video frames from Video S1. The bottom row of images of Figure 1 are digitally processed images complementary to the top row to aid in visualizing sublimation progress. The images in Figure 1 show that the nanorods decrease in length due to sublimation, which initiates at the tips and continues along the length of the particle. At this low temperature, mass loss occurred from both ends of the nanorods. At higher temperatures, sublimation occurred exclusively from one end of the nanorod. Figure 2 shows this effect at 450°C.

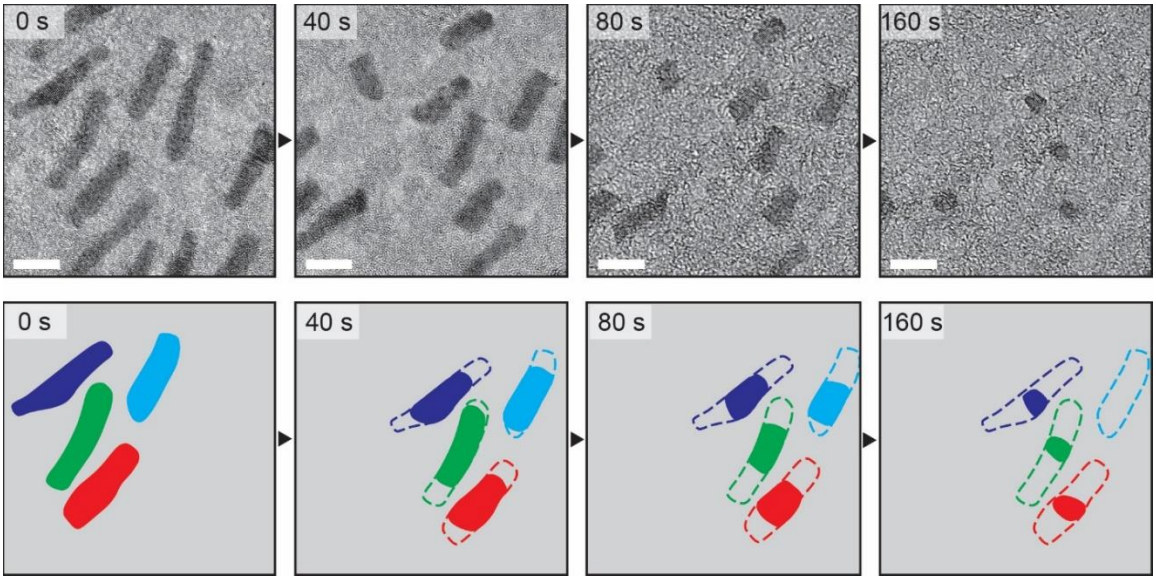

Figure 6.1. (Top) Bright field TEM video frames showing the progression of nanorod sublimation at 370˚C. (Bottom) Qualitative image maps with initial nanorod profiles at t=0 s shown as dotted outlines and profiles at the specified time shown as a solid fill. The scale bar is 10 nm.

6.3.2 Temperature dependence of sublimation

At the lowest temperature, 370°C, nanorod sublimation occurred at a temperature below the predicted bulk sublimation point at the TEM column pressures. Sublimation at this temperature would only initiate after imaging a given field of view. This e-beam phase change induction was not observed at higher temperatures. For example, partially sublimed nanorods are seen at the start of the videos at the higher temperatures, but not at the lowest.

p

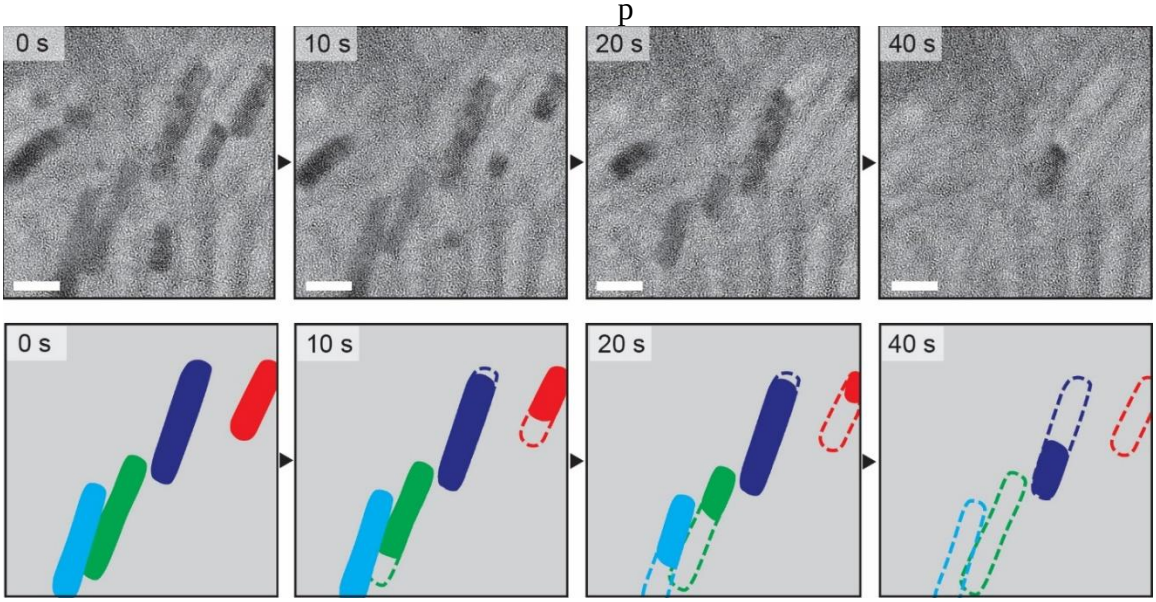

Figure 6.2. (Top) Bright-field TEM video frames at increasing times showing the progression of sublimation from one end of the nanorod at 450˚C. (Bottom) Qualitative image maps with initial nanorod profiles at t=0 s shown as dotted outlines and profiles at the specified time shown as a solid fill. The scale bar is 10 nm.

At all observed temperatures, nanorods generally sublimed anisotropically, losing mass along the c-axis until the particle reached 2-3 nm in length measured along the c-axis. Before reaching this *transition size*, the rod diameter did not change within resolution limits. Upon reaching this transition size, the sublimation direction changed from the c-axis to the ab-axes, and quickly proceeded from one side of the nanorod until no crystal remained. Our analysis will be confined to what happens above this transition size, because below the transition it is difficult to quantify the size of the residual nanocrystals. To quantify the sublimation dynamics above the transition size, we measured the dimensions of four nanorods at each temperature throughout the videos which are identified in Figure S2. Since nanorod widths did not change within resolution limits of the data up until the transition point, we used the rate of linear length decrease along the c-axis of the nanorod to calculate mass loss; see Figure S3 for a schematic of our measurement method.

6.3.3 Sublimation rates

The average sublimation rate increased with temperature as shown in Figure 3. Uncertainty in the rate of sublimation from individual nanorods precludes us from demonstrating if the sublimation follows Arrhenius kinetics and from obtaining an accurate activation energy. Variations in the pattern of sublimation at low and high temperatures could be seen very clearly, however.

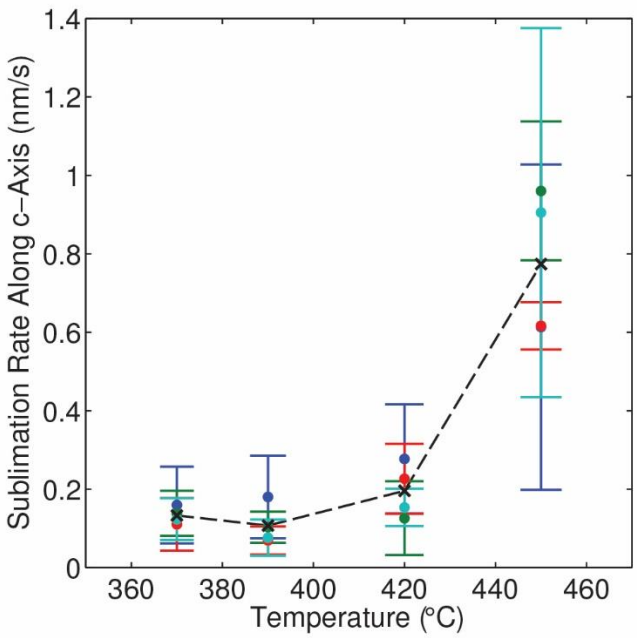

Figure 6.3. Average sublimation rate along c-axis direction for four nanorods at different temperatures. Rates were averaged from both ends during the entire phase change for each nanorod; error bars represent the standard deviation. Black "X" markers and the dashed line indicate average rate for all nanorods at all times for each temperature.

The sublimation rate from the nanorod ends is not always continuous and is strongly dependent on temperature. There are two distinct behaviors: (1) non-continuous, punctuated sublimation from *both* ends at low temperatures, and (2) continuous sublimation from *one* end at high temperatures. The intermediate temperatures exhibited a mixture of these modes. Non-continuous behavior is defined by sporadic pauses occurring locally at a single nanorod end during the course of sublimation. Figure 1 shows all nanorods sublime from both ends at 370 °C. By 450 °C the sublimation only proceeds from one end of the nanorod as seen in Figure 2. This is accompanied by an increased rate of mass loss established in Figure 3. Figure 4 reports the cumulative length sublimed from each end of the four measured nanorods at their respective temperatures using the same methodology established above.

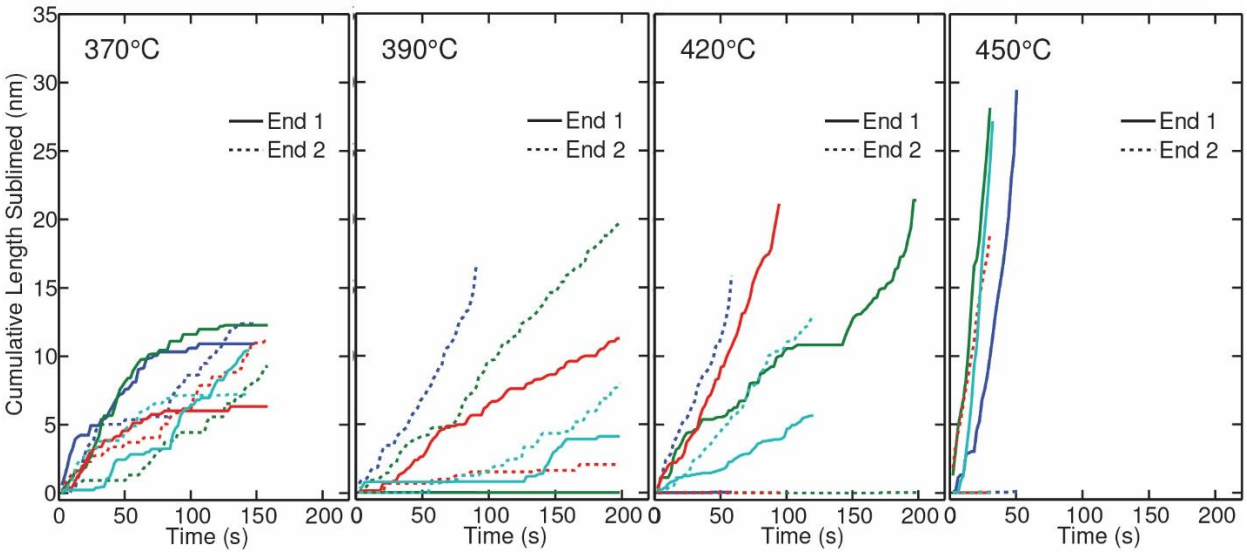

Figure 6.4. Total length sublimed from the ends of each nanorod. Each color represents a different nanorod as indicated in Figure S2, which also correspond to colors in Figure 2. Two ends are differentiated by solid (end closer to top of frame) and dashed line (end closer to bottom of frame) in the orientation in Figure S2.

During sublimation, the solid interface at the nanorod end, or the sublimation front, rocked back and forth as mass vaporized. This interface is defined as a difference in contrast between the nanocrystal and the substrate spanning the width of the nanorod at each tip. As a given sublimation front progressed along the length of the particle, the interface made an angle greater or less than the normal with the c-axis. One side of the front might progress while the opposite remained stationary and appeared "pinned" creating an angle with the c-axis normal. The active front exhibiting this behavior would switch from side to side creating a rocking, or see-saw appearance. This was observed at all temperatures. At the lower temperatures, both sides of the sublimation front would sometimes periodically halt, sometimes ending in what appeared to be a pristine facet from the TEM image.

6.3.4 Mechanism of sublimation in CdSe nanorods

The single particle *in situ* electron microscopy sublimation studies shown here, enable us to see phenomena that would be entirely obscured in ensemble studies. Here there are two rather surprising observations: on the one hand, sublimation is punctuated, but proceeds from both ends of the rods at low temperature; while on the other, sublimation is continuous, but occurs from only one end of a rod at higher temperature. While these observations beg for a clear mechanistic explanation, the fact is that the *in situ* TEM employed here has limitations which allow us for the time being only to provide competing viewpoints that will require further exploration to distinguish between. In what follows, we first present a mechanism relies solely upon what we know about the idealized intrinsic material comprising the nanocrystals as synthesized. This is followed by a more complex explanation that relies upon non-ideal changes in the surface species bound to the nanoparticles induced by the electron beam. Both perspectives focus on elucidating how the kinetic barrier of a desorbing surface species—the rate limiting step—is modified by its coordinating environment. A more complete picture of the sublimation process that distinguishes between these two classes of explanations, ideal and non-ideal, or that even involves a combination of the two must await a new technique that enables simultaneous observation of the surface species on the nanocrystal while it is under observation in the microscope.

To understand the idealized mechanism of CdSe nanorods, we first explore sublimation in an ideal crystal lattice model. Past mechanistic insights on sublimation in bulk II-VI compounds invoke the terrace-ledge-kink model (TLK) of solid surfaces. The sublimation reaction begins when a CdSe unit moves from a terrace to a ledge site, then to a kink site where it dissociates into neutral adsorbates via charge transfer followed by desorption.[24–27] This series of reactions is reversible, and in the opposite direction provide a description of crystal growth. There is disagreement in the literature on whether charge transfer or desorption is the rate limiting step for cadmium chalcogenides.[24–30] In the context of CdSe nanorod sublimation, we consider a simplified reaction mechanism in which understanding what influences the activation barrier of the rate limiting step—either charge transfer or desorption—is key to understanding the observed sublimation behavior. Below we will discuss how the coordination environment of the surface CdSe unit may affect this activation barrier.

In a pure CdSe crystal, the rate limiting step is slow when the surface unit has a high coordination number such as a site on a pristine facet, or a terrace in the TLK model, compared to a low coordination site, such as a kink. Past investigations in bulk crystals found the limiting step occurred fastest at a kink site.[24–30] Mass loss is expected to be faster from a surface with a large population of kink sites and slower from a surface populated with ledges and terraces. When the crystal is less than ideal, defects may also play an important role in sublimation by reducing the activation energy of sublimation. For example, higher concentration of vacancies increase the probability of lower coordinated CdSe units, while twinning and stacking faults produce strain in a lattice reducing the bonding energy with adjacent atoms.

We add a level of complexity to this model crystal by considering an ideal ligand shell. Nanorods are distinct from bulk crystals by possessing a high ratio of surface to interior atoms which are subject to coordination to other molecules such as ligands. Since it has been established

that the coordination environment of surface species determines the sublimation rate, we must explore how binding to these other species influences the kinetic barrier. First-principles calculations of the relative surface energies of ligand-passivated facets show that the polar {0001} facets of a bare CdSe nanorod with a relaxed and reconstructed surface have a higher surface energy compared to the non-polar sides.[31–33] Coordinating the wurtzite CdSe surfaces with methyl phosphonic acid—a ligand similar to the species in our system—further increased the stability of the non-polar sides relative to the tips; the former were shown to be most stable upon ligand passivation.[32–36]

In view of the factors above that can influence the kinetic barrier to sublimation, we first propose an idealized mechanism for the observed phase transition behavior. Sublimation initiates when a CdSe unit positioned at a high energy surface site on the nanorod end undergoes charge transfer and desorbs. We suspect this occurs at a site that is not coordinated by a surface ligand as calculations show methylphosphonic acid does not completely passivate the polar end facets.[32] The departure of this initial unit produces lower coordinated sites such as kinks which will sublime yielding additional kinks, and ultimately leading to a surface rich in kinks; this is a *nucleation event* in the phase transition.

At 370°C, sublimation was observed at a temperature below the predicted bulk transition point. The electron beam played a role in initiating sublimation, since the phase transformation initiated only after illumination. Incident electrons can transfer kinetic energy resulting in sample heating, or simply increase charge concentration in CdSe therefore promoting charge transfer between the heteroatoms[11,14,26,37] Depending on the nature of the rate limiting step, both effects assist in overcoming a potential barrier for the phase change and lead to sublimation below the predicted bulk transition point. We cannot rule out phase transition size effects, such as the melting point suppression in spherical CdS nanocrystals.[38] However, the depression of the melting temperature is less pronounced in asymmetrical structures such as nanowires.[39,40]

Once sublimation is induced at the nanorod tip, the mass loss continues along the c-axis of the nanorods at an interface rich in kink sites. This behavior is consistent with the calculations discussed above: the non-polar facets that comprised the nanorod sides are greatly stabilized by coordination with the ligands compared to the ends, favoring mass loss along the c-axis. This anisotropic behavior corroborates past experimental observations of sublimation from single crystals. In CdSe/CdS octapods, the CdS arms sublimed along the c-axis.[41] In bulk wurtzite CdS, sublimation from the bulk (0001) face was found to be faster than the non-polar $(10\bar{1}0)$ face, but only by a factor of less than two.[42] In rocksalt PbS nanocrystals, sublimation occurred faster from the polar {111} facets than the non-polar {001} surfaces and ligand passivation was suggested to play a role.[8] The strong ligand stabilization of the side atoms is also likely responsible for the "pinning" of the side atoms that result in the rocking behavior of the sublimation fronts as well as post *transition size* sublimation behavior. In both cases, cadmium phosphonate strongly bonds to the CdSe units on the non-polar facets increasing the barrier to sublimation. A similar behavior was observed directly in the TEM in silver cubes (sides ~100 nm): surface interaction by the polymer ligand shell influence the facet order of sublimation.[10]

A mechanism based upon an idealized nanorod-ligand model can be invoked to describe the two sublimation behaviors. Whether a phase change occurs from both or one end is dependent on temperature, but other factors such as ligand surface pinning at the nanorod tips and the asymmetry of the crystal may also play a role. At the higher temperature, the sublimation still initiates from the nanorod end. If the potential barrier imposed by the ligand is not as strongly influenced by temperature as sublimation, then it is possible that at the highest temperatures, once the phase change is initiated at one end, the sublimation rate is so rapid that the rod vaporizes before the opposite rod end can nucleate. The asymmetry in the nanorod may exacerbate this effect. For instance, the calculations mentioned above revealed that the $(000\bar{1})$ face prefers no ligand passivation and is less stable than the opposite (0001) which maintains partial passivation. [32,33] Furthermore, the wurtzite CdSe crystal lacks an inversion center along the c-axis creating two different bonding environments for atoms at the (0001) and $(000\bar{1})$: on an unreconstructed surface cadmiums bond to three selenium atoms on the (0001) surface but have only one bond on the $(000\bar{1})$ face. In fact, past investigations suggest that the $[000\bar{1}]$ is the direction of growth.[28–30,43] If this applies to sublimation, than we expect mass loss to occur faster in this direction. However, we cannot distinguish between the two facets within the resolution of our images.

The punctuated versus continuous sublimation behavior observed can be explained by the perturbation of the kinetic barrier of the surface CdSe units. Similar non-uniform sublimation behavior was observed in silver and PbS nanocrystals.[8,11] Van Huis et. al. attributed pauses in PbS to the stochastic nature of microscopic processes and ligand passivation of particular facets.[8] Asoro et. al. suggested a mechanism whereby the nanocrystal fractures along a low energy facet creating a small fragment which then rapidly vaporizes due to its large surface area. [8,11] Because of the limits of our frame rate and image resolution, we cannot assess if the latter process applies. One might suspect that the pauses observed at the lower temperatures may be induced by local cooling below the transition point due to the latent heat of sublimation and thus temporarily decrease the sublimation rate. However, the speed of sound in CdSe is 1.5-3.8 x 10^7 m/s, which prevents thermal gradients at these length scales.[44]

Invoking our idealized nanocrystal model, we propose a mechanism whereby the punctuated and uniform sublimation rates observed at lower and higher temperature are controlled by the coordination of the surface CdSe units. In an ideal CdSe nanorod end free of surface ligand, the sublimation rate is fast from a surface populated with low coordination sites such as kinks, and slow from one dominated by low coordination sites such as ledges or terraces. A clean {0001} facet will cause the rate to "freeze" momentarily until a kink site is nucleated. Sublimation appears punctuated at low temperatures as the nanorod ends fluctuate between large populations of low coordination sites and high coordination sites, and can even pause at kink free facet. Temporary basal plane facets can been seen at the nanorod ends at 370 °C in Video S1; rod A exhibits a sustained {0001} plane at t = 8s (video time, ~105s real time). In the high temperature regime only kink sites exist, or are easily generated by surface diffusion, and mass loss is continuous. This is consistent with the images which show rounded nanorod tips and the lack of any basal planes at high temperatures. Defects may contribute to the punctuated behavior of the low temperature regime. As an advancing front encounters defects, sublimation proceeds quickly as these sites have

a reduced kinetic barrier. However, we are unable to confirm the presence of defects in our samples due to resolution limits.

An equally plausible mechanism based upon non-ideal changes in the surface species offers an alternative description of the two sublimation behaviors. When running an in-situ experiment inside the TEM, we must be cognizant of the e-beam effects. High energy dosages lead to decomposition of the ligand shell and the presence of other unknown contaminants in the column that can modify the nanorod surface and influence the kinetic barrier to sublimation. The presence of a lighter contrast footprint of the nanorod remained after sublimation which is indicative of organic deposition. A similar shell was observed in the sublimation of CdS/CdSe octopods and silver cubes.[10,41] Besides ligands, other species can adsorb to the nanocrystal surface and inhibit the sublimation rate. These species are most likely carbon, but unknown TEM column contaminants from previous experiments cannot be definitively ruled out. The ligand alkyl chains or carbon support can decompose, vaporize, and redeposit as amorphous carbon on the nanorods. Furthermore, alkyl chains have been reported to crosslink under electron beam radiation which would convert the ligands into stronger binding, multidentate species.[45–47] We suspect a carbon shell exists around nanorods in our experiments, and further this shell need not arise from crosslinking of ligands. Past investigations report that the deposition of polymerized pump oils used in diffusion pumps lead to sublimation retardation in bulk CdS crystals.[42]

A sublimation mechanism based upon non-ideal conditions within the TEM can offer a competing viewpoint to the ideal model. Contaminants deposited on the nanorod surface would increase the kinetic barrier of the rate limiting step, which could potentially reduce the rate of mass loss from the tips. At lower temperatures, it is possible that the sublimation rate may be similar to the contaminant deposition rate. If this is correct, then the sublimation front would pause when contaminants deposit, then continue after the surface "unpins" from the contaminant via nucleation or desorption of the foreign species. At higher temperatures, sublimation might occur much faster than deposition resulting in continuous mass loss. Clearly, further experiments are needed to test this hypothesis.

6.4 Conclusion

We observed CdSe nanorods sublime anisotropically along the direction of the least stable facet. The sublimation rate, measured along the c-axis, increased with temperature. Two distinct behaviors of sublimation were discovered: non-continuous from both ends at lower temperatures and continuous from one end at higher temperatures. A mechanism which considers the coordination environment of the surface species is explained using two nanocrystals models, ideal and non-deal, that can potentially account for these results, and further experiments are needed to explain these surprising sublimation observations.

6.5 Supporting Information

Videos S1-4 are available free of charge via the internet at http://pubs.acs.org.

6.5.1 Calculation of sublimation temperature

The sublimation temperature of CdSe was calculated with the Antoine equation using literature values that were dervided from empirical fits. We used the values for the dissociation pressure of wurtzite CdSe from various sources aggregated by Sharma and Chang[2] except one set which was assesed as an outlier by Sigai and Wiedemeier[3] (see table below). The total pressure, $Ptot = P_{Cd} + P_{Se_2}$, was taken to be the at the column pressure 10^{-7} Torr.

$$Log_{10}\left(P_{tot}(bar)\right) = -\frac{A}{T(K)} + B$$

Source #	A	B	T_{vap}(K)
1	11480	7.309	668.1
2	10976	6.766	659.6
3	11306	7.102	666.0
4	10848	6.586	659.0
5	11088	7.009	656.7
Average			661.9±4.9

6.5.2 Other comments on data

The data contains a few noticeable imperfections. Aduro E-chips minimize, but do not eliminate, thermal drift. To counteract thermal drift during video acquisition, the electron beam was tilted to maintain the same field of view. This moved the focal point off the image plane compromising focus and beam alignment. Imperfect focus is manifested as white halos at the rod ends and poor resolution in certain frames. During the experiment, heat was transferred from the membrane edge (i.e. heat source) to the nanoparticles through an amorphous carbon support film. This distance was not measured but had a range of 0.1-3.5 μm. Averaging rates throughout the entire phase transformation, small sample size (four rods per temperature) of inherently stochastic processes, and image resolution limitations contributed to large error bars seen in Figure 2.

6.5.3 S Figures

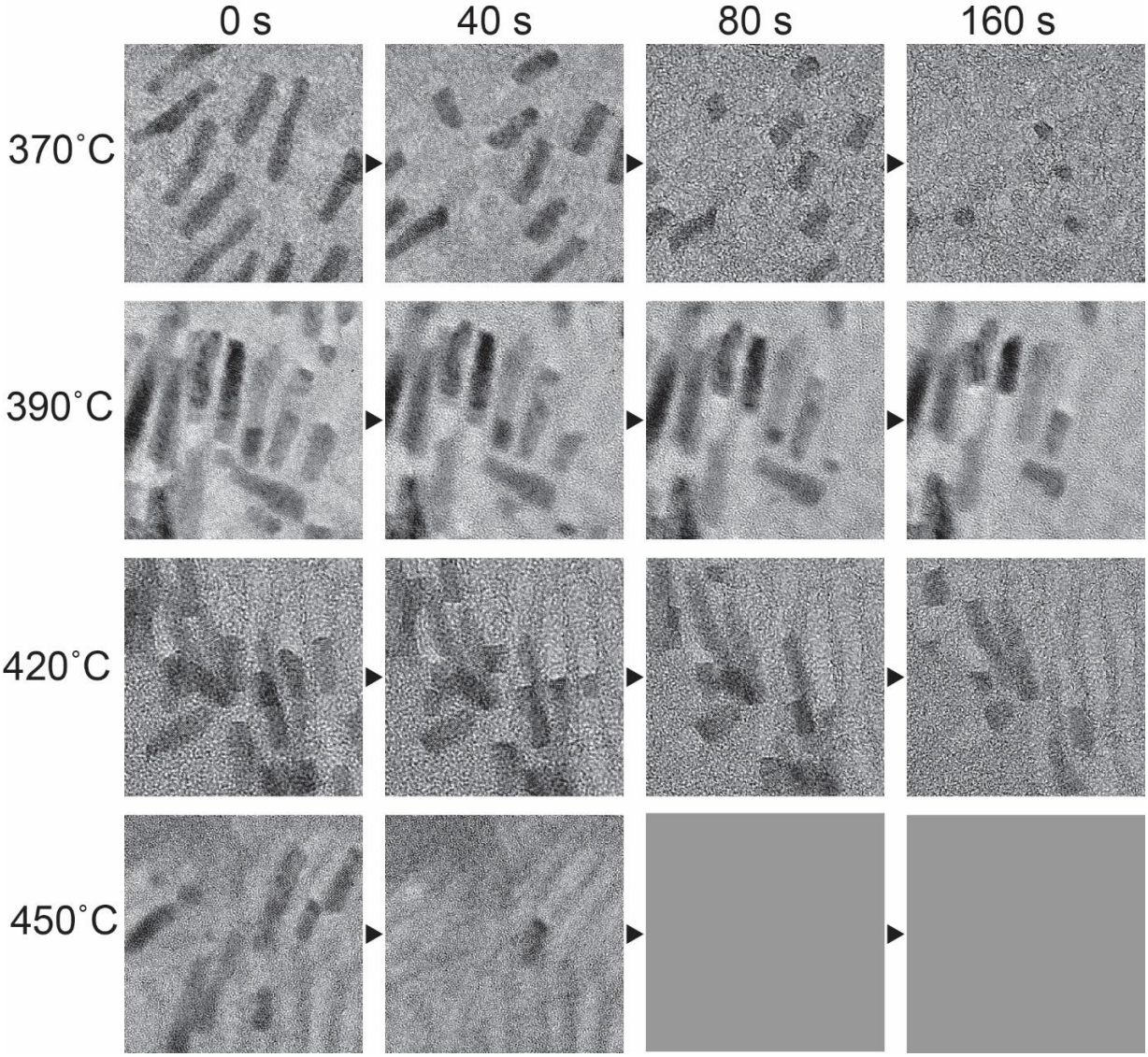

Figure S1. Video frames of CdSe nanorod sublimation at 370, 390, 420, and 450˚C.

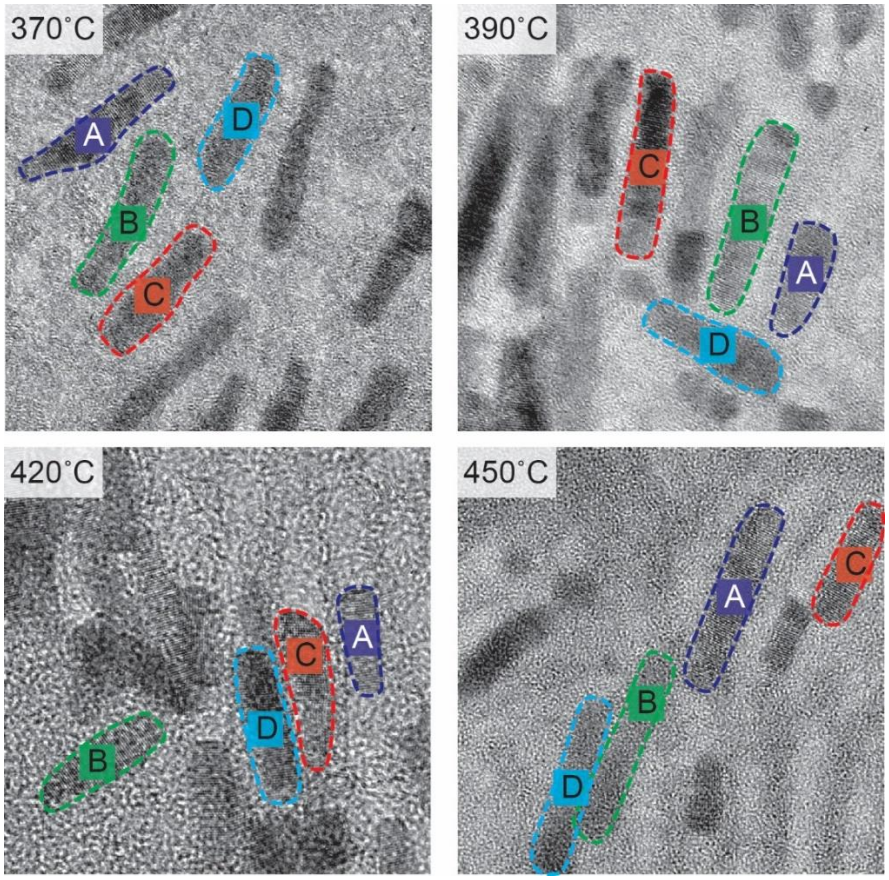

Figure S2. Map of measured nanorods at each temperature on the first video frame.

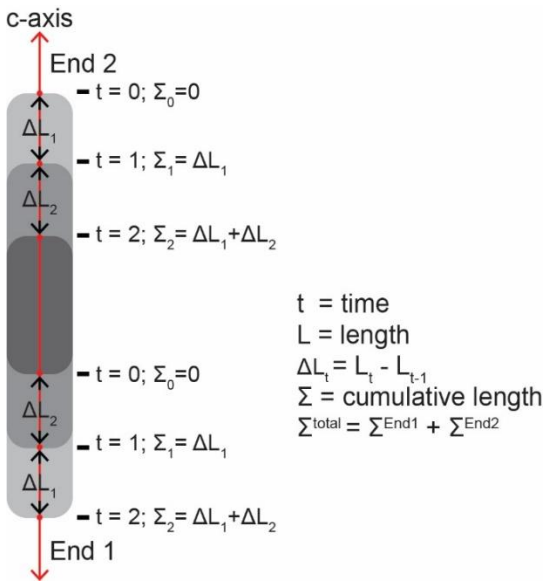

Figure S3. Illustration of measurement method showing how cumulative length (Σ) for each end is the sum of the length difference (ΔL) between two times. We used linear length as a proxy for mass loss since nanorod width did not change, within resolution limits, up until the *transistion size*.

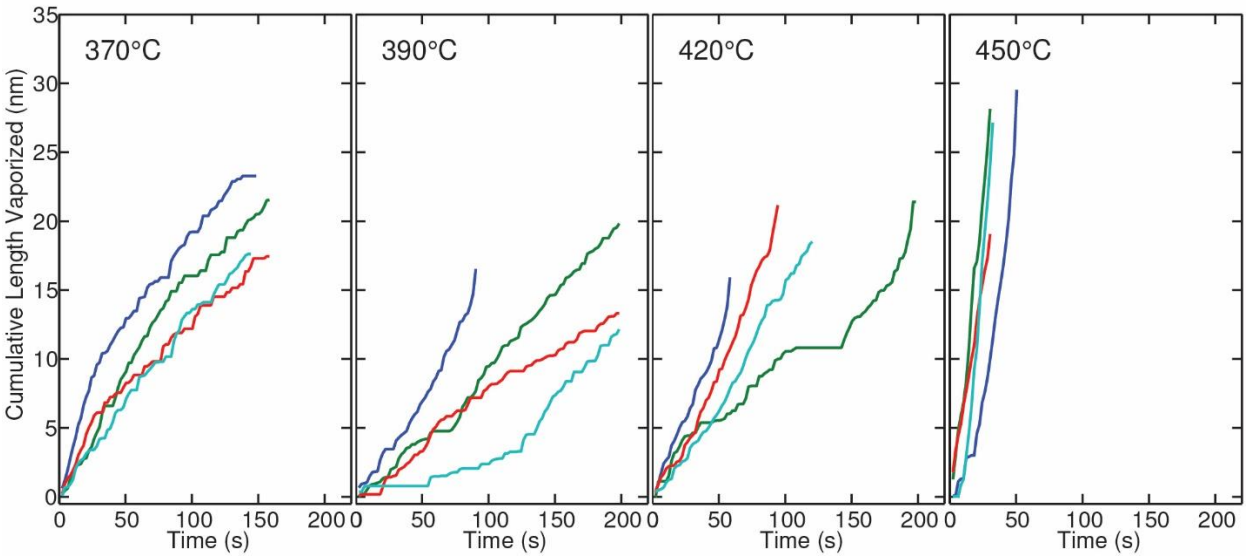

Figure S4. Total cumulative length (End 1 + End 2) sublimed over time. Colors correspond to different nanorods measured defined in Fig. S1.

6.6 Acknowledgements

The authors would like to thanks J. Ciston and K. Bustillo for their assistance with the NCEM facility, P. Ercius for sharing his knowledge of image processing, and C. Bear for help with the TOC figure. This work was performed at NCEM, which is supported by the Office of Science, Office of Basic Energy Sciences of the U.S. Department of Energy under Contract No. DE-AC02-05CH11231. D.H. was supported in part from the US National Science Foundation Graduate Research Fellowship. Work on image analysis was supported by the Physical Chemistry of Inorganic Nanostructures program, KC3103, Director, Office of Science, Office of Basic Energy Sciences, of the United States Department of Energy under contract DE-AC02-05CH112321.

6.7 References

For experimental section reference, see below.

(1) Glotzer, S. C.; Solomon, M. J. Anisotropy of Building Blocks and Their Assembly into Complex Structures. *Nat. Mater.* **2007**, *6*, 557–562.

(2) Yin, Y.; Alivisatos, A. P. Colloidal Nanocrystal Synthesis and the Organic-Inorganic Interface. *Nature* **2005**, *437*, 664–670.

(3) Zheng, H.; Smith, R. K.; Jun, Y.-W.; Kisielowski, C.; Dahmen, U.; Alivisatos, A. P. Observation of Single Colloidal Platinum Nanocrystal Growth Trajectories. *Science* **2009**, *324*, 1309–1312.

(4) Yuk, J. M.; Park, J.; Ercius, P.; Kim, K.; Hellebusch, D. J.; Crommie, M. F.; Lee, J. Y.; Zettl, A.; Alivisatos, A. P. High-Resolution EM of Colloidal Nanocrystal Growth Using Graphene Liquid Cells. *Science* **2012**, *336*, 61–64.

(5) Liao, H.-G.; Zherebetskyy, D.; Xin, H.; Czarnik, C.; Ercius, P.; Elmlund, H.; Pan, M.; Wang, L.-W.; Zheng, H. Facet Development During Platinum Nanocube Growth. *Science* **2014**, *345*, 916–919.

(6) Lim, T. H.; Mccarthy, D.; Hendy, S. C.; Stevens, K. J.; Brown, S. A.; Tilley, R. D. Real-Time TEM and Kinetic Monte Carlo Studies of the Coalescence of Decahedral Gold Nanoparticles. *ACS Nano* **2009**, *3*, 3809–3813.

(7) Asoro, M. A.; Kovar, D.; Shao-Horn, Y.; Allard, L. F.; Ferreira, P. J. Coalescence and Sintering of Pt Nanoparticles: In Situ Observation by Aberration-Corrected HAADF STEM. *Nanotechnology* **2010**, *21*, 025701.

(8) Van Huis, M. A.; Young, N. P.; Pandraud, G.; Creemer, J. F.; Vanmaekelbergh, D.; Kirkland, A. I.; Zandbergen, H. W. Atomic Imaging of Phase Transitions and Morphology Transformations in Nanocrystals. *Adv. Mater.* **2009**, *21*, 4992–4995.

(9) Link, S.; Wang, Z. L.; El-Sayed, M. A. How Does a Gold Nanorod Melt? *J. Phys. Chem. B* **2000**, *104*, 7867–7870.

(10) Ding, Y.; Fan, F.; Tian, Z.; Wang, Z. L. Sublimation-Induced Shape Evolution of Silver Cubes. *Small* **2009**, *5*, 2812–2815.

(11) Asoro, M. A.; Kovar, D.; Ferreira, P. J. In-Situ Transmission Electron Microscopy Observations of Sublimation in Silver Nanoparticles. *ACS Nano* **2013**, *7*, 7844–7852.

(12) Lee, J.-G.; Lee, J.; Tanaka, T.; Mori, H. In Situ HREM Observation of Crystalline-to-Gas Transition in Nanometer-Sized Ag Particles. *Phys. Rev. Lett.* **2006**, *96*, 075504.

(13) Yim, J. W. L.; Xiang, B.; Wu, J. Sublimation of GeTe Nanowires and Evidence of Its Size Effect Studied by in-Situ TEM. *J. Am. Chem. Soc.* **2009**, *131*, 14526–14530.

(14) Zheng, H.; Rivest, J. B.; Miller, T. A.; Sadtler, B.; Lindenberg, A.; Toney, M. F.; Wang, L.-W.; Kisielowski, C.; Alivisatos, A. P. Observation of Transient Structural-Transformation Dynamics in a Cu2S Nanorod. *Science* **2011**, *333*, 206–209.

(15) Lee, J.; Sundar, V. C.; Heine, J. R.; Bawendi, M. G.; Jensen, K. F. Full Color Emission Form II-VI Semiconductor Quantum Dot-Polymer Composits. *Adv. Mater.* **2000**, *12*, 1102–1105.

(16) Bruchez Jr., M.; Morone, M.; Gin, P.; Weiss, S.; Alivisatos, A. P. Semiconductor Nanocrystals as Fluorescent Biological Labels. *Science* **1998**, *281*, 2013–2016.

(17) Kamat, P. V. Quantum Dot Solar Cells. Semiconductor Nanocrystals as Light Harvesters. *J. Phys. Chem. C* **2008**, *112*, 18737–18753.

(18) Mokari, T.; Rothenberg, E.; Popov, I.; Costi, R.; Banin, U. Selective Growth of Metal Tips onto Semiconductor Quantum Rods and Tetrapods. *Science* **2004**, *304*, 1787–1790.

(19) Talapin, D. V; Nelson, J. H.; Shevchenko, E. V; Aloni, S.; Sadtler, B.; Alivisatos, A. P. Seeded Growth of Highly Luminescent CdSe/CdS Nanoheterostructures with Rod and Tetrapod Morphologies. *Nano Lett.* **2007**, *7*, 2951–2959.

(20) Hu, J.; Li, L.-S.; Yang, W.; Manna, L.; Wang L-W; Alivisatos, A. P. Linearly Polarized Emission from Colloidal Semiconductor Quantum Rods. *Science* **2001**, *292*, 2060–2063.

(21) Huynh, W. U.; Dittmer, J. J.; Alivisatos, A. P. Hybrid Nanorod-Polymer Solar Cells. *Science* **2002**, *295*, 2425–2427.

(22) Sharma, R. C.; Chang, Y. A. The Cd-Se (Cadmium-Selenium) System. *J. Phase Equilibira* **1996**, *17*, 140–145.

(23) Peng, Z. A.; Peng, X. Nearly Monodisperse and Shape-Controlled CdSe Nanocrystals via Alternative Routes: Nucleation and Growth. *J. Am. Chem. Soc.* **2002**, *124*, 3343–3353.

(24) Meschi, D. J.; Searcy, A. W. The Kinetics of Dissociative Vaporization Reactions. *High Temp. Sci.* **1974**, *6*, 221–236.

(25) Short, D. W.; Rapp, R. A.; Hirth, J. P. Influence of Surface Charge and Surface Structure on the Sublimation of Ionic Crystals. *J. Chem. Phys.* **1972**, *57*, 1381.

(26) Somorjai, G. A. Mechanism of Sublimation. *Science* **1968**, *162*, 755–760.

(27) Munir, Z. A.; Hirth, J. P. Transient Phenomena in the Sublimation of Cadmium Sulfide. *J. Electron. Mater.* **1977**, *6*, 409–424.

(28) Munir, Z. A.; Seacrist, L. S.; Hirth, J. P. Morphology of Thermally Etched Basal Surfaces of Cadmium Selenide. *Surf. Sci.* **1971**, *28*, 357–372.

(29) Seacrist, L. S.; Munir, Z. A. Studies on the Sublimation of IIB-VIA Compounds IV. The Anisotropic Behavior of the Sublimation of Basal-Plane Oriented Crystals of Cadmium Selenide. *High Temp. Sci.* **1971**, *3*, 340–348.

(30) Leonard, R. B.; Searcy, A. W. The Variation of Vaporization Rates with Orientation for Basal Planes of Zinc Oxide and Cadmium Sulfide. *J. Appl. Phys.* **1971**, *42*, 4047.

(31) Puzder, A.; Williamson, A. J.; Zaitseva, N.; Galli, G.; Manna, L.; Alivisatos, A. P. The Effect of Organic Ligand Binding on the Growth of CdSe Nanoparticles Probed by Ab Initio Calculations. *Nano Lett.* **2004**, *4*, 2361–2365.

(32) Manna, L.; Wang, L. W.; Cingolani, R.; Alivisatos, A. P. First-Principles Modeling of Unpassivated and Surfactant-Passivated Bulk Facets of Wurtzite CdSe: A Model System

for Studying the Anisotropic Growth of CdSe Nanocrystals. *J. Phys. Chem. B* **2005**, *109*, 6183–6192.

(33) Rempel, J. Y.; Trout, B. L.; Bawendi, M. G.; Jensen, K. F. Properties of the CdSe(0001), (0001), and (1120) Single Crystal Surfaces: Relaxation, Reconstruction, and Adatom and Admolecule Adsorption. *J. Phys. Chem. B* **2005**, *109*, 19320–19328.

(34) Hughes, S. M.; Alivisatos, A. P. Anisotropic Formation and Distribution of Stacking Faults in II-VI Semiconductor Nanorods. *Nano Lett.* **2013**, *13*, 106–110.

(35) Talapin, D. V; Shevchenko, E. V; Murray, C. B.; Kornowski, A.; Förster, S.; Weller, H. CdSe and CdSe/CdS Nanorod Solids. *J. Am. Chem. Soc.* **2004**, *126*, 12984–12988.

(36) Manna, L.; Scher, E. C.; Li, L.-S.; Alivisatos, A. P. Epitaxial Growth and Photochemical Annealing of Graded CdS/ZnS Shells on Colloidal CdSe Nanorods. *J. Am. Chem. Soc.* **2002**, *124*, 7136–7145.

(37) Hobbs, L. W. Radiation Effects with Inorganic Specimens. In *Introduction to Analytical Electron Microscopy*; Hren, J. J.; Goldstein, J. I.; Joy, D. C., Eds.; Plemnum Press: New York, 1979; pp. 437–480.

(38) Goldstein, A. N.; Echer, C. M.; Alivisatos, A. P. Melting in Semiconductor Nanocrystals. *Science* **1992**, *256*, 1425–1427.

(39) Goswami, G. K.; Nanda, K. K. Comment on "Size-Dependent Melting Behavior of Zn Nanowire Arrays" [Appl. Phys. Lett. 88, 173114 (2006)]. *Appl. Phys. Lett.* **2007**, *91*, 196101.

(40) Gulseren, O, Ercolessi, F, Tosatti, E. Premelting of Thin Wires. *Phys. Rev. B* **1995**, *51*, 7377–7380.

(41) Goris, B.; Huis, M. a Van; Bals, S.; Zandbergen, H. W.; Manna, L.; Tendeloo, G. Van. Thermally Induced Structural and Morphological Changes of CdSe/CdS Octapods. *Small* **2012**, *8*, 937–942.

(42) Somorjai, G. A.; Stemple, N. R. Orientation Dependence of the Evaporation Rate of CdS Single Crystals. *J. Appl. Phys.* **1964**, *35*, 3398.

(43) Lam, S.-T. A Unified Approach to the Vaporization Process of II-VI Compounds, University of California, Davis, 1979.

(44) Cline, C. F. Elastic Constants of Hexagonal BeO, ZnS, and CdSe. *J. Appl. Phys.* **1967**, *38*, 1944.

(45) Zharnikov, M.; Frey, S.; Heister, K.; Grunze, M. Modification of Alkanethiolate Monolayers by Low Energy Electron Irradiation: Dependence on the Substrate Material and

on the Length and Isotopic Composition of the Alkyl Chains. *Langmuir* **2000**, *16*, 2697–2705.

(46) Nandwana, V.; Subramani, C.; Yeh, Y.-C.; Yang, B.; Dickert, S.; Barnes, M. D.; Tuominen, M. T.; Rotello, V. M. Direct Patterning of Quantum Dot Nanostructures via Electron Beam Lithography. *J. Mater. Chem.* **2011**, *21*, 16859.

(47) Miszta, K.; Greullet, F.; Marras, S.; Prato, M.; Toma, A.; Arciniegas, M.; Manna, L.; Krahne, R. Nanocrystal Film Patterning by Inhibiting Cation Exchange via Electron-Beam or X-Ray Lithography. *Nano Lett.* **2014**, *14*, 2116–2122.

References for experimental section

(1) Peng, Z. A.; Peng, X. Nearly Monodisperse and Shape-Controlled CdSe Nanocrystals via Alternative Routes: Nucleation and Growth. *J. Am. Chem. Soc.* **2002**, *124*, 3343–3353.

(2) Sharma, R. C.; Chang, Y. A. The Cd-Se (Cadmium-Selenium) System. *J. Phase Equilibira* **1996**, *17*, 140–145.

(3) Sigai, A. G.; Wiedemeier, H. Solid-Gas Phase Equilibria and Thermodynamic Properties of Cadmium Selenide. *J. Electrochem. Soc.* **1972**, *119*, 910–914.